System characterisation of a full body slit scanning radiography machine: Theory and experiment.

Martin Scheelke

Supervisor: Tania Douglas

Submitted to the Faculty of Health Sciences at the University of Cape Town in partial fulfillment of the requirements for the degree of Master of Science in Biomedical Engineering.
Cape Town

June, 2005

Declaration

I, MARTIN SCHEELKE, hereby declare that the work that this thesis is based is my original work (except where acknowledgements indicate otherwise) and that neither the whole nor any part of it has been, is being or is to be submitted for any other degree in this or any other University.

Signature removed

Signature

28/03/2006

Date

Abstract

This thesis describes a system model of the imaging chain of the Statscan slit scanning full body radiography machine. A Cascaded Linear-Systems model of the detector was developed and the theoretical DQE, MTF and NPS were compared to measured values for the RQA7 beam quality described in IEC 62220-1. The effect on Detector DQE of various system parameters such as coupling efficiency, CCD noise and pixel binning was quantified. Also, detector performance for various thicknesses of Gd_2O_2S:Tb screens was analysed. The notion of "System DQE" has been suggested by several authors to facilitate the comparison of overall systems rather than only the detector efficiency. An expression for the overall "System DQE" of the Statscan system was developed by including system level effects such as scattered radiation, grid attenuation and geometric blur in the Cascaded Linear-Systems Model. Scattered radiation was quantified as a function of system geometry parameters and was treated as an "Additive Noise Stage". A realistic model of the focal spot was used to calculate the MTF due to beam divergence in the scan direction and focal spot unsharpness in the slit direction. The effect of geometric blur was included as a "Quantum Scatter Stage" in the Cascaded Linear-Systems Model. Grid attenuation was treated as a "Binary Selection Stage". It was found that the "System DQE" is a valuable parameter for the purpose of comparing gridless slit scanning system performance to conventional geometry system performance. Also the "System DQE" parameter could be useful for the optimisation of the imaging performance of entire radiography systems.

Acknowledgments

Greg Flash of Lodox Systems for his assistance with practical aspects of the Statscan machine and general support.

Mattieu de Villiers of Lodox Systems for his assistance and guidance with the DQE measurements.

Herman Potgieter of Lodox Systems for general guidance, ideas and support.

Carlos Sousa, Dries Vermeulen and Ben Wright of Lodox Systems for assistance with practical hardware and software issues.

Dr. Tania Douglas and Prof. Kit Vaughan of the Biomedical Engineering Department of the University of Cape Town for their guidance and assistance.

Dr. Jeffrey H. Siewerdsen of the Ontario Cancer Institute, Princess Margaret Hospital, Toronto for his advice on Cascaded Linear-Systems models.

Dr. Ulrich Neitzel of Philips Medical Systems for his advice on DQE measurement techniques.

Bruce Becker and Mark Horner of the University of Cape Town, Physics Department, CERN collaboration for their help with cluster computing problems in the Monte Carlo simulation.

Andre Booysens of De Beers Mining Company for sharing his knowledge on Charge Coupled Device systems.

Contents

List of Abbreviations

A/D	Analog to Digital.
AMBER	Advanced Multiple Beam Equalization Radiography.
CCD	Charge Coupled Device.
DG	Detector Gain.
DI	Detectability Index.
DQE	Detective Quantum Efficiency.
EMTF	Expectation Modulation Transfer Function.
FOP	Fibre Optic Plate.
FOT	Fibre Optic Taper.
FSSR	Fixed Source Slit/Slot Scanning Radiography.
HVL	Half Value Layer.
IEC	International Electro-Technical Commission.
K	Air Kerma.
LSF	Line Spread Function.
LSSR	Linear Slit/Slot Scanning Radiography.
MICROMEGAS	Micromesh Gaseous Structure.
mR	milliRoentgen.
MTF	Modulation Transfer Function.
NEQ	Noise Equivalent Quanta.
NNPS	Normalised Noise

	Power Spectrum.
NPS	Noise Power Spectrum.
OD	Object to Detector distance.
PGA	Programmable Gain Amplifier.
PSF	Point Spread Function.
QAE	Quantum Absorption Efficiency.
ROI	Region Of Interest.
SC	Source to Collimator distance.
SD	Source to Detector distance.
SDQE	System DQE.
SG	System Gain.
SK	Source to ionisation chamber distance.
SMSA	Scanning Multiple Slit Assembly.
SMTF	System MTF.
$SMTF_{pre}$	Pre-sampled MTF.
SNR	Signal to Noise Ratio.
SPR	Scatter to Primary Ratio.
TASMIP	Tungsten Anode Spectral Model using Interpolating Polynomials.
TDI	Time Delay and Integrate.

List of Symbols

f_x	Spatial frequency (cycles/mm) in the slit direction.
f_y	Spatial frequency (cycles/mm) in the scan direction.
f	Two dimensional spatial frequency variable $f = (f_x, f_y)$.
y	Distance in the scan direction (mm).
x	Distance in the slit direction (mm).
$T_i(f)$	Modulation transfer function of an individual stage in the cascaded linear model.
$S_i(f)$	Noise Power Spectrum of additive noise at the i th stage.
$\bar{s}_i$	Mean number of scattered radiation quanta at the i th stage.
$MTF_i(f)$	Modulation transfer function of the system up to and including the i th stage.
$NPS_i(f)$	Noise Power Spectrum of the system up to and including the i th stage.
$\bar{q}_i$	Mean number of signal quanta resulting from the primary radiation fluence at the i th stage.
$DQE(f)$	Detector DQE.
$SDQE(f)$	System DQE.
SPR	Scatter to Primary Ratio.
$\Im$	Fourier transform operator.

F_w	Focal spot width.
C_w	Collimator gap width.
$\bar{g}_i$	Mean gain at *i th* stage.
$\bar{\varepsilon}_i$	Poisson excess of the *i th* (gain) stage.
$A_s(E)$	Energy dependant Swank factor associated with gain variance.
geom(x)	LSF of geometrical blur in slit direction.
geom(y)	LSF of geometrical blur in scan direction.
τ_y	Dummy distance variable along scan direction axis in focal spot plane.
$focal(\tau_y)$	Intensity distribution of focal spot in the scan direction.
M_f	Demagnification of the projected focal spot in the slit direction.
$F_1(y)$	Lower limit of integration along focal spot distribution in calculation of the geometric LSF in the scan direction.
$F_2(y)$	Upper limit of integration along focal spot distribution in calculation of the geometric LSF in the scan direction.
t_p	Primary radiation grid transmission.
t_s	Scattered radiation grid transmission.
F_C	FOT Fill factor.
NA	FOT Numerical aperture.
n_{FO}	Transmission of untapered FOT.
m	FOT Demagnification.
n_1	Refractive Index of FOT source medium.

n_2	Refractive index of FOT core.
n_3	Refractive index of FOT cladding.
L_R	Light loss at FOT surface.
T_F	Transmission of fibre core.
T_T	FOT transmission efficiency.
u_p	Linear attenuation coefficient due to the Photoelectric Effect.
u_c	Linear attenuation coefficient due to the Compton Scattering Effect.
p	Density of a material in g/cm^3.
δ	Mass thickness of a material in g/cm^2.
t	Thickness of screen material (mm).
H	Lorentzian fitting parameter for screen MTF.
M_n	The n th moment of screen light output distribution.
$C(E)$	Number of visible photons emitted from the screen per absorbed x-ray of energy E.
τ	Finite phosphor persistence decay time constant.
υ	Scan velocity.
Io	Initial light intensity emitted by screen after stimulation.
d	Thickness of the screen.
B_w	Beam width at the detector.
$I(\lambda)$	Wavelength dependant distribution of light incident on CCD surface.
$Q_{CCD}(\lambda)$	Wavelength dependant distribution of CCD Quantum Absorption Efficiency.
a	Pixel pitch at detector plane (mm).
b	Binning number.
S_{in}	Input signal to CCD.

N_d	Variance of dark noise in CCD (electrons).
N_r	Variance of the read noise in CCD (electrons).
G_c	CCD Output amplifier sensitivity (uV/electron).
N_c	Variance of external circuit and clocking noise (uV).
N_a	Variance of A/D noise and crosstalk (uV).
G_p	PGA amplifier gain (uV/uV).
G_d	Digitisation gain (D/uV).
N_q	Variance of quantization noise (D).
D	Digital units.
r	Radial distance from source.
$Object(f)$	Spatial frequency distribution of the object in a detection task.
$Background(f)$	Spatial frequency distribution of the background in a detection task.
μGy	microGrey.
MTF_{dig}	Digital Modulation Transfer Function.
SNR_{out}	Signal to Noise Ratio at the output of a real detector.
SNR_{ideal}	Signal to Noise Ratio at the output of an ideal detector.
NPS_{dig}	Digital Noise Power Spectrum.
$\Pi(f, a^{-1})$	Comb function. Consists of a train of impulses in the frequency domain spaced at sampling frequency a^{-1}.
MTF_{pre}	Pre-Sampled Modulation Transfer Function.

List of Tables

List of Figures

1 Introduction

The goal of this Masters of Science project is to create a mathematical model of the imaging chain of the Statscan slit scanning full body x-ray machine. The model will serve as a design aid for engineers wanting to optimise the image quality, dose delivered and cost of the x-ray machine. The model will also increase understanding of the image formation process in the Statscan x-ray machine and will allow for intelligent decision making on future technologies. This work is an extension of previous modeling work by the original Statscan design team [1, 2, 3, 4].

1.1 Background and motivation

The Statscan full body x-ray machine is a commercially available digital radiography system that has recently been approved by the Food and Drug Administration in the US and CE marked in Europe. The system utilizes a gridless linear slit scanning geometry in which a narrow fan beam is scanned linearly over the object in synchronism with a linear detector array (see Figure 1-1 and

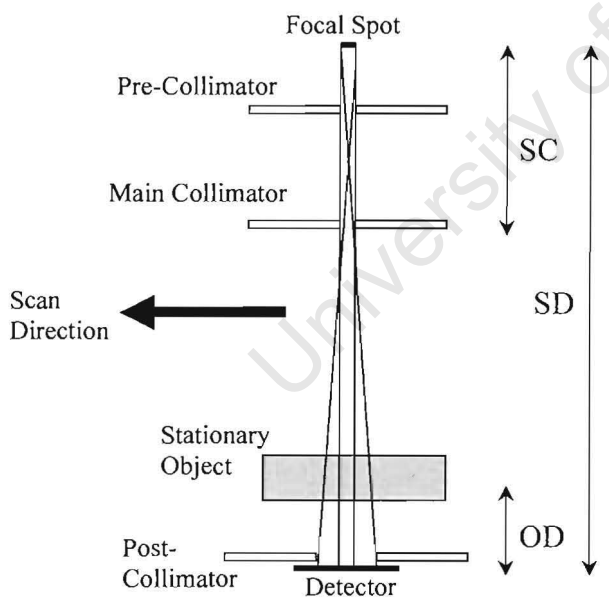

Figure 1-1 Illustration of linear slit scanning principle. The source, detector and collimator seen from the side here are scanned across the object. The narrow fan beam is detected by a screen and projected by fibre optic taper onto a linear array of CCD sensors operating in TDI mode. SC is the Source to Collimator distance, OD the Object to Detector distance and SD the Source to Detector distance.

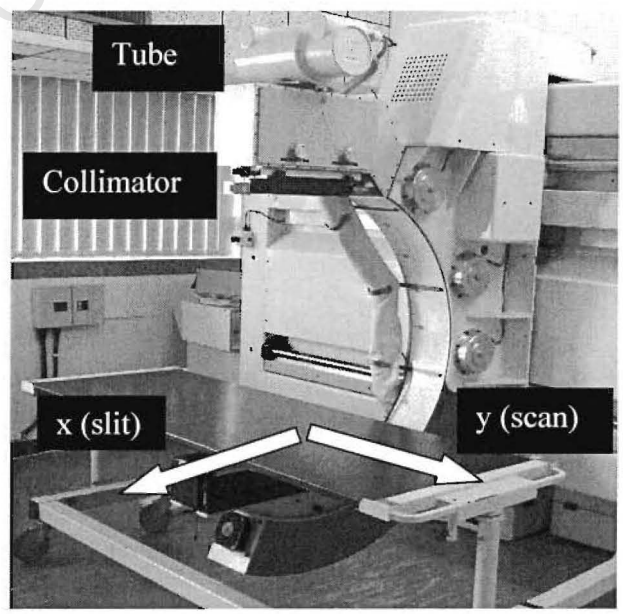

Figure 1-2 Experimental version of the Statscan full body x-ray machine showing the reference axes used in this study.

Figure 1-2). The slit scanning principle is a well known method in radiography [5, 6, 7] to drastically reduce the scatter to primary ratio (SPR) without using a grid. The result is an increased signal to noise ratio (SNR) for a given dose. Entrance doses measured during typical imaging procedures (Skull, Spine, Abdomen, Full Body) for the Statscan system are approximately 10 percent of typical entrance doses for a conventional geometry (wide beam) system [8]. However for lung imaging the slit scanning dose reduction is less marked (at 70 percent) since the low lung density results in a conventional geometry system having a proportionally lower SPR. A further advantage of the linear slit scanning technique is a larger image area (selectable up to 1.8 m x 0.68 m in the case of Statscan) for a given detector size and cost. Figure 1-3, Figure 1-4, Figure 1-5, Figure 1-6 and Figure 1-7 show examples of images from various procedures and patient sizes taken with the Statscan imaging system.

A commonly reported concern [5] with the slit scanning technique is that the low flux usage efficiency results in tube heat loading placing a practical upper limit on image size, quality and duty cycle. This problem has been partly overcome due to the availability of tubes with greater heat loading capacity, increases in detector sensitivity and empirical optimisation of the slit width for a given imaging task.

The Detector DQE has been measured for an earlier version of the Statscan system [9]. Since that study, detector noise and coupling efficiency have been improved and this report presents new NNPS, MTF and DQE measurements for various screens and detector configurations. Furthermore, an expression was developed for these image quality metrics using Cascaded Linear-Systems analysis [10]. The first purpose of this study is to give a comparison and analysis of the predicted and measured detector MTF and DQE.

Although the Detector DQE is a commonly used metric [11] for the rating of x-ray detectors, it does not include system level effects such as scatter, grid attenuation and focal spot geometric blur. At the present time no standard method is available for comparing the imaging versus dose efficiency of entire x-ray systems. A metric for imaging system evaluation that includes system level effects has been suggested and variably named the "System DQE" [12], "Generalized DQE" [13] or "Effective DQE" [7] – in this study the metric is referred to as "System DQE" or SDQE. The second purpose of this study is to present an extended Cascaded Linear-Systems model that includes system level effects and to analyse the effect of various system parameter values on the SDQE. Of specific interest is to use the SDQE concept to compare two systems with identical detectors but different geometries: slit scanning geometry or conventional geometry.

Figure 1-3 Obese poly-trauma patient with tension pneumothorax and fracture of the pelvis. Procedure factors: 120 kV, 160 mA, full scan speed (140 mm/s), 6x6 binning (360 um pixel pitch), large focal spot (1.2x1.2 mm), narrow collimator gap width (0.4 mm).

Figure 1-4 Full spine lateral, medium sized patient. Procedure factors: 145 kV, 200 mA, half scan speed, 8x8 binning (420 um pixel pitch), large focal spot (1.2x1.2 mm), wide collimator gap width (1 mm).

Figure 1-5 Full body scan pediatric patient. Procedure factors: 80 kV, 100 mA, full scan speed (140 mm/s), 4x4 binning (240 um pixel pitch), small focal spot (0.6x0.6 mm), narrow collimator gap width (0.4 mm).

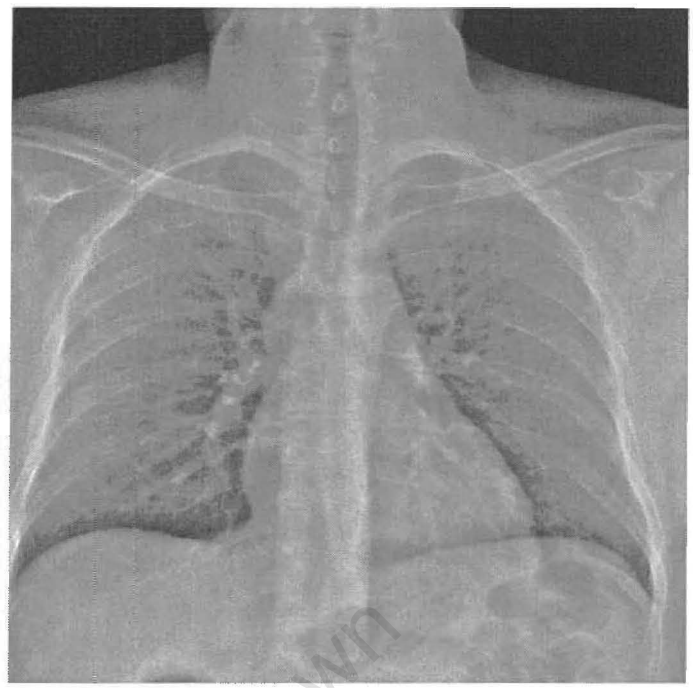

Figure 1-6 Chest, medium sized patient. Procedure factors: 120 kV, 125 mA, full scan speed (140 mm/s), 2x2 binning (120 um pixel pitch), small focal spot (0.6x0.6 mm), narrow collimator gap width (0.4 mm).

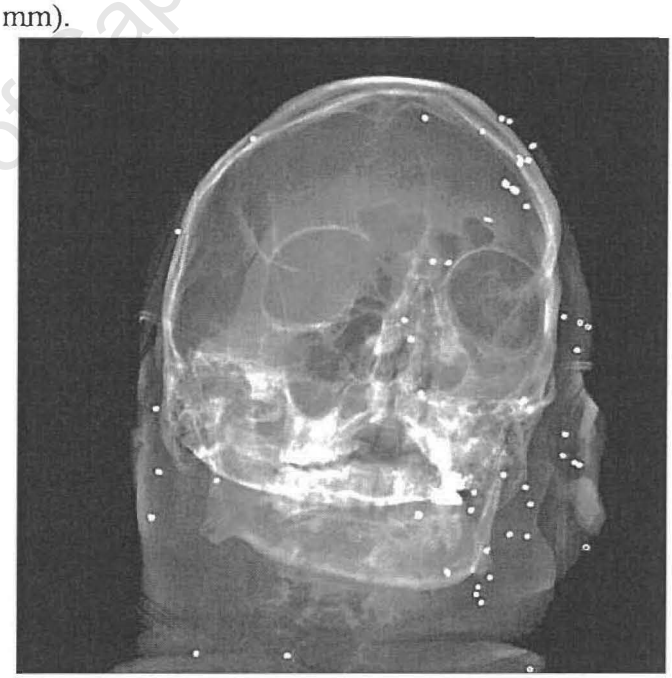

Figure 1-7 Skull, large patient – blast victim. Procedure factors: 110 kV, 160 mA, full scan speed (140 mm/s), 4x4 binning (240 um pixel pitch), small focal spot (0.6x0.6 mm), narrow collimator gap width (0.4 mm).

1.2 Principle of operation of the Statscan system

A narrow and vertical fan beam 3-6 mm in width and 700 mm long (at detector) is scanned linearly over the patient and detected by a radiographic screen of similar size and shape as the fan beam. The beam shape is set by two slits or "collimators" as shown in Figure 1-1. A post-collimator at the detector removes any scattered radiation outside of the primary main beam area. The entire primary beam is detected – no radiation is "lost" outside the sensitive area of the detector. The source and detector are mounted on a C-arm (see Figure 1-2) that can rotate up to 90 degrees – allowing lateral scans to be taken without repositioning of the patient. Three scans speeds can be selected: 35, 70 and 140 mm/s.

The detector consists of a screen (Gd_2O_2S:Tb, 130 mg/cm^2) optically coupled by fibre optic taper (FOT) to twelve scientific grade CCDs operated in Time Delay and Integrate mode (TDI) [14]. This configuration is illustrated in Figure 1-8 and Figure 1-9. The CCD pixel pitch is 27 μm and the basic image pixel pitch is 60 μm due to the FOT demagnification of 2.3. For each image acquisition, pixels can be binned at the CCD line register level to allow selection of an image pixel pitch of for example 60, 120, 240, 360 or 480 μm. The FOT butts are arranged diagonally so that neighboring CCD's receive overlapping data. This allows an "unbutting" software algorithm to completely remove butting artefacts.

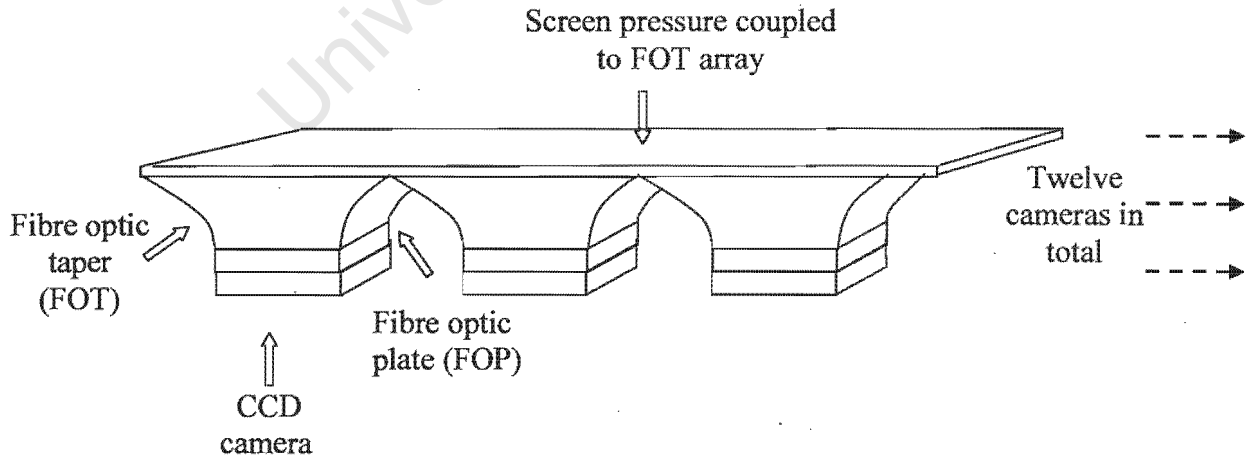

Figure 1-8 Schematic of detector. In the current configuration, the detector has the following parameters: CCD pixel size: 27 um, Image pixel size 60 um, FOT demagnification: 2.3, Screen type: Gd_2O_2S:Tb 130 mg/cm^2, Detector length 690 mm, Detector width 15 mm, Number of CCD's: 12.

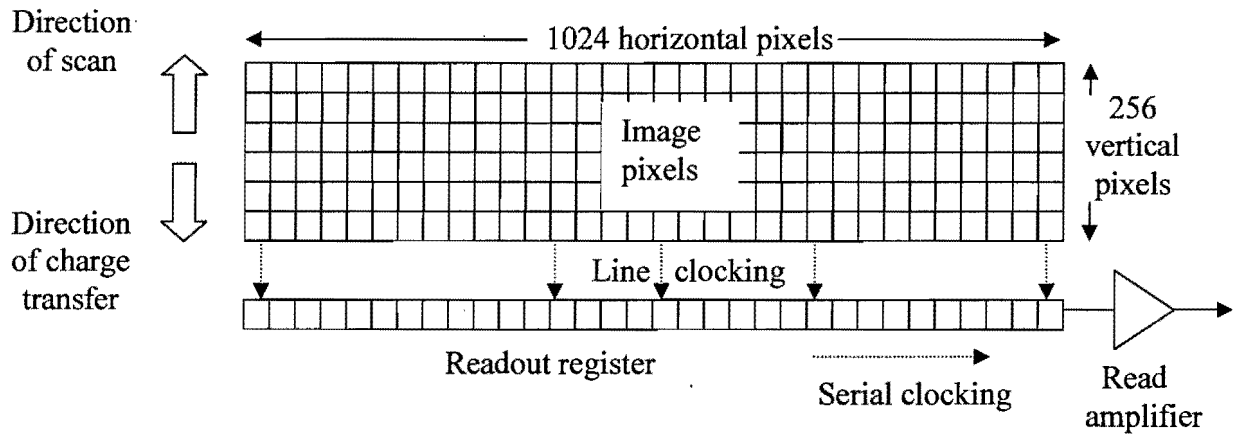

Figure 1-9 Illustration of image acquisition by the TDI effect in the CCD.

Multiplicative structured noise due to spatial variation of sensitivity in the screen, FOT and CCD are compensated for by a gain and offset correction algorithm similar to that described by Samei [15]. The structured noise is less pronounced in the scan direction due to the TDI integration effect.

In slit scanning systems, tube output fluctuations and scan speed variations introduce banding in the scan direction. These effects are lessened by designing the C-arm to dampen anode vibration and the linear drive induction motor was chosen to allow a high degree of scan speed accuracy. The TDI integration effect serves to further lessen image banding in the scan direction. The x-ray tube is mounted with the plane of the rotating anode in the slit direction. As a result, the Heel effect occurs in the scan direction and is of no consequence since the slit is open only to a narrow portion of the beam. Image post-processing includes log compensation, dynamic range compression, geometric distortion correction, camera overlap unbutting and various noise reduction and filtering image processing algorithms.

2 Literature Review

2.1 Detector and System quality metrics

2.1.1 Definition and interpretation of NPS, MTF and DQE

The Modulation Transfer Function (MTF) and Detective Quantum Efficiency (DQE) are commonly used metrics for quantification of the signal and noise transfer properties of detectors in radiographic imaging systems [11]. The metrics are intended to describe linear, shift invariant systems with wide sense cyclo-stationary noise properties. In situations where the system is not shift invariant – for example in digitally sampled systems with aliasing, the MTF and DQE need to be interpreted with caution [16].

The signal transfer properties of the detector up to but not including the sampling stage are described by the spatial frequency dependant pre-sampled MTF which is defined as:

$$MTF_{pre}(f) = \frac{\left|\Im[PSF(x,y)]\right|}{\left|\Im[PSF(x,y)]_{f=0}\right|}, \tag{2-1}$$

where $PSF(x,y)$ is the pre-sampled output response of the detector defined in Cartesian coordinates to a Dirac-Delta function at the input plane of the detector.
In digitally sampled systems, the sampling operation can be modelled as a convolution in the frequency domain with a train of impulses spaced at the sampling frequency. As a result, the spatial frequency dependant digital MTF can be defined as:

$$MTF_{dig}(f) = MTF_{pre}(f) * \Pi(f, a^{-1}) \tag{2-2}$$

Where $\Pi(f, a^{-1})$ is a train of impulses in the frequency domain spaced at the sampling frequency a^{-1}. The digital MTF is essentially the sum of several copies of the pre-sampled MTF that have been shifted along the frequency axis by the sampling frequency. If the pre-sampled MTF modulated signal, contains information above the Nyquist frequency (equal to half the sampling frequency), aliasing occurs which is the contamination of data below the Nyquist

frequency by data above the Nyquist frequency. Such a system where aliasing occurs is termed an under-sampled system. An under-sampled system described by the digital MTF can no longer be defined as shift invariant since the digital MTF depends on the phase of the input Dirac-Delta function with respect to the sampling function [16, 17]. For this reason investigators have defined an Expectation MTF (EMTF) [18] that is the average of the digital MTF over all phases and is a shift invariant descriptor of digitally sampled systems.

The spatial frequency dependant Noise Power Spectrum of the digital output image is a measure of the variance of the image noise at each spatial frequency [16]. The digital NPS (NPS_{dig}) can be calculated from a flat field image by dividing the image into M partially overlapping rectangular regions of interest (ROIs) of width R pixels and applying the following equation [11]:

$$NPS_{dig}(u_n,u_k)=\frac{\Delta x\Delta y}{M\times R^2}\sum_{m=1}^{M}\left|\sum_{i=1}^{R}\sum_{j=1}^{R}\left(I(x_i,y_j)-Mean_M\right)\times e^{-2\pi i(u_n x_i+v_k y_j)}\right|^2 \tag{2-3}$$

Where u and v are the orthogonal spatial frequency variables with units of cycles/mm, Δx and Δy are the mean pixel spacings in the x and y directions respectively, $I(x_i,y_j)$ is the image intensity at pixel coordinate (i, j) and $Mean_M$ is the mean pixel value of the M_{th} region of interest.

The spatial frequency dependant DQE of a linear, shift invariant detector is defined as:

$$DQE(f)=\frac{SNR_{out}^2}{SNR_{ideal}^2} \tag{2-4}$$

and is a measure of the extent that the squared signal to noise ratio is increased by a detector at each spatial frequency. The denominator represents the maximum squared signal to noise ratio that could be obtained given the quantum image at the input to the detector and is equal to the mean number of input photons per unit area at the detector input $\bar{q}$ (for the case of a Poisson distributed quantum image at the input). The numerator in equation 2-4 represents the actual squared SNR at the output of the detector and is given by:

$$SNR_{out}^2=\frac{d^2MTF_{pre}^2(f)}{NPS_{dig}(f)}, \tag{2-5}$$

Where $NPS_{dig}(f)$ is the digital Noise Power Spectrum measured at the output of the detector with sampling and aliasing effects included. By combining equations 2-4 and 2-5, the DQE can be rewritten as:

$$DQE(f) = \frac{\bar{d}^2 MTF_{pre}^2(f)}{\bar{q} NPS_{dig}(f)}, \tag{2-6}$$

where $\bar{d}$ is the mean output signal.

It should be noted that the effects of sampling and aliasing of the noise power spectrum are included, but the effects of signal aliasing are not since it is the pre-sampled MTF and not the digital MTF that appears in the definition of the DQE. Although signal aliasing is a form of image noise, it is not included since it is not a shift invariant effect and is dependant not purely on the detector properties, but also on the signal present in the input image [16].

2.1.2 Measurement of MTF and DQE

The International Electro-technical Commission (IEC) has recently introduced IEC 62220-01 [11] – a document that stipulates a standard for the measurement of the MTF and DQE of digital radiography detectors. The methodology described in IEC 62220-01 is based on previous measurements carried out in laboratories and has been described in detail elsewhere [20, 21]. It is interesting to note that it is stated in the IEC standard that the methodology described therein does not apply to scanning radiography systems. However as shown by other investigators [9, 22], the method required to take DQE measurements in slit scanning systems requires only slight modification of the IEC standard.

The working equation for the calculation of DQE is Equation 2-6 above and is based on measurable quantities. Quantities required for the calculation are the digital NPS at the detector output, the pre-sampled detector MTF and the mean number of quanta per unit area at the detector input plane used to create the image. The MTF and DQE measurement method is described in more detail in Section 4.2 of this thesis.

Several other investigators made DQE measurements using this method for the purposes of rank-ordering of digital detectors found in the real world [9, 15, 18, 23, 24]. It is however pointed out in IEC 62220-01 and elsewhere [23, 25, 26] that the relationship between DQE and image quality and the performance of human observers is not yet fully understood and that image quality in the real world depends on many factors including the display, anatomic noise, the detection task and the radiographic system itself – not just the efficiency of the detector.

2.1.3 System quality metrics: System MTF and System DQE

The DQE and MTF metrics described above do not fully describe the signal and noise properties of a radiographic system since they pertain only to the detector [13, 26]. System level effects [27] such as geometric blurring resulting from finite focal spot size, the presence of scattered radiation at the detector input and the use of a primary beam attenuating grid [7, 28, 29, 30] affect the resolution and noise properties of the final output image. However they are not included in the formulation of the DQE and the MTF. This problem has been previously recognized and figures of merit for the quantification of system noise and resolution properties have been developed [13, 26]. The system quality metric analogue to the detector DQE has variably been named the "Effective DQE" [7], "Generalized DQE" (gDQE) [26] or "System DQE" (SDQE) [12] and is referred to by the latter name in this study. Kyprianou et al. [26] have included specific system level effects such as the scatter MTF, scatter noise and focal spot blur effects into an expression for the Generalized DQE. Also, previous investigators have derived the relationship between the System DQE and Detector DQE when the effects of grid attenuation and scatter radiation noise are included in the analysis [25].

A general expression for the System DQE can be found by considering Equation 2-6 and taking q as the number of image forming primary quanta per unit area at the object plane (i.e. at the plane where the image is formed) and by defining the pre-sampled MTF as the response of the system to a Dirac-Delta function input at the object plane. The digital NPS measured at the detector output is task dependant and is the combination of noise arising from the primary and scattered fluences incident on the detector and additive detector noise. The amount of scattered radiation incident on the detector is dependant on the scattering object, hence the task dependency. In order to take magnification effects into account, the pre-sampled MTF and NPS should be referred to the object plane where the image is formed.

2.2 Image quality and system optimization - SNEQ

An established absolute measure of image quality that applies to linear, shift invariant imaging systems in terms of the SNR at each spatial frequency is the Noise Equivalent Quanta or NEQ [31, 32]. The NEQ at the output of a real detector is the number of Poisson distributed quanta per unit area at each spatial frequency that would be required at the input of an ideal detector to produce at its output the SNR measured at the output of the real detector and can be written as:

$$NEQ(f) = \bar{q}_0 DQE(f) \tag{2-7}$$

or as:

$$NEQ(f) = \frac{[\bar{q}_0 (G) MTF(f)]^2}{NPS(f)} \tag{2-8}$$

where $\bar{q}_0$ is the mean number of input quanta per unit area, G is the large area detector gain factor and $NPS(f)$ is the output image Noise Power Spectrum.

Kyprianou et al. [13, 26] have extended the concept of NEQ to include system level effects and define a Generalized NEQ (which is referred to as the System NEQ or SNEQ in this thesis) as:

$$SNEQ(f) = \bar{q}_0 SDQE(f) \tag{2-9}$$

where f is the spatial frequency variable referred to the object plane (i.e. spatial frequency at the detector plane divided by the geometric magnification). The $SNEQ(f)$ is then an absolute measure of image quality which can be expressed in terms of physical machine parameters and optimised.

Furthermore, it has been shown that for the specific imaging task of detecting a known object against a noisy background, a figure of merit or Detectability Index DI can be defined as [25, 31, 33, 34, 35].

$$DI = \int [Object(f) - Background(f)]^2 SNEQ(f) df \tag{2-10}$$

where *Object(f)* is the spatial frequency distribution of the object to be detected and *Background(f)* is the spatial frequency distribution of the background noise. The Detectability Index is a measure of the detection performance of an ideal observer and is an upper bound on the performance of a human observer in a similar detection task [31].

2.3 Cascaded Linear-Systems theory

Cascaded linear modeling of detectors in radiography is a well established method for analyzing detector performance in terms of physical parameters. Investigators [33, 34, 37, 38, 39, 40, 41, 42, 43] have used the Cascaded Linear-systems theory to predict Detector MTF and DQE and System quantities such as the SMTF and SDQE [13, 25, 26, 27, 35] to a high degree of accuracy.

In the theory of Cascaded Linear-Systems analysis the imaging system is divided into discrete stages that have an effect on the signal and noise as they propagate through the system [10, 32, 44]. Cascaded Linear-Systems analysis relies heavily on frequency domain analysis and requires that the system be Linear, Shift Invariant, Ergodic, and should have wide sense cyclo-stationary noise properties. The system under study is assumed to approximately meet the last two requirements and is shown to be approximately linear and shift invariant in the results and discussions section.

At the *i* th stage in the Cascaded Linear-Systems Model, the signal and noise are represented by a distribution of quanta $q_i(x,y)$ and by the frequency domain Noise Power Spectrum $NPS_i(f)$ respectively, where $f=(f_x,f_y)$ is the two dimensional spatial frequency variable. Each stage modifies the signal and noise in a specific way and the output from each stage serves as the effective input to the next stage. Five different stage types in a cascaded linear model can be identified [10, 32, 44]:

2.3.1 Quantum gain

The number of quanta representing the quantum image is increased by a factor g_i where g_i is the quantum gain of the stage. The gain may be stochastic with a greater than unity variance or it

may be deterministic with unity variance. The mean number of quanta and NPS are transferred according to:

$$\bar{q}_i = \bar{g}_i \bar{q}_{i-1} \tag{2-11}$$

and

$$NPS_i(f) = \bar{g}_i^{\,2} NPS_{i-1}(f) + \bar{q}_{i-1}\sigma_i^{\,2}. \tag{2-12}$$

where $\sigma_i^{\,2}$ is the variance of the gain and $\bar{q}_i$ is the mean number of quanta at the i th stage. The fluctuations in the gain can also be described by a Poisson excess term ε_i which is how much the gain fluctuation exceeds a Poisson distributed gain fluctuation (in a Poisson distributed gain fluctuation, the variance is equal to the mean number of quanta). The Poisson excess is defined as follows:

$$\varepsilon_i = \frac{\sigma_i^{\,2}}{\bar{g}_i} - 1. \tag{2-13}$$

The NPS transfer of a Gain Stage can then be restated as:

$$NPS_i(f) = \bar{g}_i^{\,2} NPS_{i-1}(f) + \bar{q}_{i-1}\bar{g}_i(\varepsilon_i + 1). \tag{2-14}$$

2.3.2 Binary selection:

The binary selection stage is a special case of the quantum Gain Stage with $g \leq 1$. Input quanta either interact with probability g or are discarded with probability (1-g). The mean number of quanta and NPS are transferred according to the following relations:

$$\bar{q}_i = \bar{g}_i \bar{q}_{i-1} \tag{2-15}$$

and

$$NPS_i = \bar{g}_i^{\,2}\left(NPS_{i-1} - \bar{q}_{i-1}\right) + \bar{q}_{i-1}\bar{g}_i. \tag{2-16}$$

The term $\bar{q}_{i-1}$ to the right of the plus sign Equation 2-16 refers to the uncorrelated component of the input noise power spectrum and the bracketed expression refers to the correlated component. So in a binary selection stage the correlated component of the NPS is transferred through the mean gain squared and the uncorrelated component through the mean gain.

2.3.3 Quantum scatter

Quanta are redistributed randomly in the spatial domain with a probability distribution described by the stage Point Spread Function (PSF). The NPS is transferred according to:

$$NPS_i = (NPS_{i-1} - \bar{q}_{i-1})MTF_i^2(f) + \bar{q}_{i-1} \tag{2-17}$$

where $MTF_i^2(f)$ is the Fourier transform of the stage PSF.

Only the correlated component is modulated by the squared MTF meaning that an uncorrelated distribution of quanta will have an NPS unaffected by a Quantum Scatter Stage alone. The mean number of quanta is unaffected by a Quantum Scatter Stage.

2.3.4 Deterministic blur

In a deterministic blur stage the input NPS is modulated by the square of the stage MTF giving:

$$NPS_i(f) = NPS_{i-1}(f)MTF_i^2(f) \tag{2-18}$$

The mean number of quanta is unaffected by a deterministic blur stage (unless the quanta are integrated in an aperture with area differing from unity).

2.3.5 Additive noise:

The NPS of the additive noise is added to the stage NPS according to

$$NPS_i(f) = NPS_{i-1}(f) + S_i(f), \tag{2-19}$$

where $S_i(f)$ is the NPS of the additive noise at the *i*th stage.

If further stages occur after an Additive Noise Stage with an uncorrelated quanta component then it is necessary to treat the additive noise as a separate fluence with an NPS and a mean number of quanta. The uncorrelated component of the additive noise must then be propagated through the rest of the system. An example of this is the scattered radiation additive noise that is added at stage three in this work as an uncorrelated distribution of quanta.

2.4 Classification of digital projection x-ray imaging systems

A digital projection x-ray imaging system typically consists of an x-ray source and detector (the image acquisition sub-system) and an image display sub-system. The characterization and optimisation of the image acquisition sub-system is the main focus of this study.

A number of x-ray machine geometry configurations are possible: In a conventional or "wide beam" [15] geometry system, x-rays radiate from the source and are collimated to expose the region of the patient that is to be imaged. The x-ray detector is placed behind the patient and the image contrast results from the differences in attenuation of the different tissues and materials in the patient (eg. bone and soft tissue). One disadvantage of wide beam systems is that a large amount of scattered radiation [30] is detected along with the primary image information which reduces the SNR of the image information detected. Various approaches have been taken to solve this problem – for example a focused grid [28, 29] posterior to the patient preferentially attenuates scattered x-rays. This leads to a lower Scatter to Primary Ratio (SPR) at the detector but also reduces [46, 47] the primary radiation detected by a certain fraction. Another method of reducing the Scatter to Primary Ratio is to modify the geometry of the acquisition system to either a "flying spot configuration" [48] or a "slit or slot scanning" configuration [49]. In these systems the instantaneous field size is small which results in a reduction in the amount of scatter detected along with the primary beam – without attenuation of the primary beam. Limited success has been realised until now with the flying spot configuration because of long acquisition times and practical heat loading considerations.

2.5 Scanning slit/slot radiography systems

In a slit or slot scanning configuration the radiated x-rays are collimated to a fan beam shape and the beam is scanned over the patient and detected either by a moving detector of similar size as the fan beam from which the image is built up or by a stationary full field detector [5, 6, 7, 14, 22, 43, 49, 50, 51, 52, 53, 54, 55, 56, 57, 58, 59, 60, 61, 62, 63, 64, 65].

A slit scanning system can either be of the "Scanning multiple Slit Assembly" SMSA [54, 65] type or of the "Scanning Single Slit Assembly" type. Multiple slit assemblies have greater flux utilization efficiency than single slit assemblies since the flux emitted by the tube is used simultaneously by several beams. However, potential disadvantages in SMSA's include scatter, cross talk [2] between the beams and difficulty of alignment of the main collimating slits with the post-collimator slots.

It is possible to distinguish between two additional configuration categories in slit scanning systems [66]: The "Linear slit/slot scanning radiography" (LSSR) configuration and the "Fixed Source slit/slot scanning Radiography" (FSSR) configuration. In the LSSR configuration, the source scans along a linear path in synchronism with the fan beam and the detector as it is scanned over the patient, whiles in the FSSR configuration, the source is fixed and the fan beam sweeps a radial path whiles scanning over the patient.

A slit scanning system may have a slot or "post-collimator" [5, 53] posterior to the patient which serves to further reduce the scattered radiation detected (since a slot has a limited acceptance angle). Deeper slots have superior scatter suppression properties [53].

In general slit scanning systems have the advantage of low dose image acquisition, and the possibility of a large image area. Disadvantages include the necessity of using a narrow slit to preserve spatial resolution in the scan direction – using a narrow slit reduces the flux utilization efficiency and hence introduces tube heat loading limitations. Also, tube output fluctuations introduce image non-uniformities and there are typically difficulties in aligning the post-collimating slot at the detector with the beam forming slit.

The slit scanning system configuration has a major advantage in terms of its lower SPR and lower dose, but other disadvantages such as the difficulty of mechanical alignment of the collimator and

detector, expense of moving parts, scan speed uniformity and stringent tube heat loading requirements need to be considered. Several existing embodiments of the slit scanning system configuration are described in the following sub-sections.

2.5.1 AMBER - "Advanced Multiple Beam Equalization Radiography"

The acronym AMBER expands to "Advanced Multiple Beam Equalization Radiography" and is the name of a dedicated chest imaging system [58]. The AMBER system combines slit scanning with screen film detection. Typically, screen film alone would not be adequate for the high contrast ranges present in a chest image. The solution provided by AMBER is to modulate the beam according to the measured exposure levels achieved at various points in the image. The exposures are measured by an x-ray translucent set of 20 Xenon filled ionisation chambers placed above the detector. The measured exposure level is fed back electronically to 20 piezoelectric actuated beam modulators that attenuate the slit beam according to the amplitude of the measurement from the corresponding ionisation chamber. In this way denser areas of the chest receive greater exposure and vice versa. The result is a more uniform exposure of the film and the potential for simultaneous viewing of the mediastinum and lung areas.

Chest scanning is a particularly useful application for digital equalization radiography systems because of the large range of attenuations present in the chest [58]. The large dynamic range provided by the beam modulation system is suited to simultaneous viewing of the lung and mediastinum. Also, the slit scanning configuration helps to reduce the SPR in the mediastinum area.

2.5.2 Low-Dose Gas Microstrip Detector

The EOS [22, 51] system is a dual view orthopaedic radiography system built by Biospace Instruments in Paris, France. The system is orientated vertically so that bone examinations are undertaken under full patient loading which is desirable for certain orthopaedic examinations. The vertical slit scanning modality has been utilized previously for orthopaedic purposes, particularly for low-dose Scoliosis and Lordosis assessment [56]. The EOS system is based on the linear slit scanning radiography principle (the source moves along a linear path during a scan) and each of

the two detector and source assemblies angled at 90 degrees consist of a single beam shaping slit, a post collimator and a gas microstrip detector. The post-collimator is a 0.5 mm wide slit and the detector is based on the Micromesh Gaseous Structure (MICROMEGAS) technology [22] which has been described elsewhere [52]. Incident photons interact mostly by the Photoelectric effect in an "interaction zone" containing 10 cm of Xenon gas pressurized at 6 atmospheres. The photo-electrons then drift to a conversion zone where a strong electric field causes avalanche gain and guides the resulting electrons to detecting electrodes and associated signal amplifiers. The detecting electrodes are spaced at a pitch of 254 um which sets the slit direction pixel pitch. The scan direction pixel pitch is also set to 254 um by adjusting the scan speed (which has a maximum of 150 mm/s) and integration time.

The MTF of the microstrip gas detector is anisotropic (i.e. dependant on direction) and is energy dependant particularly in the scan direction. Frequency values at which the MTF drops to half its full value were measured at 1.0, 0.90 and 0.76 mm^{-1} in the slit direction and at 0.97, 0.95 and 0.92 mm^{-1} in the scan direction for beams having half value layers of 1.8, 3.4 and 5.1 mm Al. The fact that resolution is energy dependant suggests that spatial image artefacts would be a problem in dual-energy imaging. The energy dependence and limitation of the resolution in the slit direction in the EOS system result from the fact that higher energy photoelectrons have a longer range in the Xenon gas filled conversion zone in the detector. The resolution limitations in the scan direction are set by the width of the post-collimating slit. A narrower post-collimating slit would improve the detector resolution, but would reduce tube flux utilization efficiency and the DQE.

The DQE of the gas detector could potentially be high because of good stopping power at the beam qualities used and low detector noise. In reality, the DQE is limited by alignment problems resulting in a portion of the fan beam contributing to patient dose but falling outside the post-collimating slit and hence failing to contribute to the detector input signal. The DQE exhibits remarkably low exposure dependence due to the low additive noise in the detector – possibly a result of signal amplification. In a similar fashion to the MTF the DQE is highly sensitive to beam quality with harder, higher kV beams resulting in a greatly reduced DQE.

The measured DQE values in the scan direction ranged between 0.14 and 0.2 at 0.5 mm^{-1}, 0.05 and 0.06 at 1.0 mm-1 and 0.00 and 0.01 at 1.5 mm^{-1}. In the slit direction the measured values were between 0.13 and 0.15 at 0.5 mm-1, 0.08 and 0.11 at 1 mm^{-1} and 0.04 and 0.07 at 1.5 mm^{-1}. The DQE measurement were taken with relatively soft beams having HVL's of 1.8, 3.4 and 5.1 mm Al at 50, 80 and 110 kVp and at doses ranging from 1.3 to 25.8 μGy.

Improvements in the DQE and MTF can be realized by increasing the gas pressure in the conversion zone. This would however lead to the requirement of a sturdier and bulkier gas vessel and potential leakage problems. Also, the increase in gas pressure would lead to increased space charge accumulation which in turn affects the linearity and gain of the detector.

In conclusion, the EOS system is able to take low dose (approximately 10 uGy entrance skin exposure [51]) dual view full body examinations that have sufficient image quality for usage in Scoliosis examinations and surgery planning. High resolution, low noise imaging is limited due to the soft beam limitation imposed by the gas detection technique.

2.5.3 ThoraScan

ThoraScan [63] is a digital slot-scanning dedicated chest imaging system from Delft Imaging Systems in the Netherlands. ThoraScan has the advantage of the large dynamic range of digital detectors which is necessary for the large range of attenuations present in the chest [7]. Also, the efficient scatter suppression of the slit scanning geometry is useful when imaging the highly attenuating mediastinum area in the chest.

ThoraScan [64] is based on the Scanning Single Slit principle and is an FSSR system meaning that the source is fixed during a scan and the fan beam follows a radial path. The detector [6] consists of 500 um of Thallium doped CsI directly coupled by fibre optic plate to CCD's operated in TDI mode. This detector arrangement has a potentially high DQE since the 500 um thick CsI is arranged in a columnar structure leading to a good MTF combined with high x-ray absorption efficiency and the straight coupling arrangement leads to minimal light loss and the lack of a high frequency drop in the spatial frequency dependant DQE. Although the ThoraScan detector design is expected to have a high DQE, in reality the measured DQE is relatively low and exhibits high exposure dependence. The generally low DQE values can be attributed to beam alignment problems resulting in flux that contributes to dose without falling within the sensitive area of the detector (in a similar fashion to the low dose microstrip detector - see Section 2.5.2). The high exposure dependence of the DQE is most likely a result of excessive additive electronic noise in the CCD and output electronics.

In a comparative study of image quality with an indirect conversion digital conventional geometry grid system (XQ/I, GE medical systems) similar image quality was obtained by ThoraScan in the lung region and superior image quality was obtained in the denser mediastinum areas by the

ThoraScan system using about 37 % less dose [63]. The improvement in image quality in the denser regions can mainly be attributed to the lower scatter fractions obtained by ThoraScan. Both systems in the study were digital with the associated high dynamic range allowing simultaneous viewing of the lung and mediastinum areas.

3 Derivation of Cascaded Linear-systems Model

A Cascaded Linear-Systems Model of the Statscan system was developed that includes stages identified in the detector as well as system level effects [13, 27] such as focal spot blurring, grid attenuation and scattered radiation incident. Table 3-1 shows the stages and parameters used in the Cascaded Linear-Systems model. The inclusion of stages before absorption in the screen is something of a departure from traditional cascaded linear models. An attempt was made to select stages that have the largest effect on system image quality metrics. Error due to omission of certain minor stages is discussed in the results and discussion section.

Table 3-1: Stage parameters and descriptions for Cascaded Linear-Systems model.

Stage #	Stage Parameters	Stage Type	Stage Description
i = 0	$\bar{q}_0$		Initial primary flux
i = 1	$T_1(f)$	Quantum scatter	Focal spot and beam divergence blurring
i = 2	G_2	Binary selection	Grid attenuation of primary beam
i = 3	S_3	Additive noise	Scattered radiation incident on detector
i = 4	g_4	Binary selection	Quantum absorption efficiency of screen
i = 5	g_5, ε_5	Quantum gain	Screen conversion gain and Poisson excess
i = 6	$T_6(f)$	Quantum scatter	Light spreading in screen
i = 7	$T_7(f)$	Quantum scatter	"Image Smear" in the scan direction due to finite phosphor persistence
i = 8	g_8	Binary selection	Coupling efficiency between screen and CCD
i = 9	$T_9(f)$	Deterministic blur	Pixel aperture
i = 10	S_{10}	Additive noise	Read Noise, dark noise, external circuit electronic noise and quantization noise.

3.1 Application of cascaded linear model

In this section for each stage identified in Table 3-1, the signal and noise are propagated according to the transfer properties described in Section 2.3. The initial input to the system is a spatially uncorrelated distribution of quanta with Poisson mean and variance. For convenience, the stage parameters are described in terms of the two dimensional frequency variable *f*. When the results are combined, the resultant NPS, MTF and DQE are split into their component directions as a function of f_x and f_y [43]. At the end of this section, the system MTF, NPS and DQE are calculated in terms of system parameters. The values for each system parameter are then derived (see Section 4.1) from measurement and theory.

3.1.1 Stage 0: Incident quanta

The initial primary signal or quantum image is an uncorrelated Poisson distribution of quanta with mean fluence $\bar{q}_o$ and Noise Power Spectrum given by [32]:

$$NPS_0(f) = \bar{q}_o . \tag{3-1}$$

3.1.2 Stage 1: Quantum scatter – Focal spot and beam divergence

Focal spot blurring in the slit direction and beam divergence in the scan direction are treated as a Quantum Scatter Stage [13]. The uncorrelated quantum image is passed by a stochastic convolution through the stage point spread function [32]. The NPS is therefore transferred according to Equation 2-17 and the mean number of quanta is unaffected yielding:

$$NPS_1(f) = NPS_0(f) = \bar{q}_o \tag{3-2}$$

and

$$\bar{q}_1 = \bar{q}_o . \tag{3-3}$$

It should be noted that the slit direction component of the system MTF is at this point equal to the slit direction component of $T_1(f)$ which arises as a result of finite focal spot size. The scan direction component of $T_1(f)$ arises from beam divergence in the scan direction.

3.1.3 Stage 2: Binary selection – Grid attenuation

The hypothetical grid used in this model transmits incident primary photons with probability given by $(1-\bar{g}_2)$. Applying Equations 2-15 and 2-16 for a binary selection stage gives:

$$NPS_2(f) = \bar{g}_2\bar{q}_o \tag{3-4}$$

and

$$\bar{q}_2 = \bar{g}_2\bar{q}_o \tag{3-5}$$

3.1.4 Stage 3: Additive noise – Scattered radiation incident

In this study, scatter is treated as a noise term. In a digital system, the DC signal offset introduced by scatter can be removed and therefore has no direct effect on image contrast in the way that it does in screen film imaging. However, the quantum fluctuations of the scattered photon fluence incident on the detector do introduce noise that has a direct effect on image quality and should therefore be included in the analysis.

The scattered radiation field incident is assumed to be an uncorrelated Poisson distribution of quanta [27]. The NPS of the scattered radiation $S_3(f)$ is therefore equal to the mean number of scattered quanta incident per mm^2 $\bar{s}_3$. Note that $\bar{s}_3$ is the mean number of scattered photons incident on the detector *after* the scattered radiation field has been attenuated by the grid.

From this point onwards, the noise transfer for the primary and scattered cases are considered separately. The resultant mean fluence and NPS at this stage is therefore given by the sum of the contributions due to the mean primary fluence and mean scattered fluence yielding:

$$NPS_3(f) = \bar{g}_2\bar{q}_o + \bar{s}_3 \tag{3-6}$$

and

$$\bar{q}_3 + \bar{s}_3 = \bar{g}_2\bar{q}_o + \bar{s}_3 . \tag{3-7}$$

The mean primary fluence is given by the first terms before and after the equality sign in Equation 3-16 and the mean scattered fluence is given by the second terms.

3.1.5 Stage 4: Binary selection – Screen quantum absorption efficiency

In a similar fashion to the analysis of Siewerdsen et al. [27], it is assumed that the difference in spectral distribution between the primary and scattered radiation fields is small. As a consequence, in this model, both quanta distributions go through the same absorption efficiency, quantum gain and spatial spreading stages in the screen. Using Equations 2-15 and 2-16 for a binary selection stage, the NPS at Stage 4 for the scattered and primary contributions is given by:

$$\begin{aligned} NPS_4(f) &= \bar{g}_4{}^2\left[NPS_3(f) - (\bar{q}_3 + \bar{s}_3)\right] + \bar{g}_4(\bar{q}_3 + \bar{s}_3) \\ &= \bar{g}_4(\bar{g}_2\bar{q}_o + \bar{s}_3) \end{aligned} \tag{3-8}$$

and the mean scattered and primary fluences are given by.

$$\bar{q}_4 + \bar{s}_4 = \bar{g}_4\bar{g}_2\bar{q}_o + \bar{g}_4\bar{s}_3 \tag{3-9}$$

3.1.6 Stage 5: Quantum gain – Screen conversion gain

The scattered and primary quanta are converted from x-ray to light quanta in the screen [37]. This is a stochastic process with an associated mean gain and gain variance. Application of Equations 2-11 and 2-14 yields the following expressions for the Noise Power Spectrum and mean number of quanta:

$$NPS_5(f) = (1 + \frac{\bar{s}_3}{q_o \bar{g}_2}) \left[\bar{g}_5 \bar{g}_4 \bar{g}_2 \bar{q}_0 + \bar{g}_5^{\,2} \bar{g}_4 \bar{g}_2 \bar{q}_0 (\frac{\varepsilon_2}{\bar{g}_5} + 1) \right] = (1 + \frac{\bar{s}_3}{q_o \bar{g}_2}) \bar{g}_5 \bar{g}_4 \bar{g}_2 \bar{q}_0 \left[1 + (\varepsilon_5 + \bar{g}_5) \right] \quad \text{(3-10)}$$

and

$$\bar{q}_5 + \bar{s}_5 = \bar{g}_5 \bar{g}_4 \bar{g}_2 \bar{q}_o + \bar{g}_5 \bar{g}_4 \bar{s}_3 . \quad \text{(3-11)}$$

It is worth noting at this stage that term $\frac{\bar{s}_3}{q_o \bar{g}_2}$ is equal to the scatter to primary ratio (SPR) at the detector (after the grid).

3.1.7 Stage 6: Quantum scatter – Spatial spreading of light quanta in screen

The quanta are redistributed according to the screen Point Spread Function. Application of Equation 2-17 yields the following relations:

$$NPS_6(f) = (1 + \frac{\bar{s}_3}{q_o \bar{g}_2}) \bar{g}_5 \bar{g}_4 \bar{g}_2 \bar{q}_0 \left[1 + (\varepsilon_5 + \bar{g}_5) T_6(f)^2 \right] \quad \text{(3-12)}$$

and

$$\bar{q}_6 + \bar{s}_6 = \bar{g}_5 \bar{g}_4 \bar{g}_2 \bar{q}_o + \bar{g}_5 \bar{g}_4 \bar{s}_3 . \quad \text{(3-13)}$$

The system MTF at this stage is given by:

$$MTF_6(f) = T_1(f) T_6(f) . \quad \text{(3-14)}$$

3.1.8 Stage 7: Quantum scatter – Scan direction blur due to finite phosphor persistence

Two Quantum Scatter Stages in a row (stage 6 and stage 7) are equivalent to one Quantum Scatter Stage with MTF equal to the product of the individual stage MTF's (this is clear from inspection of Equation 2-17) yielding [19]:

$$NPS_7(f_x) = (1+\frac{\bar{s}_3}{q_o\bar{g}_2})\bar{g}_5\bar{g}_4\bar{g}_2\bar{q}_0\left[1+(\varepsilon_2+\bar{g}_5)T_6(f)^2T_7(f)^2\right] \tag{3-15}$$

and

$$\bar{q}_7+\bar{s}_7 = \bar{g}_5\bar{g}_4\bar{g}_2\bar{q}_o+\bar{g}_5\bar{g}_4\bar{s}_3. \tag{3-16}$$

The system MTF at this stage is given by:

$$MTF_6(f) = T_1(f)T_6(f)T_7(f). \tag{3-17}$$

3.1.9 Stage 8: Binary selection – Coupling efficiency between screen and CCD silicon

Application of Equation 2-15 and 2-16 yields:

$$NPS_8(f) = (1+\frac{\bar{s}_3}{q_o\bar{g}_2})\bar{g}_8\bar{g}_5\bar{g}_4\bar{g}_2\bar{q}_0\left[1+\bar{g}_8(\varepsilon_5+\bar{g}_5)T_6(f)^2T_7(f)^2\right] \tag{3-18}$$

and

$$\bar{q}_8+\bar{s}_8 = \bar{g}_8\bar{g}_5\bar{g}_4\bar{g}_2\bar{q}_o+\bar{g}_8\bar{g}_5\bar{g}_4\bar{s}_3. \tag{3-19}$$

3.1.10 Stage 9: Deterministic blur – Integration in CCD elements scan direction

The quanta are integrated in the CCD pixel aperture with dimension axa mm^2. The integration introduces a scaling factor a^2 for the signal and a scaling factor a^4 for the NPS (since the NPS is

related to the squared signal) [19]. The NPS and fluence are modified according to Equation 2-18 giving:

$$NPS_9(f) = a^4(1+\frac{\bar{s}_3}{q_o\bar{g}_2})\bar{g}_8\bar{g}_5\bar{g}_4\bar{g}_2\bar{q}_0\left[1+\bar{g}_8(\varepsilon_5+\bar{g}_5)T_6(f)^2T_7(f)^2\right]\times T_9(f)^2 \quad (3\text{-}20)$$

and

$$\bar{q}_9+\bar{s}_9 = a^2\bar{g}_8\bar{g}_5\bar{g}_4\bar{g}_2\bar{q}_o + a^2\bar{g}_8\bar{g}_5\bar{g}_4\bar{s}_3. \quad (3\text{-}21)$$

The system MTF at this stage is given by:

$$MTF_6(f) = T_1(f)T_6(f)T_7(f)T_{10}(f). \quad (3\text{-}22)$$

3.1.11 Stage 10: Additive noise – External and internal noise sources

At the final stage the additive noise power spectrum is added yielding [38, 39, 40]:

$$NPS_{10}(f) = a^4(1+\frac{\bar{s}_3}{q_o\bar{g}_2})\bar{g}_8\bar{g}_5\bar{g}_4\bar{g}_2\bar{q}_0\left[1+\bar{g}_8(\varepsilon_5+\bar{g}_5)T_6(f)^2T_7(f)^2\right]\times T_9(f)^2 + S_{10} \quad (3\text{-}23)$$

and

$$\bar{q}_{10}+\bar{s}_{10} = a^2\bar{g}_8\bar{g}_5\bar{g}_4\bar{g}_2\bar{q}_o + a^2\bar{g}_8\bar{g}_5\bar{g}_4\bar{s}_3. \quad (3\text{-}24)$$

3.2 Calculation of detector and system image quality metrics: DQE, MTF, NPS

For the purposes of this study it was assumed that aliasing effects are small (due to the low resolution screen and relatively large pixel pitch used in the Statscan system). Methods for including the effects of aliasing on the MTF, DQE and NPS are described in the literature and could be applied in an extension of this study [16, 32]. For example, the detector digital MTF (which includes aliasing) is the pre-sampled MTF convolved with an impulse train spaced at the sampling period (inverse of the sampling frequency).

Also, object magnification effects were ignored (the SDQE is referred to the detector plane) [13]. For an analysis of the effects of magnification, the SMTF and SDQE should be referred to the object plane. However, due to the fixed source to detector distance and relatively small magnification effect in the system under study it was decided not to include magnification effects. Furthermore, the magnification in the linear slit scanning system under study is unity in the scan direction.

3.2.1 System and detector Gain

The system and detector gains relate the number of x-rays quanta representing the input signal to the number of quanta (electrons in the read out register) representing the output signal [40]. The system gain *SG* is given by the product of the primary gains of each stage in the system including the grid:

$$SG = a^2 \bar{g}_8 \bar{g}_5 \bar{g}_4 \bar{g}_2 \tag{3-25}$$

and the detector gain *DG* is given by the product of the gains of each stage in the detector:

$$DG = a^2 \bar{g}_8 \bar{g}_5 \bar{g}_4 . \tag{3-26}$$

3.2.2 System and detector MTF

The component MTF's of the system can be combined multiplicatively so the pre-sampled System MTF (SMTF) in the scan direction can be written as [17]:

$$SMTF(f_y) = T_1(f_y)T_6(f_y)T_7(f_y)T_9(f_y) \tag{3-27}$$

and as

$$SMTF(f_x) = T_1(f_x)T_6(f_x)T_9(f_x). \tag{3-28}$$

in the slit direction.

The detector MTF is found by setting the geometric blur term T_1 to unity in Equations 3-27 and 3-28.

3.2.3 System and detector NNPS and DQE

The results for the theoretical System NPS and System MTF can be combined in an expression for the System DQE using the definition of the System Detective Quantum Efficiency [26]:

$$SDQE(f) = \frac{\bar{q}_0 SG^2 SMTF(f)^2}{NPS_{10}(f)}$$

The System DQE in the scan direction is therefore given by

$$SDQE(f_y) = \frac{\bar{g}_2\bar{g}_4\bar{g}_5\bar{g}_8 T_1(f_y)^2 T_6(f_y)^2 T_7(f_y)^2 T_9(f_y)^2}{(1+\frac{\bar{s}_3}{q_o\bar{g}_2})\left[1+\bar{g}_8(\varepsilon_5+\bar{g}_5)T_6(f_y)^2 T_7(f_y)^2\right]\times T_9(f_y)^2 + \frac{S_{10}}{a^4 q_o \bar{g}_4\bar{g}_5\bar{g}_2\bar{g}_8}} \tag{3-29}$$

and in the slit direction by

$$SDQE(f_x) = \frac{\bar{g}_2\bar{g}_4\bar{g}_5\bar{g}_8 T_1(f_x)^2 T_6(f_x)^2 T_9(f_x)^2}{(1+\frac{\bar{s}_3}{q_o\bar{g}_2})\left[1+\bar{g}_8(\varepsilon_5+\bar{g}_5)T_6(f_x)^2\right]\times T_9(f_x)^2 + \frac{S_{10}}{a^4 q_o \bar{g}_4\bar{g}_5\bar{g}_2\bar{g}_8}} . \quad (3\text{-}30)$$

The Detector DQE is found by setting T1, g2 to unity and S3 to zero in the above equations. This is equivalent to the case with ideal scatter suppression, no grid and no focal spot blurring effects yielding:

$$DQE(f_y) = \frac{\bar{g}_4\bar{g}_5\bar{g}_8 T_6(f_y)^2 T_7(f_y)^2 T_9(f_y)^2}{\left[1+\bar{g}_8(\varepsilon_5+\bar{g}_5)T_6(f_y)^2 T_7(f_y)^2\right]\times T_9(f_y)^2 + \frac{S_{10}}{a^4 q_o \bar{g}_4\bar{g}_5\bar{g}_2\bar{g}_8}} \quad (3\text{-}31)$$

in the scan direction and

$$DQE(f_x) = \frac{\bar{g}_4\bar{g}_5\bar{g}_8 T_6(f_x)^2 T_9(f_x)^2}{\left[1+\bar{g}_8(\varepsilon_5+\bar{g}_5)T_6(f_x)^2\right]\times T_9(f_x)^2 + \frac{S_{10}}{a^4 q_o \bar{g}_4\bar{g}_5\bar{g}_2\bar{g}_8}} . \quad (3\text{-}32)$$

in the slit direction.

Inspection of Equations 3-29, 3-30, 3-31 and 3-32 reveals that for the quantum limited case (S_{10} = 0), the following relationship between the System DQE and Detector DQE holds:

$$SDQE(f) = \frac{\bar{g}_2 T_1(f)^2 DQE(f)}{(1+SPR)} , \quad (3\text{-}33)$$

where

$$SPR = \bar{s}_3 / q_o \bar{g}_2 \quad (3\text{-}34)$$

is the scatter to primary ratio of the radiation incident on the detector after the grid. This result is consistent with the findings of other investigators [7, 27] except for the new addition of the focal spot blur term $T_1(f)^2$.

4 Materials, Methods and Intermediate Results

4.1 Calculation of physical model parameters

4.1.1 Flux incident on detector

In the DQE measurement used to validate the linear Cascaded Linear-Systems Model it is necessary to predict the number of primary photons per mm^2 incident on the detector. This can be done by measuring the incident Air Kerma K with an ionisation chamber and then converting from μGy to photons/mm using a conversion factor. The conversion factor from Air Kerma K in μGy to flux density in photons/mm^2 for a monoenergetic beam in air in the energy range 1-150 keV can be calculated using the following empirically derived equation [68]:

$$\xi(E) = \left[8.76 \times (x + y\sqrt{E}\ln(E) + \frac{z}{E^2}) \right]^{-1}, \tag{4-1}$$

where x = -5.023290717769674e-06, y = 1.810595449064631e-07, z = 0.008838658459816926. E is the energy of the beam in keV and $\xi(E)$ has units of photons/mm^2 per μGy. The factor 8.76 is included to convert from exposure in air (in mR) to Air Kerma (in μGy) i.e. 1 mR = 8.76 μGy.
For a polyenergetic spectrum it is necessary to integrate over the entire spectrum and the conversion from measured Air Kerma to flux density is calculated as follows:

$$\Psi(E_{max}) = \frac{\int_{E=0}^{E=E_{max}} \Phi_o(E)dE}{\int_{E=0}^{E=E_{max}} \xi(E)\Phi_o(E)dE}, \tag{4-2}$$

where $\Phi_o(E)$ is the energy spectrum of the fluence incident on the ionisation chamber, E_{max} is the maximum energy in the spectrum (equal to the peak tube voltage) and $\Psi(E_{max})$ has units of photons/mm^2 per μGy. The numerator of Equation 4-2 represents the total fluence and the denominator represents the sum of contributions of photons at each energy in the spectrum to Air Kerma. Figure 4-1 shows $\Psi(E_{max})$ calculated for kV and filtration thicknesses used in this study.

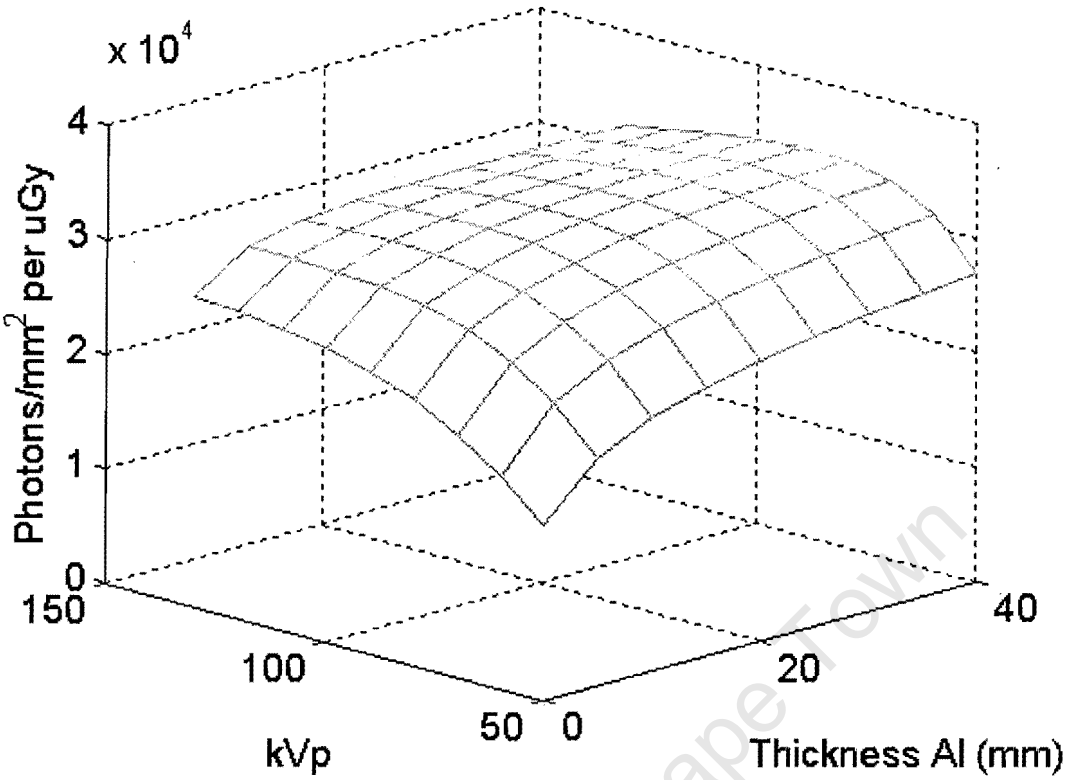

Figure 4-1 Conversion factor $\Psi(E_{max})$ (photons/mm^2 per μGy) calculated as a function of peak tube voltage setting in kVp and additional Aluminium filtration thickness.

To calculate the mean primary incident fluence $\bar{q}_0$ a further conversion factor is required to compensate for the beam divergence over the distance between the ionisation chamber and the detector. In linear slit scanning system, the number of photons/mm^2 decreases only in the slit direction meaning that fluence decreases with a 1/r dependency rather than a 1/r^2 dependency ([9] and see Section 4.2.2). This is because the distance swept by the beam in the scan direction is independent of distance from the source. The mean fluence can then be calculated using:

$$\bar{q}_0 = K \times \Psi(E_{max}) \times \frac{SK}{SD}, \qquad (4\text{-}3)$$

where $\bar{q}_0$ is the mean number of photons/mm^2 incident on the detector, SD is the source to detector distance and SK is the source to ionisation chamber distance.

The incident energy spectrum $q_o(E)$ was calculated using Boone's "Tungsten Anode Spectral model using interpolating polynomials" TASMIP [67] which is a computer routine that generates

tungsten target spectra based on empirical data. TASMIP takes the peak voltage setting and the percentage generator voltage ripple as an input. The generated spectrum was then modified to yield $q_o(E)$ using the Lambert-Beers law [68] for attenuation by the inherent tube filtration, the effective external filtration and a patient equivalent thickness of aluminum. Figure 4-2 shows the raw spectrum before and after attenuation by the inherent tube and external filtration. Mass attenuation coefficients for various materials used in the calculation were obtained from data published by Hubbel et al. [69]. Table 4-1 summarizes the parameters used to generate the raw x-ray spectra and to calculate the conversion factor $\Psi(E_{max})$ for the DQE measurements and simulations in this study. The kVp and patient equivalent thicknesses were chosen to comply with the IEC recommendation for beam qualities in DQE measurement [11]. The discrepancies between the calculated values of $\Psi(E_{max})$ and the IEC recommended values can probably be attributed to differences in the spectrum used to calculate $q_o(E)$.

The accuracy of TASMIP in predicting the Statscan emitted energy spectrum was checked by comparing calculated half value layers (HVL's) with the measured HVL. The HVL at each kVp setting was measured by finding the thickness of Aluminium needed to reduce the beam Air Kerma by half. Care was taken to reduce measured scatter by placing the thickness of Aluminum above the collimator. The corresponding predicted HVL was calculated by attenuating

Table 4-1: IEC 62220-1 recommended beam qualities used in this study

	RQA3	**RQA5**	**RQA7**	**RQA9**
Peak tube voltage setting	50	70	90	120
External filtration (mm Al)	1	1	1	1
Inherent tube filtration (mm Al)	0.9	0.9	0.9	0.9
Percentage voltage ripple on generator	0	0	0	0
Patient equivalent Aluminium (mm)	10	21	30	40
Calculated $\Psi(E_{max})$ (photons/mm2 per µGy)	22737	31375	33511	32307
IEC [11] recommended conversion (photons/mm2 per µGy)	21759	30174	32362	31077

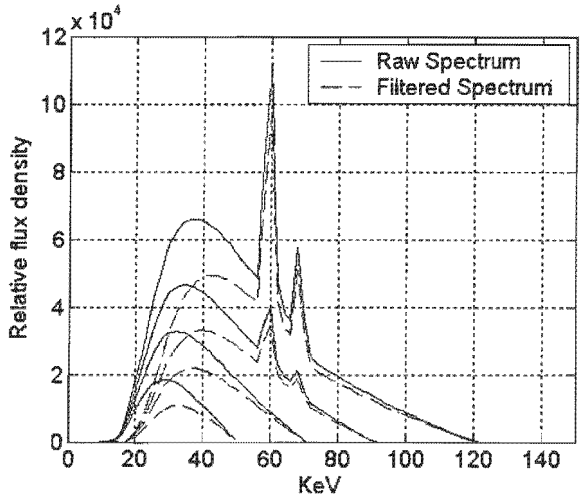

Figure 4-2 TAMSIP generated spectra in simulation of the Statscan beam before and after filtration by the inherent tube and external filtration (1.9 mm of Aluminium total)

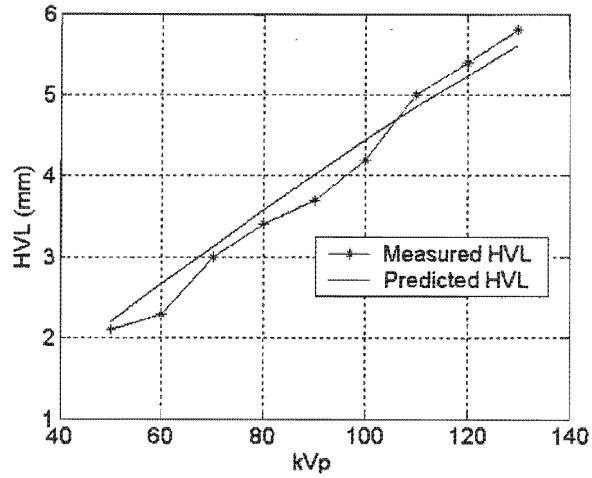

Figure 4-3 Comparison of calculated and predicted half values layers for the Statscan beam.

the generated TASMIP spectra by various thicknesses of Aluminium and generating a table of exposures using the inverse of Equation 4-2. Interpolation was then used to find the predicted HVL. Figure 4-3 shows the fairly good agreement between calculated and measured HVL's.

4.1.2 Geometric blur

There is a blurring effect due to the finite focal spot size and the machine geometry. This blurring effect is dependant on the focal spot intensity distribution, the collimator gap width and the geometry parameters SO, SD and SC (see Figure 1-1).

In the slit direction, the geometrical blur due to finite focal spot size causes every point in the object plane to be imaged in the detector plane as a demagnified version of the focal spot. The scan direction blur is a result of beam divergence and the TDI effect and is highly dependant on the object to detector distance and the focal spot width.

In order to calculate the LSF's and MTF's due to geometrical blur, it is necessary to know the focal spot intensity distribution. Figure 4-4 and Figure 4-5 show the intensity distribution in the scan and slit direction for the large and small focal spots respectively. For the calculation of geometrical blur, it is assumed that the focal spot is a horizontal plane that emits x-ray photons isotropicaly.

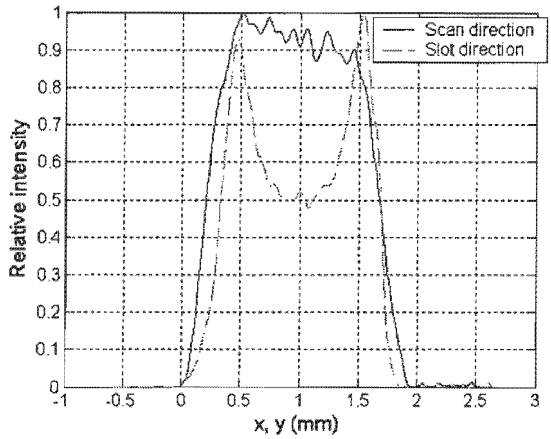

Figure 4-4: Large focal spot intensity distribution averaged in the slit and scan directions from measurements for the Statscan system (see Appendix A and [70]).

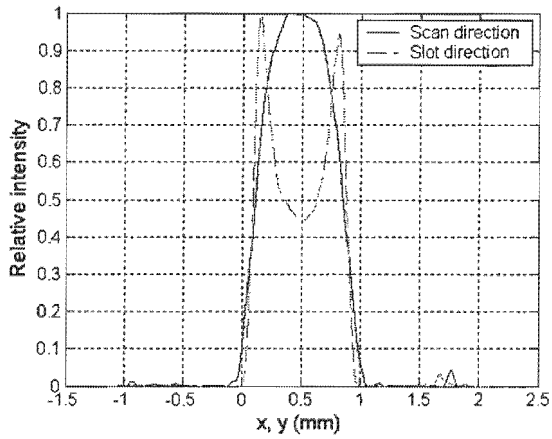

Figure 4-5: Small focal spot intensity distribution averaged in the slit and scan directions from measurements for the Statscan system (see Appendix A and [70]).

4.1.2.1 Blurring in the slit direction due to finite focal spot size

The double sided LSF in the detector plane due to focal spot blurring effects in the slit direction is given by (see Figure 4-6):

$$geom(x) = focal\left(\frac{x + F_w/2}{M_f}\right), \tag{4-4}$$

where $focal(\tau_x)$ is the intensity distribution in the slit direction of the focal spot in the focal spot plane. $M_f = \frac{OD}{SD - OD}$ is the demagnification of the projected image of the focal spot in the slit direction due to the system geometry and is included in order to refer the LSF to the detector plane. In other words *geom(x)* is the response of the system to an infinitely thin slit in the *y* (scan) direction and is a scaled version of the focal spot intensity distribution in the *x* (slit) direction.

The MTF due to focal spot blurring in the slit direction is given by the Fourier transform of the double sided LSF *geom(x)*:

$$T_1(f_x) = \Im\{geom(x)\}. \tag{4-5}$$

Figure 4-7 and Figure 4-8 show the geometric blur MTF in the slit direction for various object to detector distances and for the two available focal spot sizes.

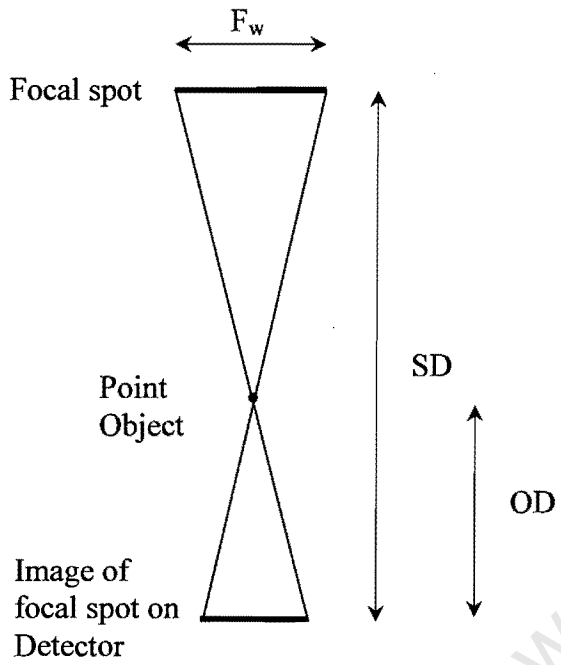

Figure 4-6 Illustration of focal spot blurring in the slit direction. The PSF in the detector plane is a demagnified version of the focal spot. The MTF is the normalised magnitude of the Fourier transform of the PSF.

4.1.2.2 Blurring in the scan direction due to beam divergence

The geometrical blur in the scan direction is a result of beam divergence, finite focal spot size and the TDI effect. As the beam is scanned over a point, not all rays pass through the point and reach the CCD in the same direction. Rays that pass through a point in the object at an oblique angle cause image data to be registered a distance away from directly below the point in the object. The cumulative effect of this false image data is the PSF of geometrical blur in the scan direction. This blur is dependant on the collimator gap width, the focal spot intensity distribution, the object to detector distance and the source to collimator distance. The scan direction blur is independent of the source to detector distance.

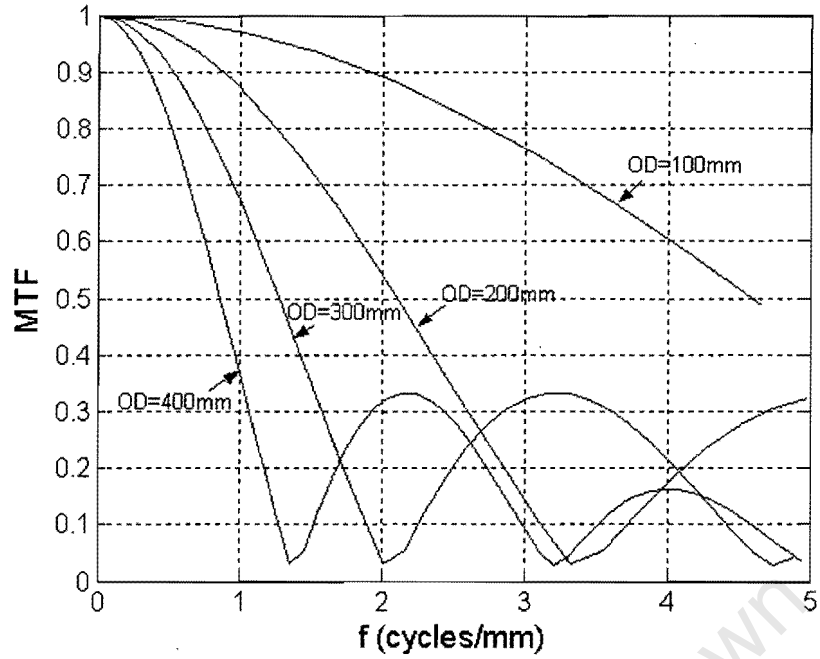

Figure 4-7 (Large Spot) MTF in the slit direction due to large focal spot blurring. The MTF is referred to the detector plane and is calculated for OD's of 100mm, 200mm, 300mm, 400mm.

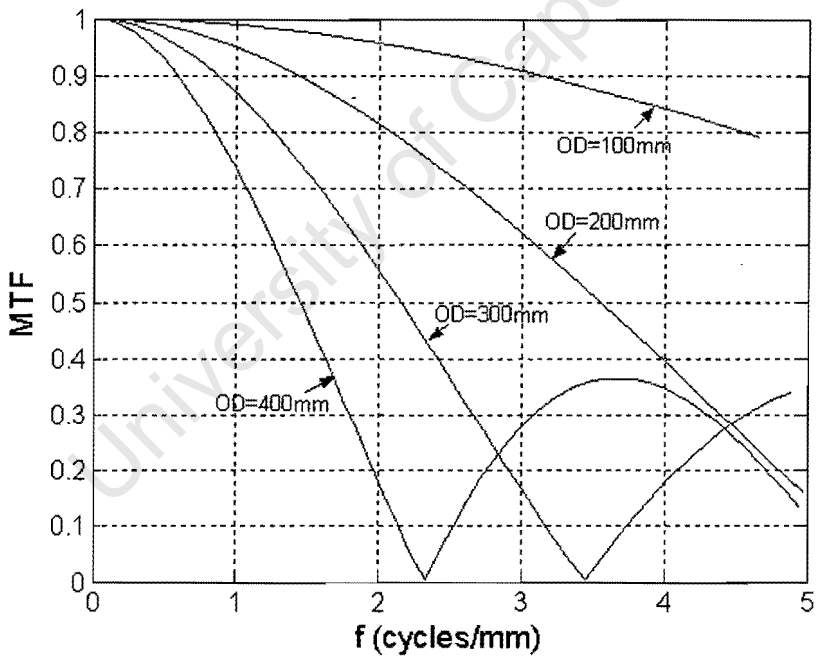

Figure 4-8 (Small Spot) MTF plane in the slit direction due to small focal spot blurring. The MTF is referred to the detector plane and is calculated for OD's of 100mm, 200mm, 300mm, 400mm.

Figure 4-9 and Figure 4-10 illustrate the blurring effect of beam divergence in the scan direction. It is necessary to integrate the effect of the angled rays on the PSF over the focal spot intensity distribution with the limits of integration being dependant on whether the focal spot is wider than

the collimator gap width or not. The single sided LSF in the detector plane due to the beam divergence in the scan direction is given by:

$$geom(y) = \int_{F_1(y)}^{F_2(y)} focal(\tau_y) d\tau_y \,, \tag{4-6}$$

where the limits of the integration are given by:

$$F_1(y) = \begin{cases} \dfrac{F_w - C_w}{2} - \dfrac{SCy}{OD} & \text{for } \left(\dfrac{F_w - C_w}{2} - \dfrac{SCy}{OD}\right) \geq 0 \text{ and } F_w \geq C_w \\ 0 & \text{otherwise} \end{cases} \tag{4-7}$$

and

$$F_2(y) = \begin{cases} \dfrac{F_w + C_w}{2} - \dfrac{SCy}{OD} & \text{for } 0 \leq \left(\dfrac{F_w + C_w}{2} - \dfrac{SCy}{OD}\right) \leq F_w \\ 0 & \text{otherwise} \end{cases} \tag{4-8}$$

and $focal(\tau_y)$ is the focal spot intensity distribution in the focal spot plane (in the scan direction). F_w and C_w are the focal spot widths and collimator gap widths respectively. SC and OD are the source to collimator distance and object to detector distances respectively.

The maximum x value for which $geom(y)$ is non-zero is given by $y_{\max} = \dfrac{OD}{SC}\left(\dfrac{F_w + C_w}{2}\right)$ which is the width of the single sided LSF due to the beam divergence in the scan direction. It can be seen that the lower limit of the integration, $F_1(y)$, is different for the case of the focal spot being wider than the collimator gap width ($F_w \geq C_w$) and for the case of the focal spot being narrower than the gap width ($F_w \leq C_w$).

The geometrical MTF due to the beam divergence in the scan direction is given by the Fourier transform of the double sided LSF:

$$T(f_y) = \Im\{geom(y) + geom(-y)\} \tag{4-9}$$

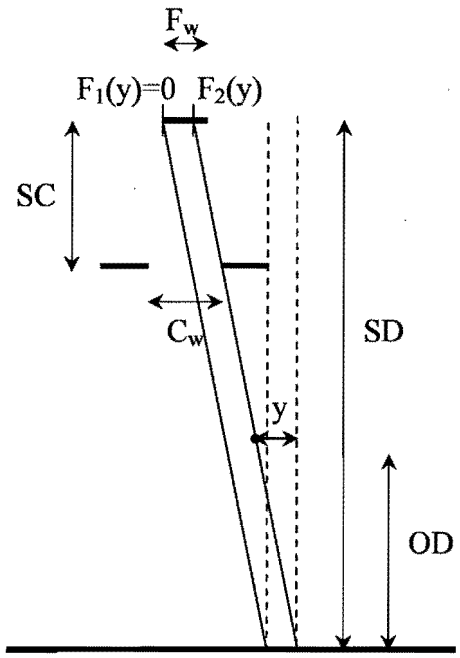

Figure 4-9 Illustration of geometric blur in the scan direction for the case with the focal spot narrower than the collimator gap width.

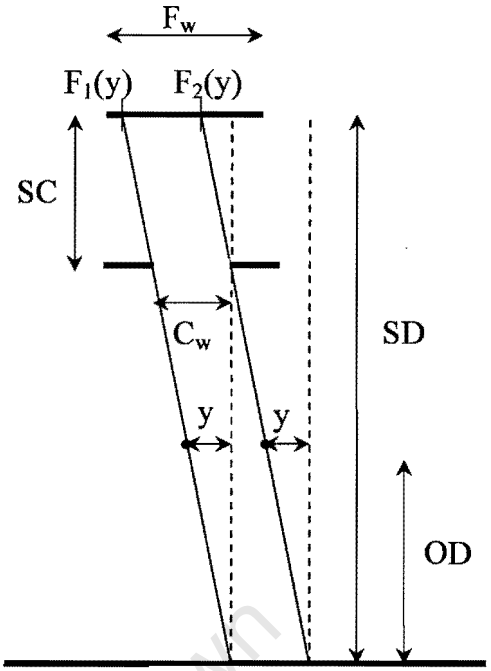

Figure 4-10 Illustration of geometric blur in the scan direction for the case with the focal spot wider than the collimator gap width.

It should be noted that $T(f_y)$ is the MTF due to the beam divergence in the scan direction referred to the detector plane. Also, $T(f_y)$ is independent of the source to detector distance but is dependant on the object to detector distance (OD) and source to collimator distance (SC). OD varies within the object so that points closer to the detector in the object are less blurred than points further away. For the calculation of $T(f_y)$ in the results section, a point in the middle of an average thickness patient was used. For a detector to table top distance of 70 mm and an example average patient thickness of 200 mm, this gives an OD of +-170 mm. Figure 4-11 and Figure 4-12 show the scan direction geometric blur calculated for various collimator gap widths, object to detector distances and for the two available focal spot sizes.

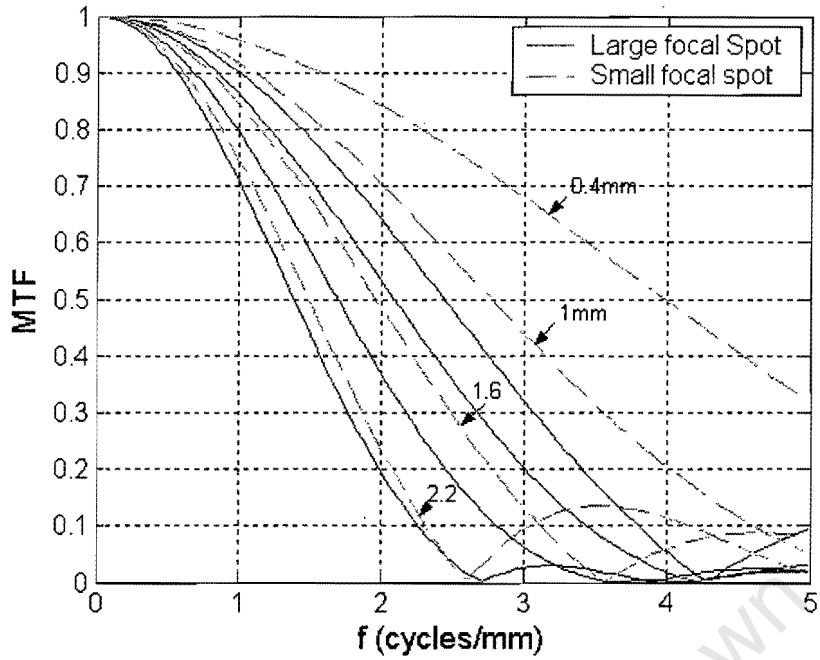

Figure 4-11 MTF due to beam divergence in the scan direction. The MTF's are calculated for collimator widths of 0.4mm, 0.8mm, 1.2mm and 2 mm and for large and small focal spot sizes. The source to collimator distance was set to SC=400mm and the object to detector distance was set to OD=70mm.

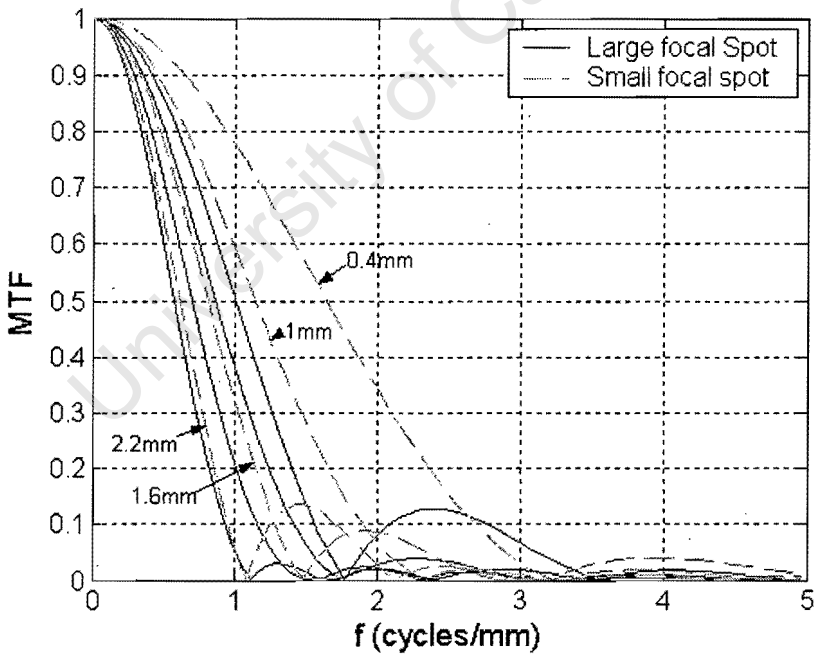

Figure 4-12 MTF due to beam divergence in the scan direction. The machine settings are the same as those in Figure 4-11 except for the object to detector distance that is changed to OD = 170mm.

4.1.3 Grid attenuation

Data for the primary and scatter transmission of typical grids has been included in the model to allow comparison of the gridless system under study with systems that use grids. Grid attenuation of primary radiation can be treated as a binary selection stage with gain given by the primary transmission of the grid t_p (equivalent to g_2 in the model). As shown in Section 3.2.3, the System DQE is effectively multiplied by the primary grid transmission. Data for grid transmission of scattered radiation t_s is included to facilitate comparison of the SPR of the system under study with that of other systems. Values for t_p in the literature typically fall in the range 0.45 – 0.65 depending on the grid type and values for t_s typically fall in the range 0.05 – 0.15 [28, 29, 53, 71].

4.1.4 Scattered radiation incident

Data for the scatter to primary ratio (SPR) incident on the detector was calculated using a GEANT4 [72, 73] Monte Carlo simulation (see Appendix C for brief illustration) on a twenty node Linux computing cluster. The SPR is highly dependant on the thickness and density of the scattering object, the air gap and on the field size. In order to limit the complexity of the simulations, it was decided to use only two thicknesses of water as the scattering object (20 cm and 40 cm). The 20 cm thickness is intended to approximate the abdomen in a frontal scan, whiles the 40 cm thickness approximates the lateral case in a large patient or the frontal case in a bariatric patient. To further simplify, it was assumed that the SPR is independent of the peak tube voltage setting [47, 74]. The author believes the assumption that SPR is independent of kV is reasonable for the purposes of this study. In reference [47] a SPR is measured by the beam stop method to be invariable as a function of kV between 80 and 120 kVp. In reference [74] the SPR varies by no more than 10% between 50 and 110 keV. The sensitivity of the model to small changes (< 10%) in the SPR is low and this has been checked in MATLAB.

Four simulations for each water thickness were carried out with different collimator gap widths (and hence beam widths) and a fixed beam length of 400 mm. The results for the SPR as a function of collimator slit width and a linear fit through the data points are shown in Figure 4-13. The data is highly linear in this beam width range. In order to compare the results with published data, it is convenient to convert the collimator width to an effective beam width at the detector.

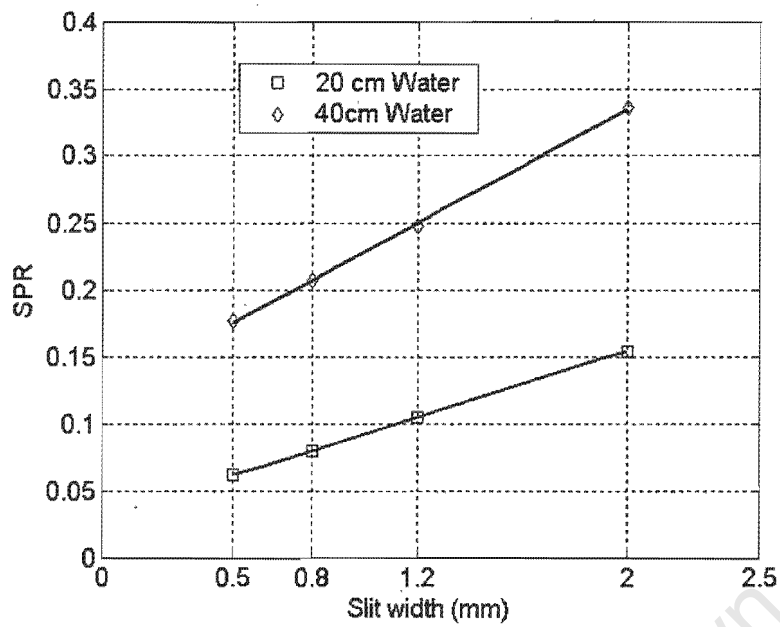

Figure 4-13 Monte Carlo simulated scatter to primary ratios for various slit widths and a straight line fit. The collimator slit widths of 0.5, 0.8, 1.2 and 2 mm correspond to beam widths at the detector of 3, 4, 4.9 and 7.85 mm respectively.

For the geometry used in the Monte Carlo simulation, the conversion from collimator width to beam width at the detector is given by:

$$B_w = \frac{SD(F_w + C_w)}{SC} - F_w \,, \tag{4-10}$$

where B_w is the beam width at the detector, F_w is the focal spot width, C_w is the collimator slit width and SC and SD are the source to collimator and source to detector distances respectively. Values used in the Monte Carlo simulations were: SC = 400 mm, SD = 1300 mm and F_w = 0.8 mm.

The main idea of Figure 4-13 is to show the relationship between slit width and the SPR in the system under study – something that is important in the trade off between collimator flux transmission and SPR in a slit scanning system. For the purpose of comparison with other imaging systems the following data was found.

- Barnes et al. [53] report a SPR of about 7.7 for a full field geometry machine and a 20 cm deep Acrylic phantom with no grid.

- Chan and Doi [75] report a SPR of approximately 3 for a 10cm beam width and a 20 cm deep water phantom with no grid. Their results were obtained by Monte Carlo simulation.

- Samei et al. [7] report a measured SPR of 0.13 in the lung region and 0.35 in the sub-diaphragm region for the ThoraScan slit scanning chest radiography machine.

- Barnes et al. [5] report a measured SPR of 0.4 in the lung region and 1.3 in the sub-diaphragm region for a full field system *with* a grid. They also report a SPR of 0.125 for a 10 mm wide beam width and 20 cm deep Acrylic phantom with no grid.

The Monte Carlo results show good agreement with published data for similar beam widths, phantoms and geometry [5, 7, 53]. Since the collimator slit width in the Statscan system is typically set to 0.4 mm it is clear that particularly low SPR's are obtained in comparison to values listed in point form above. The author realises that these are fairly old values (~1980) applicable to older grids and the author has not investigated newer SPR values for conventional systems. This can be done if anybody chooses to use the model in the future.

4.1.5 X-ray quantum absorption efficiency in the screen

X-ray photons incident on the screen can interact by a Compton Scatter, a Rayleigh scatter or by the Photoelectric effect. Energy is not deposited in a Rayleigh scatter so only the Compton and Photoelectric effects are taken as quantum absorptions. The probability of quantum absorption for monoenergetic x-rays of energy E is given by the Lambert-Beers law:

$$g_4(E) = 1 - e^{-\left(\frac{u_P(E)}{p} + \frac{u_C(E)}{p}\right)pt}, \qquad (4\text{-}11)$$

where p is the density of the screen material and t is the screen thickness. u_p/p is the mass attenuation coefficient for the Photoelectric effect in the screen material and u_c/p is the mass attenuation coefficient for Compton scatter. The term pt is equivalent to the mass-thickness of the material δ with units of g/cm^2. The mass thickness and other parameters for the screens used in this study are summarized in Table 4-2.

Table 4-2: Parameters for screens used in this study

Parameter	Rarex Medium	Rarex Fast Back	DRZ-Plus	DRZ-High	PI-200
H	0.5	1.25	0.6	1.7	2.4
Reflective backing	Yes	Yes	Yes	Yes	Yes
Mass thickness (mg/cm^2)	50	130	100	145	200
Phosphor	Gd_2O_2S:Tb	Gd_2O_2S:Tb	Gd_2O_2S:Tb	Gd_2O_2S:Tb	Gd_2O_2S:Tb

For a poly-energetic spectrum incident on the screen, the mean quantum absorption efficiency (QAE) is calculated as:

$$\bar{\bar{g}}_4 = \frac{\int_{E=0}^{E=E_{max}} q_o(E)(1-e^{-(\frac{u_P(E)}{p}+\frac{u_C(E)}{p})pt})dE}{\int_{E=0}^{E=E_{max}} q_o(E)dE}, \quad (4\text{-}12)$$

where $q_o(E)$ is the energy spectrum of the primary flux incident on the detector.

The QAE for each beam quality and screen thickness used in this study (see Table 4-2) was calculated for the four IEC 62220-1 [11] recommended beam qualities. The results are shown in Figure 4-14.

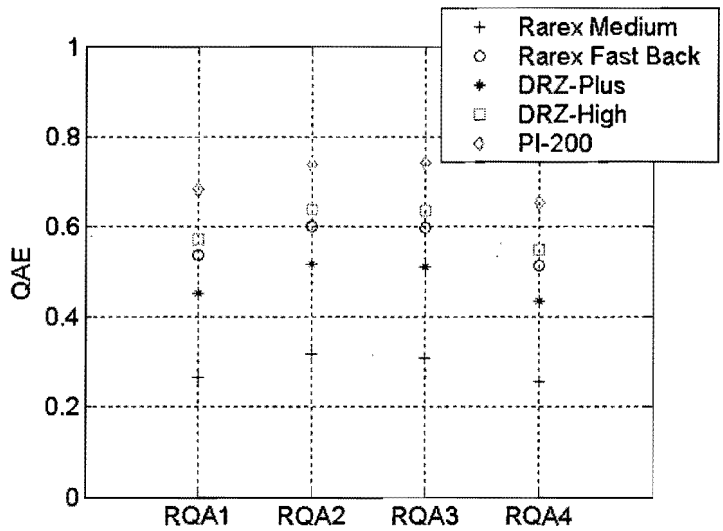

Figure 4-14 Quantum absorption efficiency for screens used in this study at IEC 62220-01 recommended beam qualities.

4.1.6 Conversion to optical quanta in the screen

Once an x-ray quantum is absorbed, its energy is amongst other things converted to several visible light photons. The number of light photons released per absorbed x-ray photon at the image side of the screen is the conversion gain of the phosphor. Various effects cause random fluctuations in this gain such as K-fluorescence escape and re-absorption, light photon scattering and the variable incident x-ray energy. Thicker screens may have reduced K-escape, but increased self attenuation – competing effects that impact on the number of light photons emitted.

Due to the complexity of these processes, modelling the generation and escape of photons in a screen appears to be more difficult than actually measuring the conversion gain and variance [77, 79].

Ginzburg and Dick [79] have measured the energy dependant conversion gain for several different types of Lanex Gd_2O_2S:Tb screens (Lanex Fast Back, Fast Front, Medium, Regular and Fine). The manufacturer of the Rarex Gd_2O_2S:Tb screens used in the system under study were unable to provide conversion gain and variance data but claim that their Rarex Fast Back, Medium screens are similar to their Lanex counterparts. For the purposes of this study, the conversion gains measured by Ginzburg and Dick for the Lanex screen equivalents are used.

The energy dependant mean conversion gains for x-ray photons absorbed in Rarex Fast Back and Medium screens are shown in Figure 4-15.

For a poly-energetic incident x-ray flux, the mean conversion gain is the weighted average of the conversions gains calculated over the energies of the absorbed energy spectrum.

$$\bar{g}_5 = \frac{\int_{E=0}^{E=E_{max}} C(E)q_o(E)dE}{\int_{E=0}^{E=E_{max}} q_o(E)dE} \tag{4-13}$$

where C(E) is the mean number of light photons emitted per absorbed x-ray photon of energy E. The mean conversion gains for Rarex Fast Back and Medium at various tube voltage settings were calculated using Equation 4-13 and are shown in Figure 4-16. For the three other screens used in this study (Figure 4-16) manufacturer data giving light output relative to the Lanex Fast Back screen was used to estimate the conversion gain. It should be noted that the spectrum existing the tube was filtered by patient equivalent thicknesses of Aluminium (see Table 4-1) before the mean conversion gain was calculated.

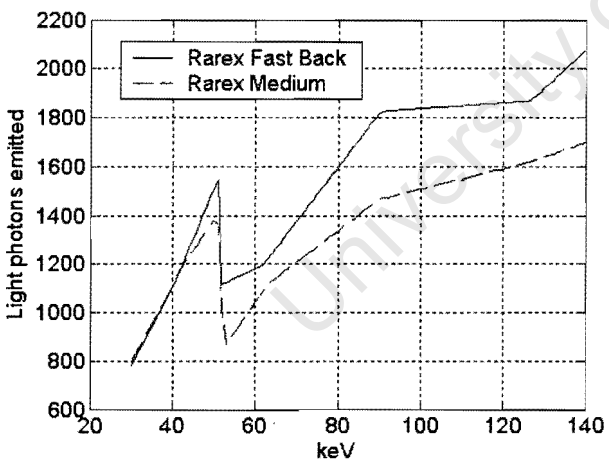

Figure 4-15: The energy dependent mean conversion gain of the Lanex/Rarex Fast Back and Medium screens. The sharp drop in conversion efficiency at 50.2 keV is due at the K-edge of the Gadolinium present in the screens. Taken from measurements by GinzBurg and Dick [79].

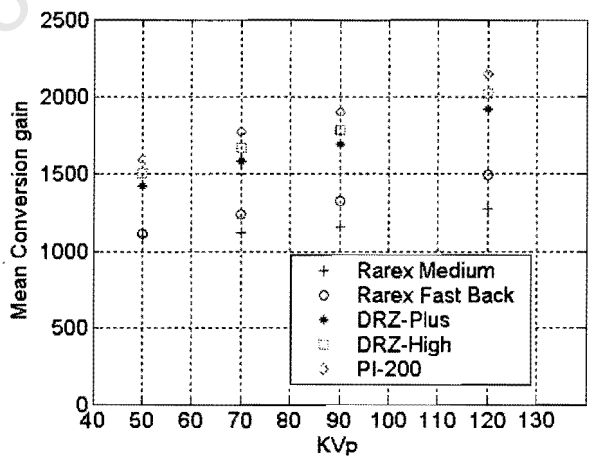

Figure 4-16: Peak voltage setting dependant mean conversion gains for the screens used in this study. Note that gains for DRZ-Plus, DRZ-High and PI-200 are only rough estimates based on limited data. The spectrum used for calculation of the gains was been filtered by the thicknesses of Aluminium defined in Table 4-1.

The random fluctuations in the conversion gain are usually described in terms of the Swank factor [77, 79]. For mono-energetic x-rays, the Swank factor is defined as:

$$A_S(E) = \frac{M_1^2}{M_0 M_2} \tag{4-14}$$

where M_n is the nth moment of the light output distribution for monoenergetic x-ray photons absorbed in the screen. The light output distribution that the moments described above are derived from is normally measured using a Pulse height Spectrometer (PHS) [79].

For a monoenergetic absorbed x-ray of energy E the first three moments of the light output distribution can be defined as follows [37], [39]:

$$M_0 = 1, \tag{4-15}$$

$$M_1 = C(E) \tag{4-16}$$

$$M_2 = C(E)^2 + C(E)(1+\varepsilon) \tag{4-17}$$

where ε is the Poisson excess of the gain distribution (see section 2.3.1 for definition of Poisson excess). For Gd_2O_2S:Tb, $A_S(E)$ is essentially unity for energies less than the K-edge at 50.2 keV. For a polychromatic x-ray spectrum, A_S is calculated by averaging the moments over the energy spectrum of x-rays absorbed in the screen [41, 77] and combining the results using Equation 4-14. In this manner, fluctuations due to variable x-ray energy and absorption are also taken into account. The Poisson excess for the light output distribution (or equivalently for the conversion gain of Stage #5) for a polychromatic input spectrum can then be calculated as:

$$\varepsilon_5 = \frac{\bar{g}_5}{A_S} - \bar{g}_5 - 1 \approx \frac{\bar{g}_5}{A_S} - \bar{g}_5 \tag{4-18}$$

This result can be used in a stochastic Gain Stage as described in section 2.3.1.

As pointed out by Williams et al. [38] limited available Swank factor data for Gd_2O_2S:Tb screens of arbitrary thickness and for an arbitrary incident x-ray spectrum makes the Swank factor a difficult parameter to generalize. Therefore it was decided for the purposes of this study not to

Table 4-3: Estimate of Swank factor for each screen type and beam quality.

Screen type, thickness	Beam Quality	A_S estimate	ε_5 estimate	Source of estimate
Rarex Fast Back, 130 mg/cm2,	RQA3	0.85	194	[77], 78, [79],[80]
"	RQA5	0.75	417	[77],[79],[80]
"	RQA7	0.72	510	[40]
"	RQA9	0.7	625	[27]
Rarex Medium, 50 mg/cm2	RQA 3	0.73	420	[40]
DRZ-Plus, 100 mg/cm2	RQA 5	0.75	566	[77], 78[79], 80]
DRZ High, 145 mg/cm2	RQA 7	0.72	690	[77],[79],[80]
PI-200, 200 mg/cm^2	RQA 9	0.7	790	[77], [78], [79], [80]

attempt to generalize the Swank factor for arbitrary phosphor mass-thickness and incident x-ray spectrum but rather to make estimates based on previously published values for specific cases [27, 40, 78], and knowledge of the trends evident in the Swank factor over the diagnostic energy spectrum [77, 78, 79, 80]. The author realizes that this limits the degree that one can be confident of the accuracy of the values of ε_5 used in the model (see Table 4-3).

4.1.7 Stochastic redistribution of quanta in the screen

The MTF due to stochastic redistribution of quanta in the screen is affected by many factors such as the K-fluorescence escape and reabsorption, depth dependant blurring and light propagation and reflection.

Swank [81] provides the following simple model for the MTF of a transparent phosphor with reflective backing (referred to as Type A in the text):

$$T(f) = \frac{\tanh(2\pi f d)}{2\pi f d} \tag{4-19}$$

Where d is the thickness of the phosphor in *mm*. Swank's model is based on light diffusion modeling and the assumption of exponential depth x-ray absorption. K-fluorescence reabsorption effects are ignored. The model has the advantage that it allows one to specify an arbitrary phosphor thickness. Swank's model was however not used because of unexplained and large discrepancies with MTF data supplied for the screens used in this study.

It was instead decided to follow the practice of other investigators [33, 40] and apply a Lorentzian fit to manufacturer supplied MTF data for the screens:

$$T_6(f) = \frac{1}{1 + H \cdot (f^2)} \tag{4-20}$$

The manufacturers (MCIO) of Rarex screens were unable to provide MTF measurements for their Rarex Fast Back and Medium screens. However they were able to say that these screens are similar in resolution properties to the Lanex Fast Back and Medium screens from Kodak. The parameter H for the Rarex screens was therefore calculated from data for their Lanex counterparts [40]. For the DRZ and PI screens the manufacturer (Kasei Optonix) supplied MTF data was used to calculate the fitting parameter H [82]. The fitting parameters used for the screens in this study are summarized in Table 4-2 and the calculated MTF for each screen is shown in Figure 4-17.

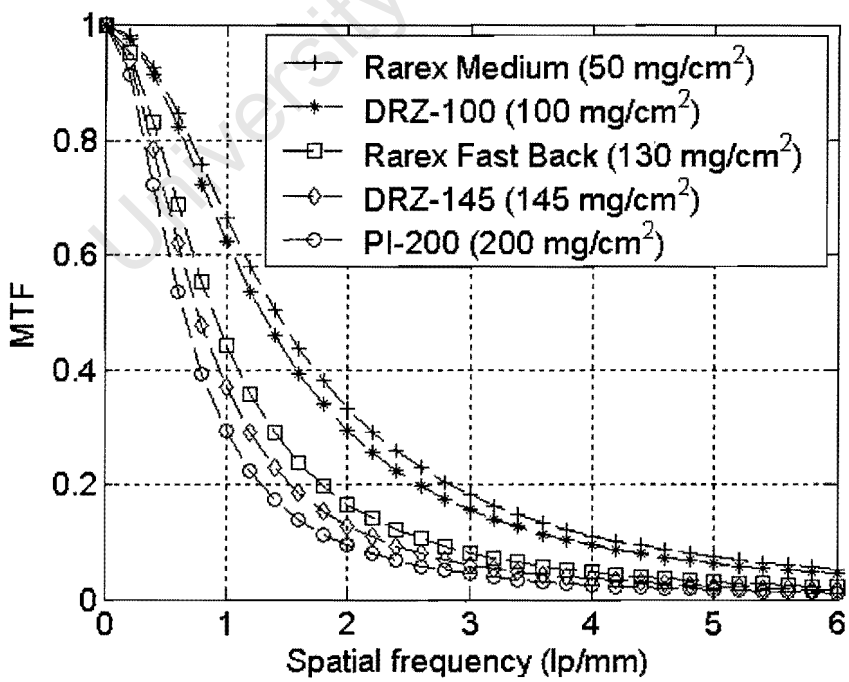

Figure 4-17 Lorenzian fit to manufacturer supplied MTF data for the screens used in this study.

4.1.8 Blurring due to finite phosphor persistence

Phosphor persistence has two concurrent components: an exponential decay of light intensity after initial stimulation and a longer lasting but lower amplitude "afterglow" [83], [84]. In this study the effects of afterglow are ignored as they are difficult to find data for and it is assumed that the afterglow intensity is low enough to make the effect negligible. For example Krus [85] states that the afterglow signal for Gd_2O_2S:Tb is less than 0.1 % of the initial stimulation output signal after 3 msec (although this result may be affected by the intensity of initial stimulation).

A simple model for the exponential time decay of light intensity in phosphor luminescence is given by Mainprize et al. [83]:

$$I(t) = I_o e^{-\frac{t}{\tau}}, \tag{4-21}$$

where $I(t)$ is the luminescence intensity at time t, Io is the initial intensity and τ is the "luminescence lifetime" or decay time constant. The "luminescence lifetime" is dependant on the type of phosphor and activator and on the concentration of phosphor dopants.

The MTF in the scan direction due to the exponential decay component is given by [83]:

$$T_\tau(f_x) = \frac{1}{\sqrt{1+(2\pi\upsilon\tau f_x)}}, \tag{4-22}$$

where υ is the velocity in the scan direction.

For the purposes of this study, a decay time constant of $\tau = 850$ µs for Gd_2O_2S:Tb is assumed [83]. The resultant MTF's for the three possible scan speed settings for the system under study (140, 70, 35 mm/s) and a hypothetical double speed setting (300 mm/s) are shown in Figure 4-18.

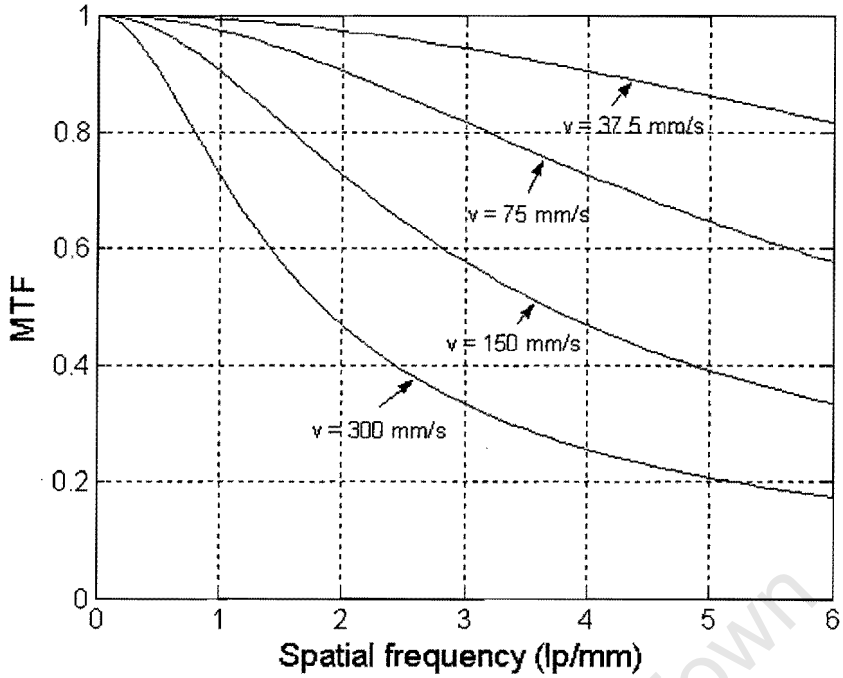

Figure 4-18: The MTF in the scan direction due to finite phosphor persistence. The curves with v = 150, 75, 37.5 mm/s correspond to Full, Half and Quarter scan speeds respectively. The MTF's are calculated for a Gd_2O_2S:Tb type screen with exponential decay time constant set to $\tau = 850$ µs.

4.1.9 Coupling of optical quanta to the CCD

Light photons that escape the screen are coupled to the CCD via the fibre optic taper (FOT) and a fibre optic plate (FOP). There is light loss in transmission through the taper, at the FOT to FOP coupling, in transmission through the FOP and at the point where light is absorbed in the CCD silicon.

The transmission efficiency of a fibre optic taper (FOT) for light from a Lambertian source pressed against the taper can be expressed as follows [86]:

$$T_T = \left(\frac{1}{m}\right)^2 \left(\frac{\left(n_2^2 - n_3^2\right)^{\frac{1}{2}}}{n_1}\right)^2 T_F\left((1 - L_R)F_C\right), \tag{4-23}$$

where T_T is the taper transmission, m is the demagnification of the fibre core, n_1, n_2 and n_3 are the refractive indices of the source medium, the fibre core and the cladding respectively. T_F is the

transmission of the fibre core, L_R is the loss at the FOT surface and F_C is the fill factor of the fibre core.

For the untapered fibre optic that is drawn to create the FOT, the transmission efficiency for a Lambertian source is given by [86]:

$$n_{FO} = NA^2 T_F \left((1 - L_R) F_C\right), \tag{4-24}$$

where NA is the numerical aperture of the fibre core.

Using the values in Table 4-4 and Equation 4-24, the value of $T_F\left((1 - L_R\right)$ was calculated and substituted into equation 4-23 to give the FOT transmission efficiency T_T. Figure 4-19 shows the calculated values for T_T at various demagnifications. Some of the data in the table was supplied by Incom the FOT manufacturer.

Table 4-4: FOT parameters used in the transmission efficiency calculation

Parameter	Value	Description	Data Source
F_C	75:25	FOT Fill factor	Incom
NA	1	FOT Numerical aperture	Incom
n_{FO}	0.61	Transmission of untapered FOT	Incom
M	2.3	FOT Demagnification	Incom
N_1	1	FOT Refractive index source medium	estimated [32]
N_2	1.8	FOT Refractive index core	Incom
N_3	1.49	FOT Refractive index cladding	Incom

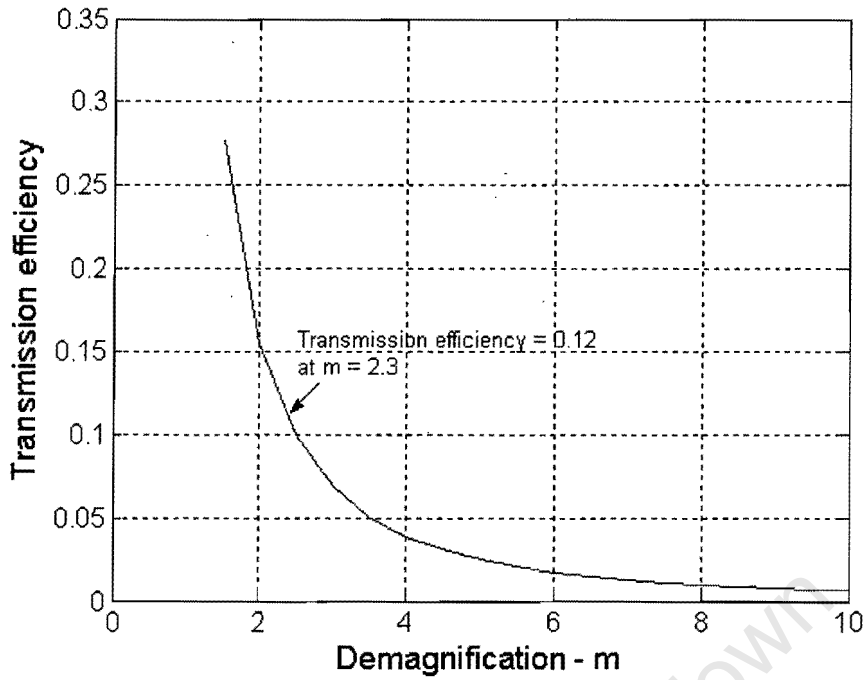

Figure 4-19: FOT transmission efficiency as a function of demagnification.

The FOT to FOP coupling efficiency and FOP transmission efficiency were estimated to be 0.5 and 0.6 respectively [14] .

The conversion efficiency of light photons to electron-hole pairs in the CCD depends on the wavelength distribution of the light incident on the CCD $I(\lambda)$ and the wavelength dependant quantum efficiency of the CCD $Q_{CCD}(\lambda)$. The average number of electrons produced per light photon incident on the CCD silicon is given by:

$$\overline{Q}_{CCD} = \frac{\int_{\lambda=0}^{\lambda=\infty} Q_{CCD}(\lambda) I(\lambda)}{\int_{\lambda=0}^{\lambda=\infty} I(\lambda)} \tag{4-25}$$

where $Q_{CCD}(\lambda)$ is the wavelength dependant absorption efficiency of the CCD silicon and $I(\lambda)$ is the incident light spectrum (see Figure 4-20). The coupling efficiency for the E2V CCD used in this study and the Gd_2O_2S:Tb screens used was calculated to be 0.29. Combining the component coupling efficiencies described in this section gives an overall coupling efficiency of:

$$\bar{g}_8 = \overline{Q}_{CCD} T_T \times 0.5 \times 0.6 \approx 0.01 \tag{4-26}$$

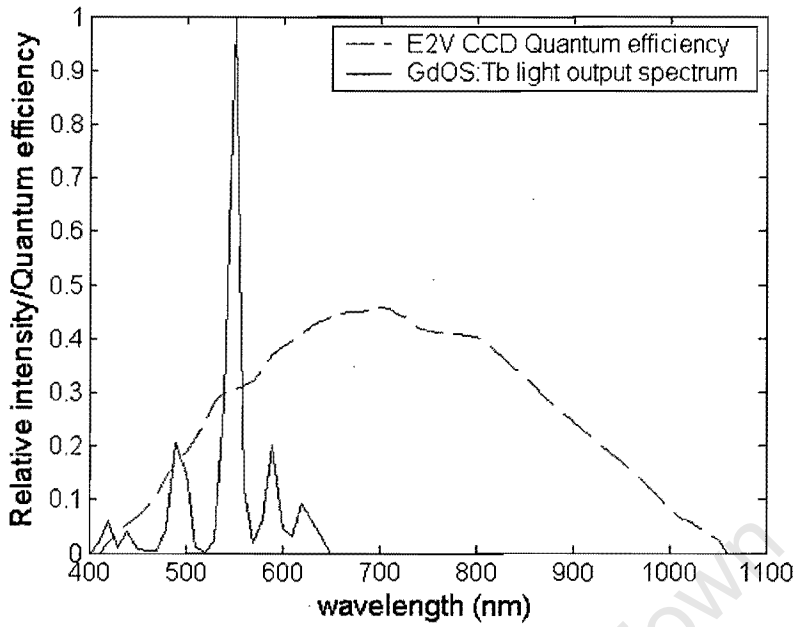

Figure 4-20 The spectral matching of a Gd_2O_2S:Tb screen to the CCD quantum efficiency. About 0.28 electrons are on average produced per incident light photon. Values were taken from the E2V CCD data sheet and from Kandarakis.

4.1.10 Integration of quanta in CCD pixel aperture

The deterministic blur pixel aperture function due to integration of quanta in the CCD pixel elements is a *rect* function of width *a*. The pixel aperture MTF is the Fourier transform of the pixel aperture function referred to the detector plane. The transformation of pixel size from the CCD plane to the detector plane is simply a multiplication by *m* (the FOT magnification). For *bxb* binning, the apparent pixel size is again increased by the factor *b*. The MTF due to the CCD aperture function in the detector plane is therefore given by:

$$T_9(f) = \Im\left\{rect(\frac{x}{ma})\right\} = \text{sinc}(bma \times f) \tag{4-27}$$

where *a* is the pixel width.

4.1.11 CCD and electronic additive noise

At the final stage in the image forming process, noise is added in the CCD and external circuit from several sources [86]. Figure 4-25 summarizes conceptually the various noise sources that contribute to the total additive noise (see Table 4-5 for key).

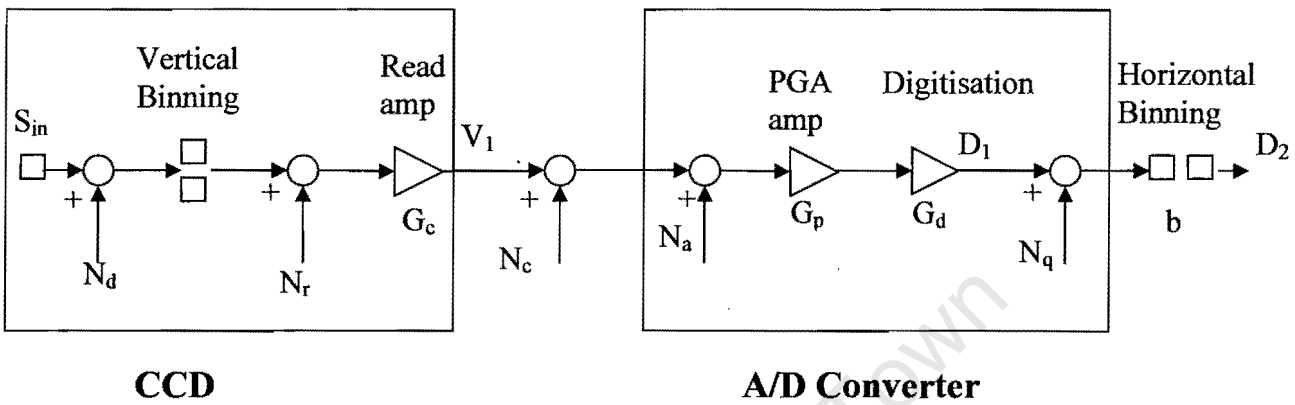

Figure 4-25 Illustration of signal and additive noise propagation through the CCD and external electronic circuit.

Starting from the left of Figure 4-25: the TDI integrated signal (and associated noise) S_{in} (with units of electrons) is accumulated and clocked into the line register. The dark noise N_d that has accumulated during integration is added at this stage. The signal and noise is then binned vertically in hardware by clocking b times into the line register (for *bxb* binning). The dark noise is therefore blurred by the pixel aperture along with the signal. The signal is then amplified and converted to the voltage signal V_1 by the CCD output amplifier and the amplifier read noise N_r is added. The read noise appears before the amplifier as it is quoted in electrons referred to the CCD amplifier input. External circuit noise such as clocking noise and electromagnetic interference is then added. The A/D converter has a PGA amplifier for setting the dynamic range which adds noise N_a. Digitisation then takes place with gain G_d and quantization noise N_q with variance 1/12 is added as a consequence. Horizontal binning, which is simply the process of adding *b* (in *bxb* binning) neighbouring pixel values in software, takes place next. All the noise sources are assumed to be uncorrelated so the noise sources are simply multiplied by a factor *b* in the horizontal binning process.

Table 4-5: Key and values of symbols in Figure 4-25. Values for the various noise sources are expressed as a pixel variance referred to the CCD input in units of electrons.

Symbol	Definition and Units	Value	Method of calculation
S_{in}	Input signal to CCD.	-	-
N_d	Variance of dark noise in CCD (electrons).	109, 54.5, 27.25 for quarter, half and full speed respectively.	Typical value from E2V CCD30-11 data sheet. N_d = 250 e^-/pixel/s x Line clock period (in seconds) = 250 e^- /pixel/s x 256 x 0.06 mm / Scan speed (mm/s).
N_r	Variance of the read noise in CCD (electrons).	5	Typical value from E2V CCD30-11 data sheet.
G_c	CCD Output amplifier sensitivity (uV/electron).	2	Manufacturer supplied data (E2V). Equivalent to max. value on E2V CCD30-11 data sheet.
N_c	Variance of external circuit and clocking noise (uV).	5975	Calculated as difference between all other dark noise sources and total measured dark noise.
N_a	Variance of PGA and A/D noise and crosstalk (uV).	4225	From Analog Devices AD9814 data sheet.
G_p	PGA amplifier gain (uV/uV).	1	From Analog Devices AD9814 data sheet.
G_d	Digitisation gain (D/uV).	1/244	From Analog Devices AD9814 data sheet.
N_q	Variance of quantization noise (D).	1240	Calculated assuming uniform probability distribution function with variance 1/12 at the output. Variance referred to input by propagation through the square of the gains.

The dark noise was measured by taking a scan without x-ray flux incident on the detector. The same method described in Section 4.2.4 was used to calculate the NPS of the dark noise. The result was then passed through the squared inverse of the CCD and output circuit gains in order to refer the dark NPS to the CCD input. Figure 4-26 shows the result in the slit and scan direction for the dark NPS that was measured and added as the final stage in the Linear Cascaded Linear-Systems Model. Some low frequency artefacts are present – probably due to structural and spatial non-uniformities (these were not included in the model). Also, there appears to be blue noise (noise that increases with f) in the slit direction, the source of which is not yet clear.

The dark NPS was measured at 1x1 binning, but as mentioned in the second paragraph of this sub-section, the result can be modified for other binnings by simply multiplying by the binning number b. The pixel variance at the CCD input is found by normalizing the dark NPS by the pixel area used in the measurement (0.06 x 0.06 mm) giving a dark noise pixel variance of approximately 11500. This result was confirmed by calculating the output variance of a dark image and referring it to the CCD input by multiplying by the squared inverse gains in the CCD and output circuit. In order to get an overview of the approximate contribution of each noise source to the total, values for the individual contributions were calculated or taken from data sheets where possible (see Table 4-5). The variance of the remaining dark noise source (external circuit noise N_c) was then calculated by the process of elimination.

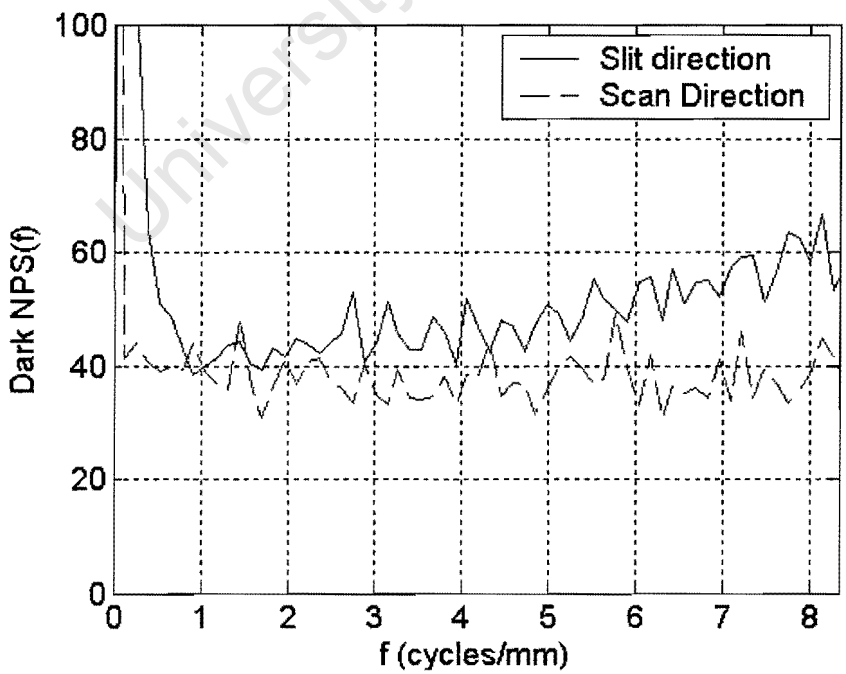

Figure 4-26 Measured Noise Power Spectrum of the dark noise (CCD and external circuit additive noise). The dark noise was measured at 1x1 binning giving a 60 um pixel size and a Nyquist frequency of 8.33 lp/mm.

4.2 Measurement of DQE, MTF, NNPS

In order to validate the model, several measurements of the detector MTF, NPS and DQE were made at various detector configurations, and exposure levels. The measurement method used is outlined in the IEC 62220-1 standard [11], is described in detail in the literature [21] and has been used in practice by other investigators [23]. A similar method was used to measure the DQE for an older version of the Statscan radiography machine [9]. The algorithm for calculating the DQE and intermediate results was implemented in C++. Corresponding theoretical values for the MTF, NNPS and DQE were calculated and compared to the measured values.

The method outlined in IEC 62220-1 does not apply directly to linear slit scanning systems, but a simple modification to the dose calculation method makes it applicable to this purpose [9]. In linear slit scanning, the exposure area increases proportional to the distance from the source rather than with the square of the distance as with conventional geometry systems [9]. Therefore, the dose correction for ionisation chamber to detector distance follows a 1/r law rather than a $1/r^2$ law. This fact is unique to *linear* slit scanning systems (the exposure area of radial slit scanning systems with a stationary tube increases by the square of the distance from the source).

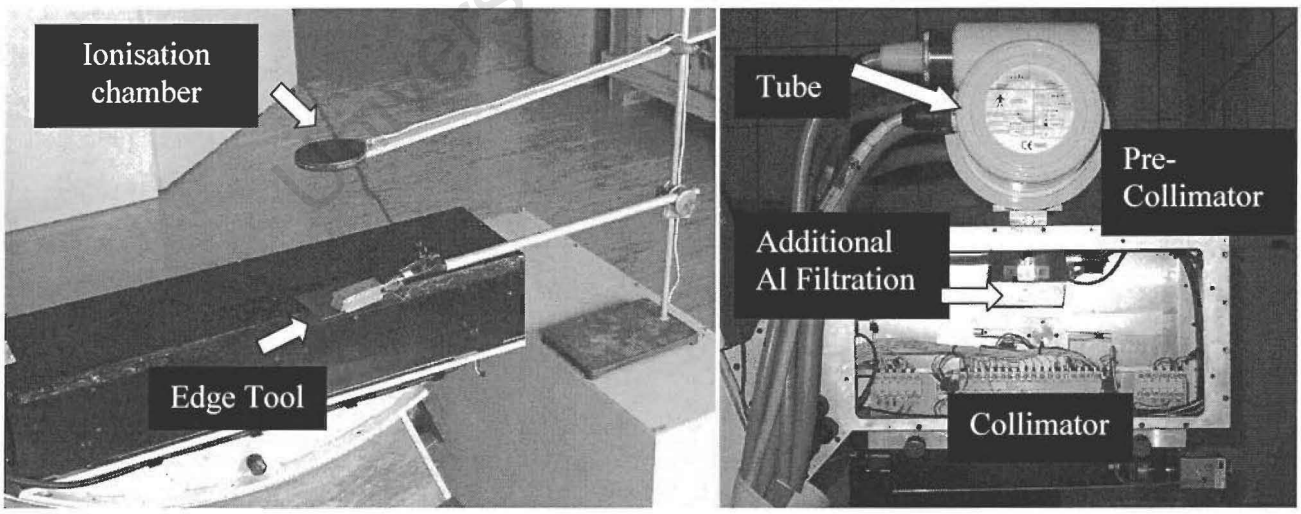

Figure 4-27. Acquisition conditions for dose, NNPS and MTF measurement. The IEC 62220-1 defined patient equivalent thickness of Aluminium was placed behind the main collimator in order to minimise detected scatter.

4.2.1 Acquisition conditions

Flat field images for the analysis of NPS and MTF were acquired at three exposure levels for each screen type and detector configuration (see Figure 4-27 for setup used). The additional thickness of Aluminium required for each beam quality defined in IEC 62220-1 was placed behind the collimator to minimize scatter. For the MTF measurement, a tungsten plate was placed in the beam (see Section 4.2.3). Log compensation was turned off so that the raw pixel values were proportional to the charge accumulated in the CCD line register during scans. Unbutting, gain correction and offset correction were turned on. The beam was collimated to expose only the four central cameras of the detector and the resulting images were about 2000 x 2000 pixels in size (for 2x2 binning).

4.2.2 Dose measurement

A relatively large (60 cm^3) ionisation chamber (Radcal 10X5-60E with Radcal 9010 dosimeter) was used to retain sensitivity at the low dose levels typical of the machine under study. The ionisation chamber was placed about 300 mm from the detector to minimize backscatter effects [68]. For each scan taken, the flux density $\bar{q}_0$ was calculated at the detector plane using the method described at the beginning of Section 4.2.

4.2.3 Detector Modulation Transfer Function

The MTF was measured using the angled edge method as described in Samei et al. [20] and de Villiers et al. [9]. Images of a milled rectangular tungsten plate with edges angled at about 2 degrees from the scan and slit direction were obtained. The edge position and angle was identified by using a Nelder-Mead optimisation algorithm. This method was used to find the edge angle and position that maximized the mean signal level difference on either side of the edge. An over-sampled (pre-sampled) edge spread function was then obtained by binning pixel values projected parallel to the edge onto an orthogonal line. The LSF was found by differentiating the ESF using a numerical difference method and the MTF was obtained by Fourier transforming the LSF.

The tungsten plate was placed as close possible to the detector – about 7 mm from the screen due to limitations imposed by the detector housing. The effect of the distance between plate and screen on the measured MTF is discussed in the results and discussions section. Care was taken to make sure the plate was level.

4.2.4 Noise Power Spectrum

Several partially overlapped 128x128 regions of interest (ROI's) from the central 1000x1000 area of each flat image were used for the calculation of the Noise Power Spectrum. The two dimensional NPS was calculated as the mean of the squared Fast Fourier Transform of each ROI's. The result was then normalised by the overall mean value of the ROI's to yield the two dimensional Normalised Noise Power Spectrum (NNPS). One dimensional cuts in each orthogonal axis direction were obtained by averaging the central 7 lines (excluding the axis). The frequency values were transformed to the central axis scale by applying $f_x = \sqrt{f_x^2 + f_y^2}$ in the scan direction and $f_y = \sqrt{f_y^2 + f_s^2}$ in the slit direction. No flat field or offset correction was applied as these corrections are built into the system software and were not turned off under image acquisition. Care was taken to ensure that the raw pixel value vs. exposure curve had an intercept at the origin.

4.2.5 Detective Quantum Efficiency

The detector Detective Quantum Efficiency was calculated from the above results as

$$DQE(f) = \frac{MTF^2(f)}{NNPS(f)\bar{q}_o}. \qquad (4\text{-}28)$$

5 Results and Discussion

5.1 Validation of the model

For each detector configuration, beam quality and exposure used to measure the NNPS, DQE and MTF, corresponding results were predicted using Equations 3-32 – 3-38 and compared to the experimental results. System parameter values for each stage in the Cascaded Linear-Systems Model were calculated as described in Section 4.1. Also, predictions were made for detector configurations that experimental data could not be obtained for (for example it was not possible to obtain CsI:Tl samples during the period of experimental work) and the results are discussed. Furthermore, predictions of system quality metrics such as SDQE and SMTF were made using Equations 3-36 – 3-38 for various system configurations and the merits of the slit scan geometry as compared to a conventional geometry system are discussed. Figure 5-1, Figure 5-2 and Figure 5-3 show a comparison of the experimental and the measured NNPS, MTF and DQE results for the five different screen types used in the study. The results are shown in the scan and slit direction at three different exposures.

Apart from providing insight into how the detector components in their current configuration affect image quality, the model can also be used to predict potential image quality metrics resulting from design changes: Two possible upgrades to the detector include:

(1) Replacing the unstructured Gd_2O_2S:Tb screen with a structured Thallium doped Caesium Iodide screen (CsI:Tl) .

(2) Replacing the demagnifying taper with a straight coupling non-demagnifying taper that projects the screen output onto a seamless linear array of CCDs.

The effects of these possible upgrades on the Detector DQE and MTF are analysed using the model and discussed in Section 5.3.1, 5.3.2. Also the possibility of applying the model to the purpose of overall system optimisation is discussed in Section 5.1.3.

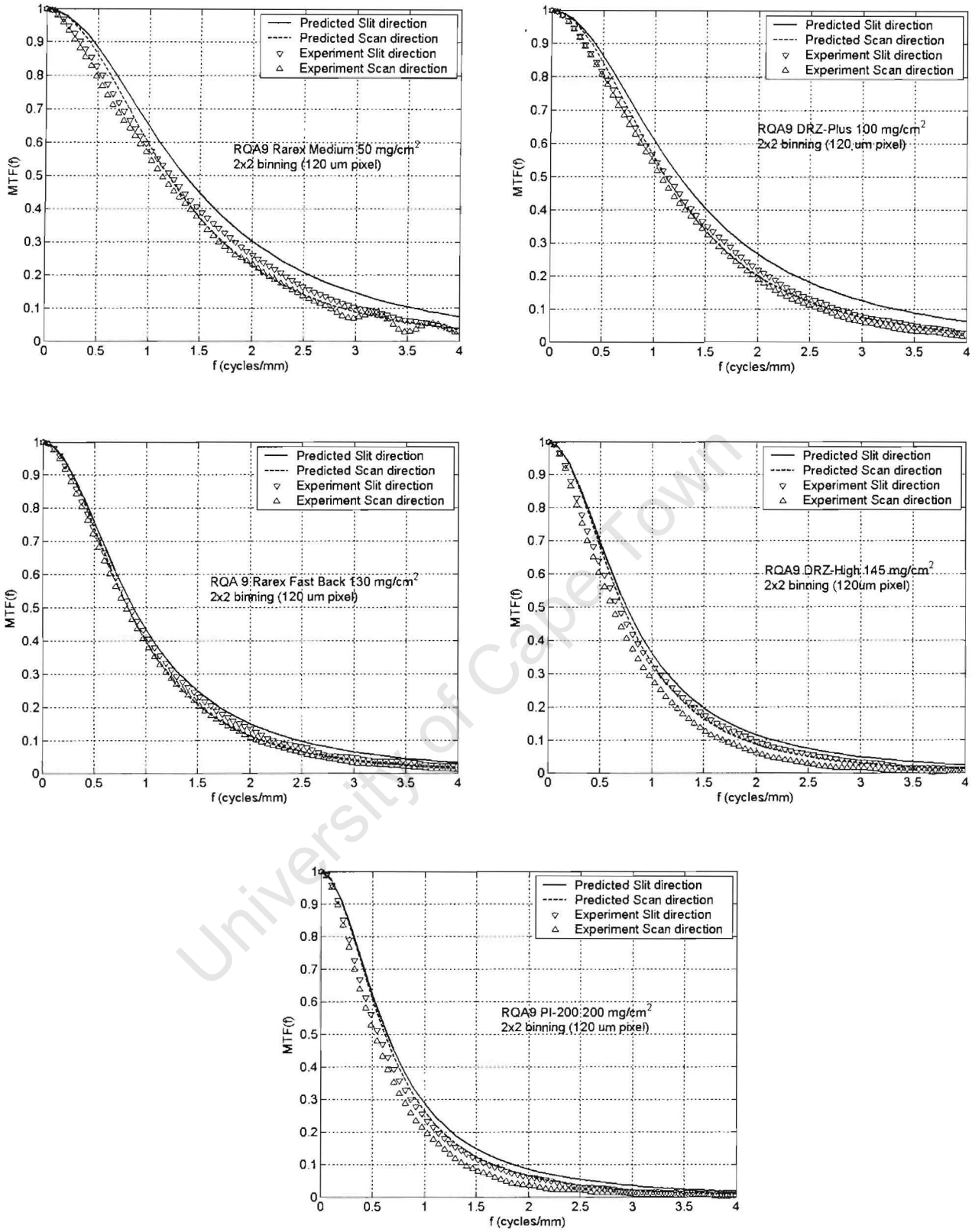

Figure 5-1 Detector MTF for detector with Rarex 50 mg/cm^2, DRZ 100 mg/cm^2, Rarex 130 mg/cm^2, DRZ 145 mg/cm^2 and PI 200 mg/cm^2 screens. Data is shown for three different exposures at RQA7 and is a comparison of measured data and theoretical prediction. All measurements and predictions were made at half scan speed (70 mm/s). For clarity, the MTF is shown in the slit direction only.

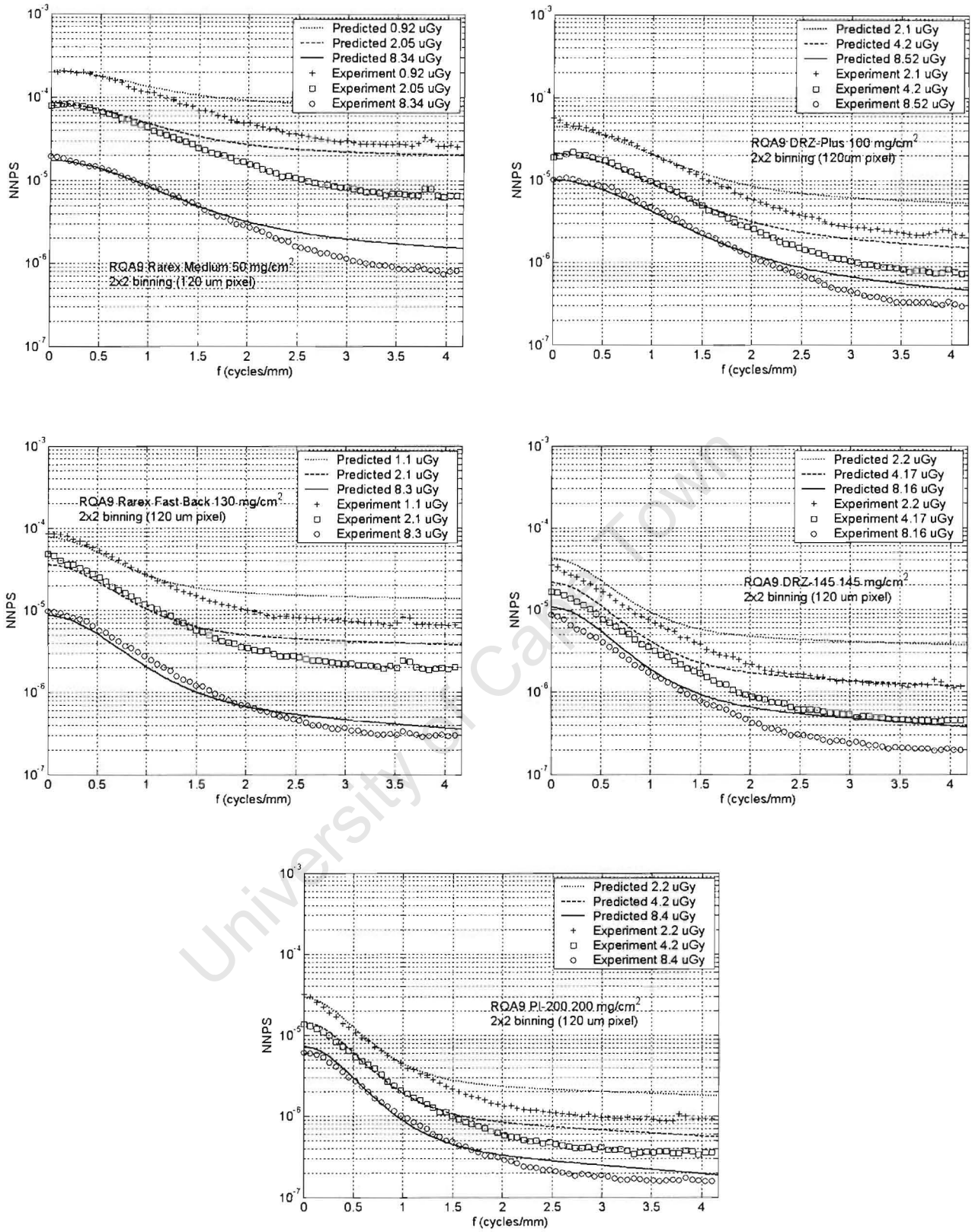

Figure 5-2 NNPS for detector with Rarex 50 mg/cm^2, DRZ 100 mg/cm^2, Rarex 130 mg/cm^2, DRZ 145 mg/cm^2 and PI 200 mg/cm^2 screens. Data is shown for three different exposures at RQA7 and is a comparison of measured data and theoretical prediction. All measurements and predictions were made at half scan speed (70 mm/s). For clarity, the NNPS is shown in the slit direction only.

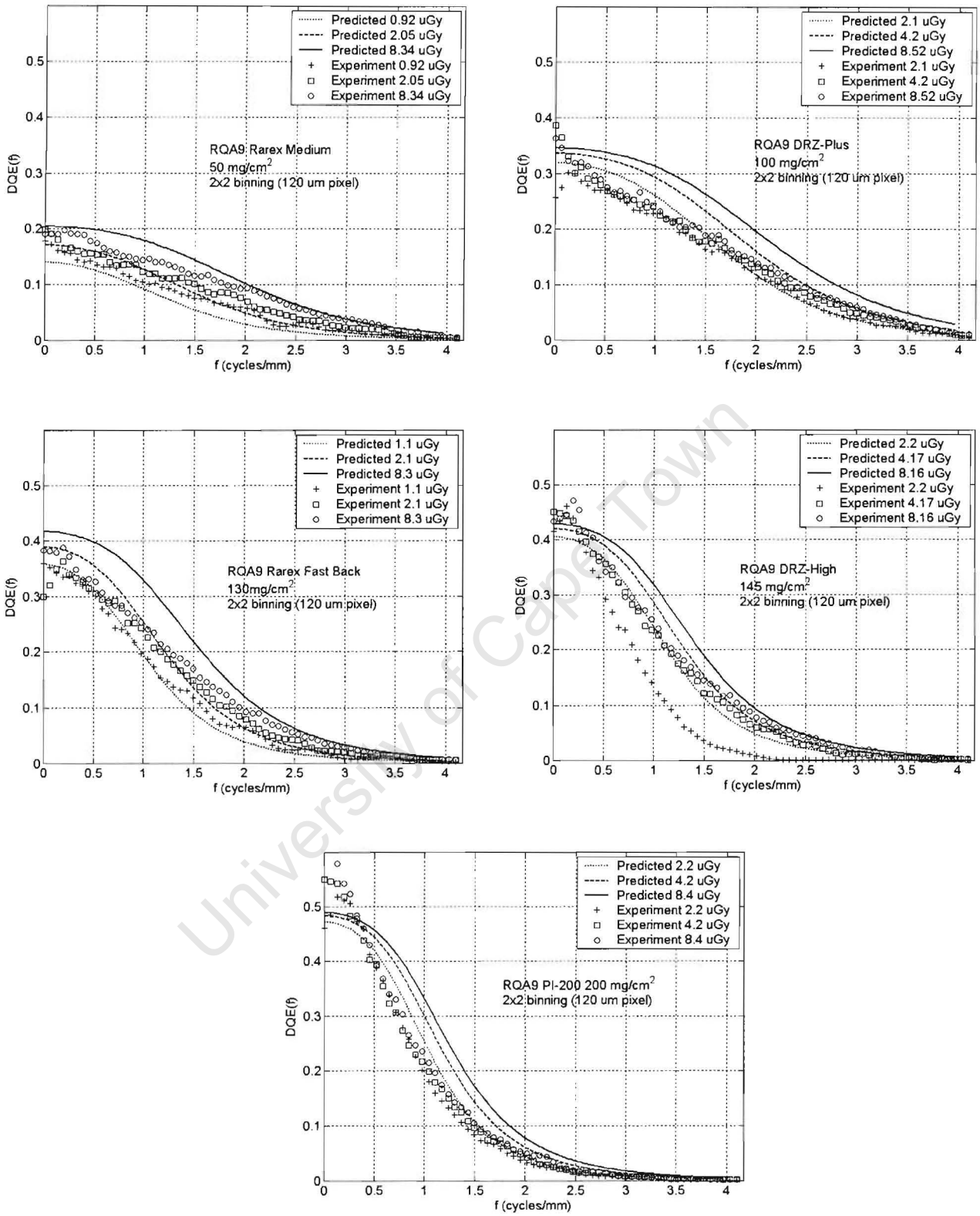

Figure 5-3 Detector DQE for detector with Rarex 50 mg/cm^2, DRZ 100 mg/cm^2, Rarex 130 mg/cm^2, DRZ 145 mg/cm^2 and PI 200 mg/cm^2 screens. Data is shown for three different exposures at RQA7 and is a comparison of measured data and theoretical prediction. All measurements and predictions were made at half scan speed (70 mm/s). For clarity, the DQE is shown in the slit direction only.

5.1.1 Detector MTF results and discussion

Figure 5-1 shows that there is good agreement at lower spatial frequencies between the predicted and measured Detector MTF. However the agreement is not as good at higher spatial frequencies with the predicted MTF considerably higher (seen as a ratio) than the measured quantity. The measured and predicted MTF in the scan direction is slightly inferior to the slit direction MTF – an expected effect of image smear due to finite phosphor persistence. Image smear has a more pronounced effect in the case of the Rarex 50 mg/mm^2 screen since the decay time constant τ remains constant but the light spreading screen MTF component is proportionally better. Reasons for the differences between measured and predicted MTF values could be:

(1) The combination of geometry blurring effects and the gap between the tungsten plate and detector (7 mm) introduces an error which reduces the actual and measured MTF. The extent to which this affects the measurement results could in principle be quantified by measuring the MTF for several known gaps between plate and detector and extrapolating the results to zero gap width. Another possibility would be to calculate the contribution of geometry blurring and gap effects to the overall MTF by using equations 4-5 and 4-9 and then to divide the geometric blur component out of the measured results.

(2) A possible misalignment between scan direction and TDI columns would reduce the actual and measured MTF [43].

(3) The effect of charge transfer inefficiency would reduce the actual and measured MTF [14].

(4) A possible scan speed-charge transfer mismatch would reduce the actual and measured MTF [60].

(5) A small degradation of the actual and measured Detector MTF may result from x-rays that are backscattered by the FOT core material reabsorbed in the screen at a site remote from the original quantum absorption. This effect could in principle be quantified by a Monte Carlo simulation of backscatter intensity and spread from the tapers for an appropriate beam quality.

(6) The spatial variation in taper demagnification introduces a degradation of the MTF. Appendix B shows a spatial map of the taper demagnification provided by Incom the taper manufacturer. Distortion resulting from these spatial variations will have an (assumed to be small) effect on the Detector PSF and hence MTF – this effect is not included in the Cascaded Linear Model.

(7) Since the screen is pressure coupled by styro-foam to the taper surface, it is possible that a further light spread occurs in areas where the screen may not be intimately coupled to the taper (this could for example occur at the taper joins). This would cause a degradation of the actual and measured Detector MTF.

5.1.2 Detector NNPS results and discussion

Figure 5-2 shows good agreement at low spatial frequencies but less agreement is shown at higher spatial frequencies. This can be explained by the squared dependence of the predicted NNPS on the predicted MTF, which is overestimated (see Section 5.1.1).

5.1.3 Detector DQE results and discussion

In Figure 5-3 reasonable agreement is shown between the predicted and measured Detector DQE results, particularly in the case of the Rarex 50 mg/cm^2 screen. It is expected that the DQE results should decrease at lower exposures since the relative effect of electronic additive noise becomes more pronounced. For all five screens used in the study greater exposure dependence is seen in the predicted results than in the measured results. Two possible reasons could be that:

(1) The gain correction algorithm described in Section 1.2 does not completely remove multiplicative noise. This could either be due to non-linearity in the detector gain or due to an insufficient number of pixels being averaged in the scan direction when creating the gain mask. This would result in increased multiplicative structured noise at higher exposures and hence a decrease in the measured exposure dependence of the DQE. The validity of this could by checked by taking several pairs of flat field images, taking their difference and checking whether the resultant noise variance is twice the noise variance of a flat field image that has been gain mask compensated.

(2) The CCD and A/D converter gains (the CCD gain is specified as a range by the manufacturer E2V) may have been underestimated causing an overestimation of the additive noise S_{I0}. The gain could in principle be calculated by using the mean-variance method [14].

Differences between predicted and measured DQE values shown at all frequencies and at all exposures are most likely due to:

(1) Deviation of the screen mass thickness from the quoted value (see Section 4.1.5).

(2) Errors in estimation of the Swank factor (see Section 4.1.6).

(3) Differences between the actual and modelled beam spectrum (see Section 4.1.1).

(4) The dose measurement may introduce an error since the exposure levels measured are low. This could perhaps be remedied by using a larger volume ionisation chamber (see Section 4.2.2) or by averaging a large number of dose measurements.

The predicted and measured value comparison of the slit and scan direction DQE for the Rarex 130mg/cm^2 screen in Figure 5-3 shows that, as predicted by theory, the scan direction DQE is slightly inferior due to finite phosphor persistence image smear.

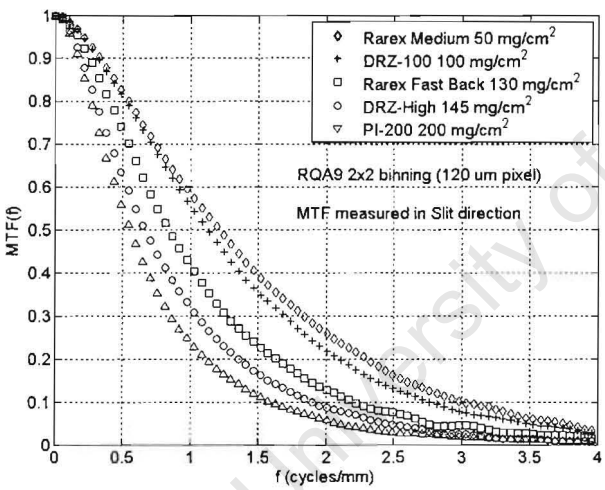

Figure 5-4 Comparison of measured detector MTF for detector with Rarex 130 mg/cm^2, Rarex 50 mg/cm^2, DRZ 100 mg/cm^2, DRZ 145 mg/cm^2 and PI 200 mg/cm^2 screens. For clarity, results are shown only in the slit direction. There appears to be a smooth variation of the curves with respect to screen mass thickness – except for the DRZ-100 screen which appears to have a comparatively good MTF given its mass thickness.

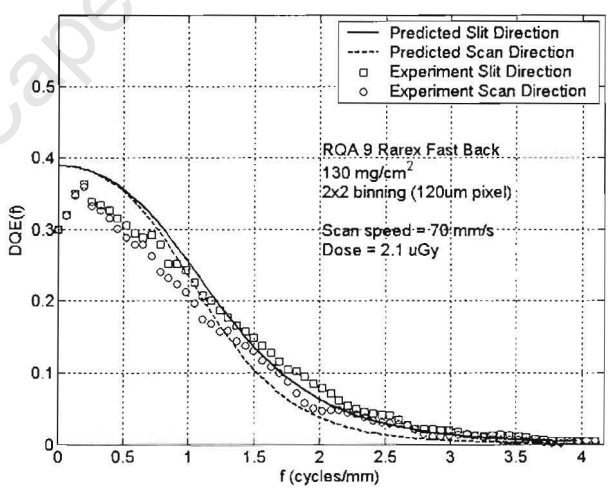

Figure 5-5 Measured and predicted DQE in the scan and slit direction for the Rarex Fast Back screen. The slightly inferior DQE in the scan direction at higher spatial frequencies was seen for all the five screens for which measurements were taken. The difference between the slit and scan direction DQE's can be attributed mainly to finite phosphor persistence and possibly also to the gap between the plate and screen causing a difference in geometry MTF contribution in the slit and scan direction.

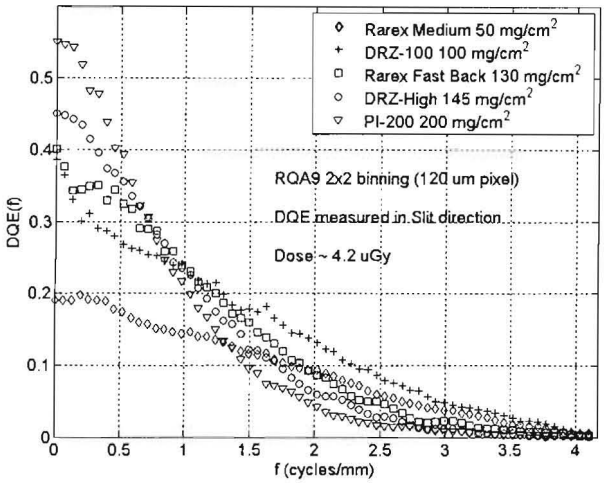

Figure 5-6 Comparison of measured Detector DQE for each screen type used in the study. Data is shown in the only slit direction for clarity. The DQE curves follow the expected tend of thinner screen having a lower high frequency DQE and vice-versa.

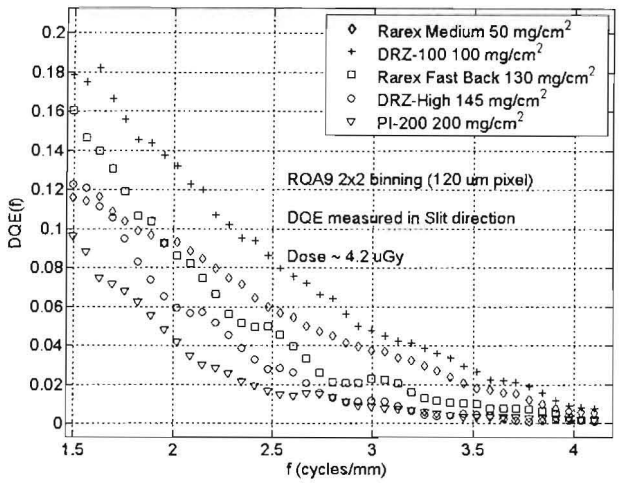

Figure 5-7 Magnified view of the measured Detector DQE in the slit direction for each screen type between 1.5 lp/mm and the Nyquist frequency. Data clearly shows the rank ordering of the different screen types at higher spatial frequencies with the DRZ-100 performing the best and the thickest screen (PI-200) performing the worst at high frequencies.

A comparison of the measured slit direction Detector MTF and DQE for all five screens used in this study is shown in Figure 5-4, Figure 5-6 and Figure 5-7. The DQE results follow the expected trend of thicker screens having higher low frequency DQE and lower high frequency DQE. The DRZ-100 mg/cm^2 screen seems to be an exception with a high frequency DQE higher than that of the next thinner screen. This can be explained by examining the MTF curves in Figure 5-1 which suggest that the DRZ-100 mg/cm^2 has a comparatively good MTF given its mass thickness.

5.1.4 Detector DQE and MTF plotted as a function of stage number

A useful method for visualizing the effect of each stage in the Cascaded Linear-Systems Model on the various frequencies of the DQE is to plot the DQE for each frequency at each stage [52] (in this case for f = 0, 1, 2 lp/mm). Such a plot is shown in Figure 5-8 and can be used for example to find the origins of high frequency Quantum Sinks or to analyse the effect of electronic noise at given exposures. A major drop equal to the Quantum Absorption Efficiency of the screen occurs at the screen absorption stage. A further frequency independent drop occurs at the Conversion Gain Stage due to Swank Noise (see Section 4.1.6). The coupling efficiency stage is responsible for a significant drop in the higher frequency DQE and a lesser drop occurs at the Additive Noise Stage. The Deterministic Blur at the Pixel Aperture Stage has no effect on the Detector DQE.

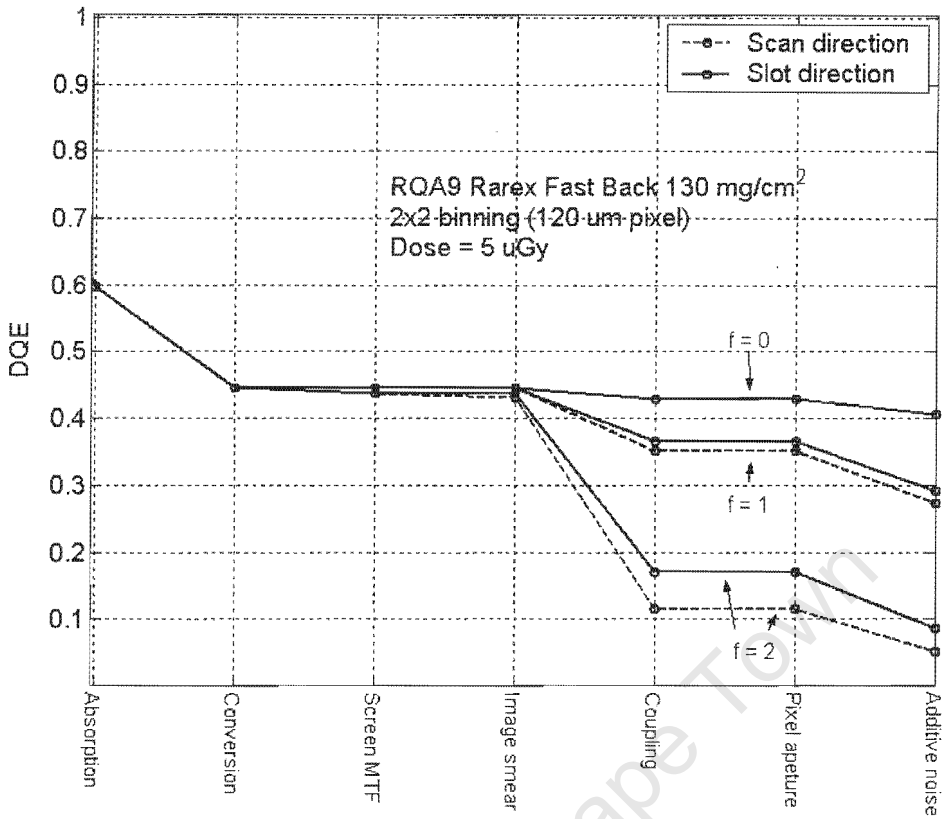

Figure 5-8 Frequency dependant Detector DQE for the system under study plotted as a function of stage number.

5.2 System DQE

The advantage of the SDQE parameter is that it allows one to include the effects of geometric blur and scatter into an overall figure of merit for a system (the relationship of this figure of merit to image quality is discussed in Section 2.2). In this section, the model is used to calculate the SDQE of the Statscan system for various parameter configurations. For comparison, the SDQE is also calculated for a hypothetical conventional geometry system (full field exposure without slit collimation) using estimates of grid attenuation and scatter to primary ratios.

5.2.1 System DQE plotted as a function of stage number

Figure 5-9 and Figure 5-10 show the SMTF and SDQE calculated for the slit scanning system under study plotted as a function stage number and for a representative set of system and detector parameters.

The most significant drop in SMTF at higher spatial frequencies (f = 1 and f = 2 cycles/mm) occurs at the Quantum Scatter Stage in the screen. A far less significant drop in MTF occurs at the pixel aperture stage which in this case is shown for 2x2 binning (giving a 120 um pixel size). This drop in MTF becomes more significant at higher binning numbers. The SMTF drops more significantly in the scan direction than in the slit direction at the geometric blur stage (Focal Spot Stage on the figure).

For the both the scan and slit directions, the most significant drops in SDQE occur at the absorption and at the coupling stage at higher frequencies. In the scan direction, a significant drop in the higher frequency SDQE occurs at the geometric blur stage Focal Spot on the figure) since the SDQE is proportional to the squared MTF at that stage. This suggests that a narrower collimator width and narrower focal spot (see Section 4.1.2.2) and the corresponding cost in tube heat loading and instantaneous power should be looked at.

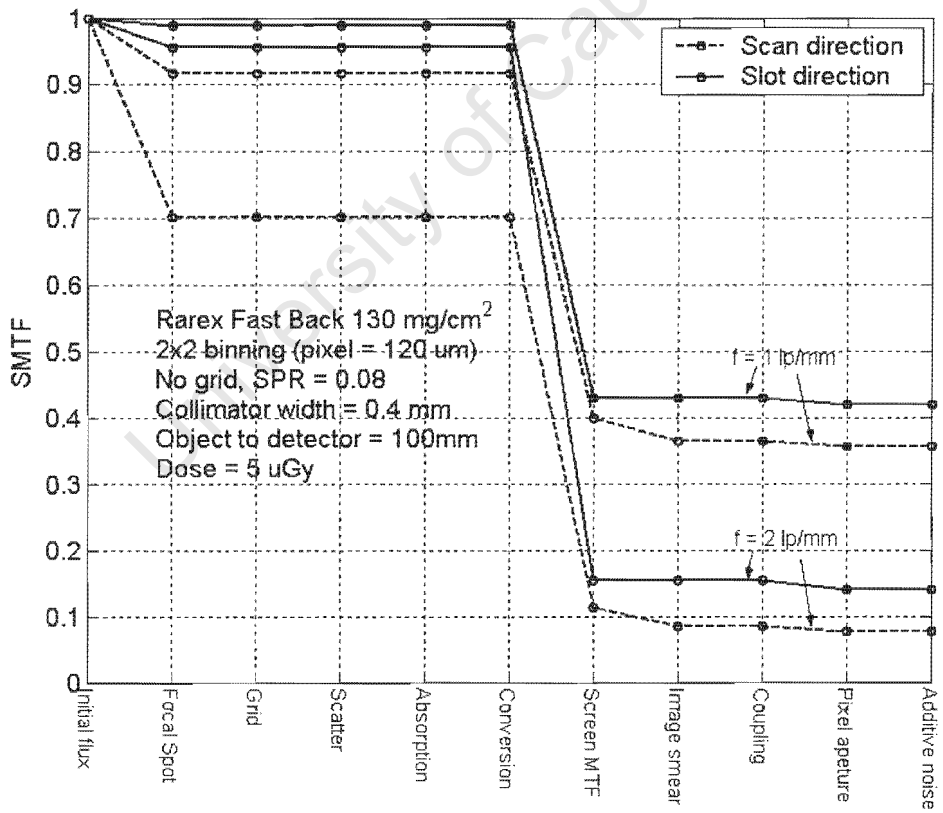

Figure 5-9 Stage dependant System MTF calculated for the slit scanning system under study.

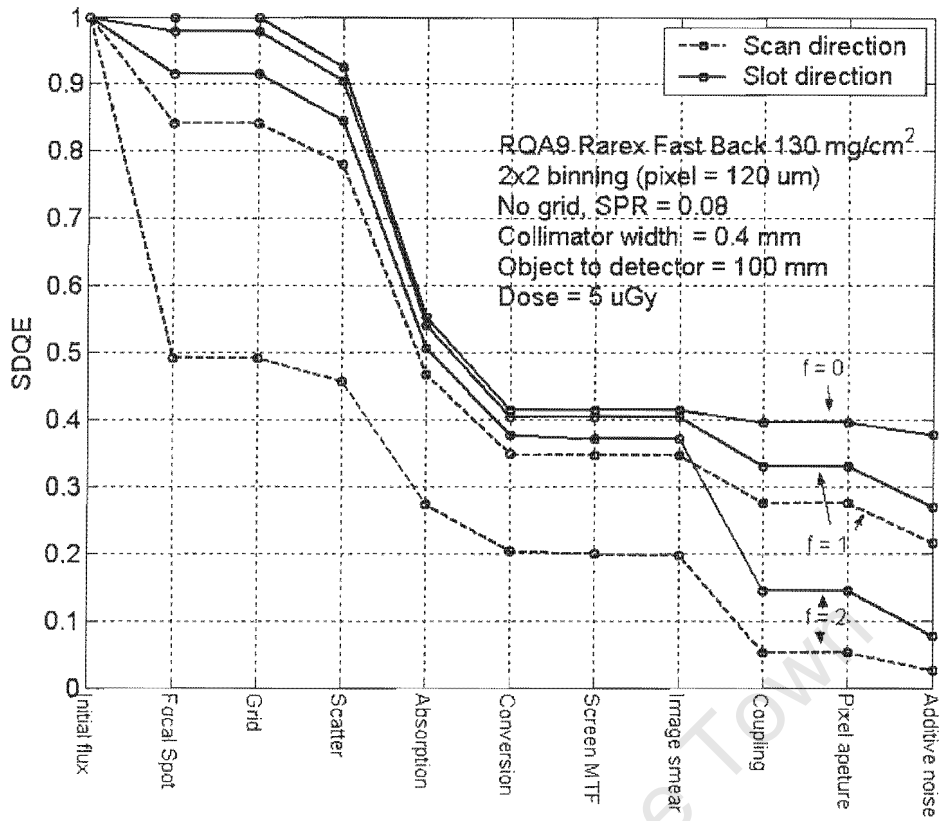

Figure 5-10 Stage dependant System DQE calculated for the slit scanning system under study.

5.2.2 Comparison of slit scanning system and conventional geometry system

Calculation of the System DQE requires knowledge of the SPR and grid attenuation for the specific system and imaging task under study. Figure 4-13 shows SPR results for the Statscan system as calculated by Monte Carlo simulation. For the phantoms, air gap and beam widths used in the Monte Carlo simulation study, the SPR has an almost linear relationship to beam width.

For the purpose of the calculations in this section, a typical SPR for the slit scanning system was taken as 0.1 (corresponding to approximately 20 cm of water. The SPR was taken as 0.7 for a conventional geometry system with a grid [5, 75] - in practice this value is highly variable and dependant on the imaging task. A typical primary beam attenuation value for a grid in a conventional geometry system was taken as 0.5 [71].

Figure 5-11 shows the stage dependent SDQE (f) calculated for two systems with different geometry but identical detectors (RQA7, Rarex 130 mg/cm^2, 120 um pixel and Dose = 5μGy). The effects of geometric blur have been ignored (i.e., the geometric blur stage has been left out). For the purposes of this example the slit scanning geometry was chosen to have no grid and a scatter to primary ratio (SPR) of 0.08, whereas the conventional geometry system was chosen to

have a grid with a 50 % transmission efficiency and a scatter to primary ratio of 0.7. The first two stages – grid attenuation and scatter - degrade the SDQE to such an extent in the conventional geometry system that even an ideal detector with a DQE of unity would still result in a "System DQE" lower than the slit scanning system. The results show that the efficiency of the conventional geometry system is significantly degraded by the system level effects of scatter and grid attenuation. Clearly the slit scanning system has a higher "System DQE" in this case.

For the same parameter values used above, Figure 5-12 shows the System DQE calculated with geometric blur effects ignored for the slit scanning system and a conventional geometry system with identical detectors (the Detector DQE is shown on the same curve).

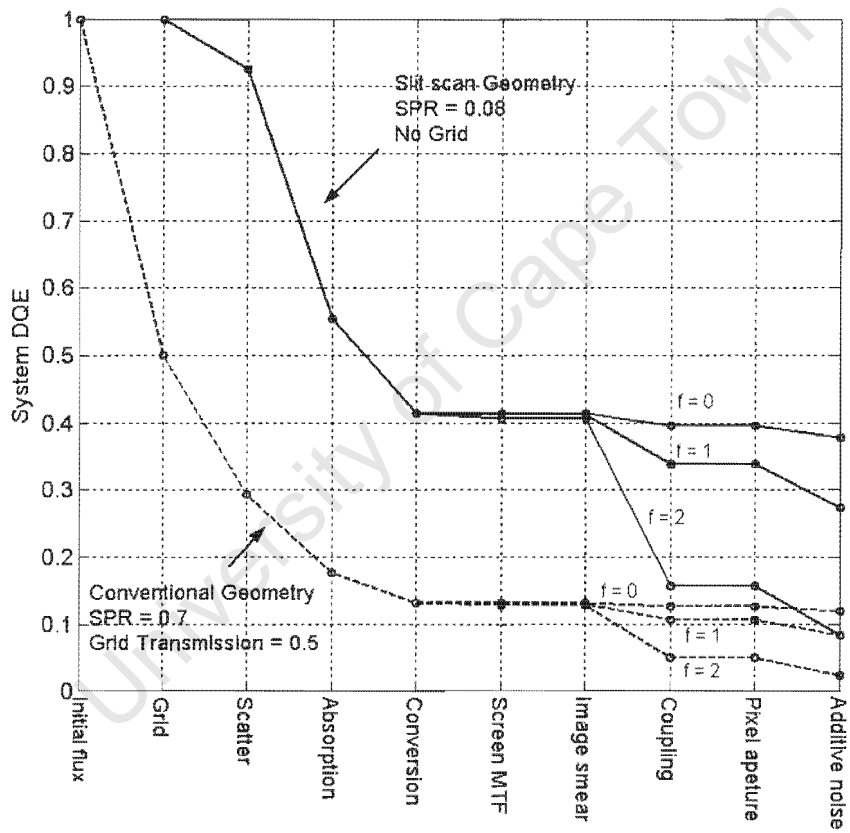

Figure 5-11 Stage dependent SDQE calculated for two systems with different geometry but identical detectors (RQA7, Rarex 130 mg/cm^2, 120 um pixel and Dose = 5μGy). The SDQE is plotted at three spatial frequencies: f = 0, f = 1 and f = 2 lp/mm. The high frequency drop is apparent in both systems at the coupling stage, and the quantum absorption stage of screen reduces all spatial frequencies by a large factor in both systems. Only the conventional geometry system suffers a large drop in SDQE at the grid attenuation and scatter stages.

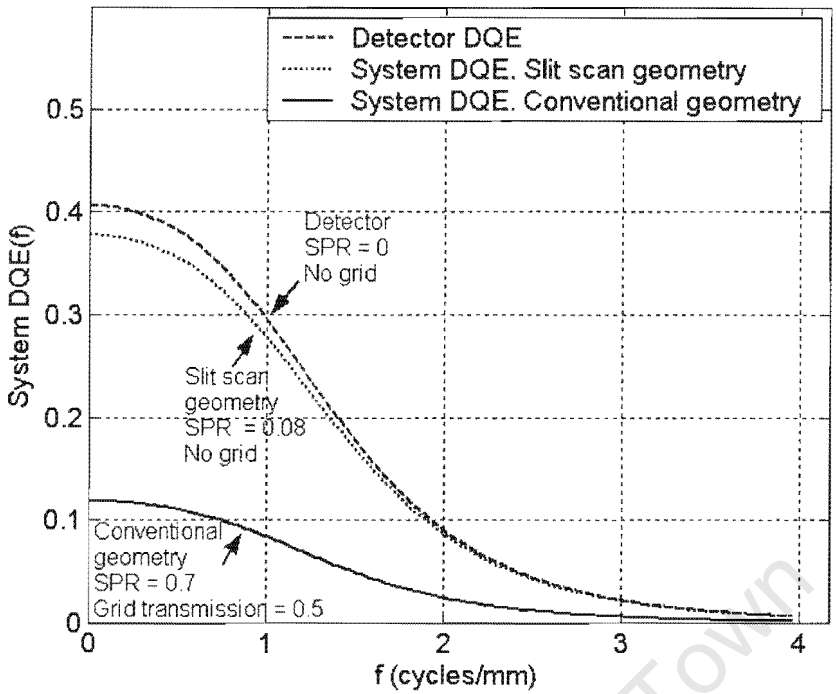

Figure 5-12 System and Detector DQE calculated for RQA7, Rarex 130 mg/cm^2, 120um pixel detector and two different grid and scatter combinations. The Slit scan geometry performs significantly better than a conventional geometry system with an identical detector.

5.3 Example applications of the model

5.3.1 Possible detector upgrades – CsI, straight coupling

The FOT coupling introduces an undesirable high frequency drop (see Figure 5-3, Figure 5-8 and [44]) into the Detector DQE. An improvement in the Detector DQE could be made by removing the FOT coupling and replacing it with a non-demagnifying fibre optic plate (FOP) that projects the screen output directly onto a butted linear array of CCD's. The Detector DQE could be further improved by replacing the current unstructured screen with a structured CsI:Tl screen: allowing greater quantum absorption efficiency for similar or superior resolution [87]. Figure 5-13 shows the Detector DQE calculated for various combinations of screen and coupling type. For the CsI:Tl screen and the two possible coupling combinations, the following parameters values were used [27, 87] : $g_4 = 0.8$; $g_5 = 1550$; $e_5 = 273$; $H = 0.49$; $g_8 = 0.014$ (FOT coupling), $g_8 = 0.1$ (FOP coupling) ; $a = 0.06$ mm; $b = 2$. The results in Figure 5-13 show that a significant improvement in the Detector DQE is possible. Further investigation in the form of a prototype detector for testing is recommended since the improvement in DQE will reduce patient dose, reduce tube loading limitations and improve image quality.

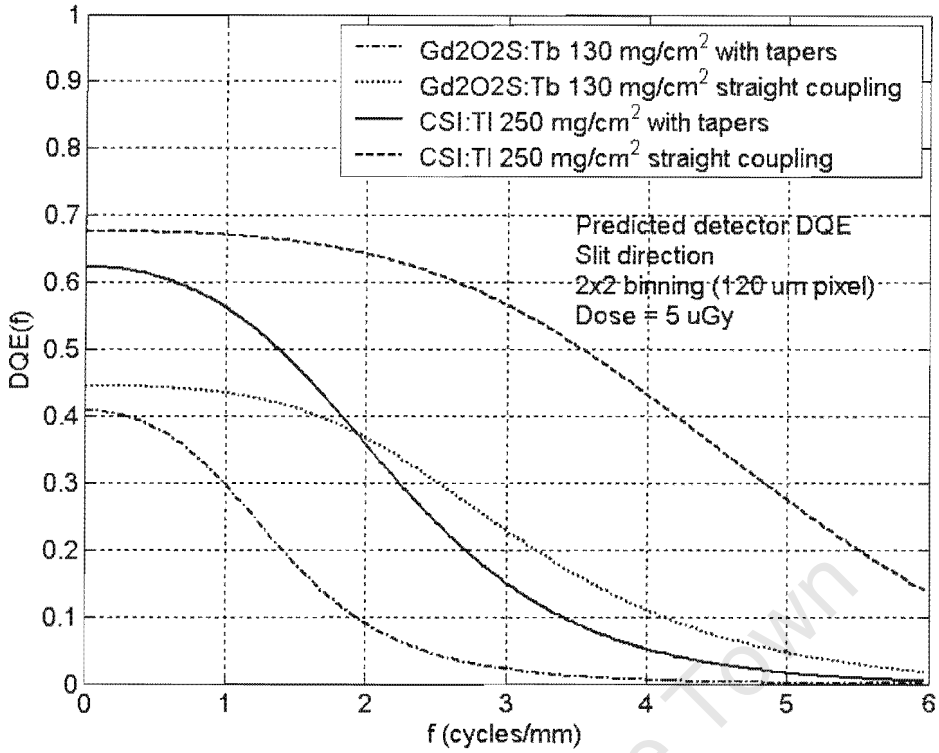

Figure 5-13 Predicted Detector DQE at RQA7 for various detector configurations. Large gains in the Detector DQE (especially at high frequencies) can be made by removing the coupling tapers and by replacing the unstructured screen with a structured CsI:Tl screen.

5.3.2 Improved heat loading by using asymmetrical focal spot

When selecting the focal spot size, there is a trade off between instantaneous power and spatial resolution. Larger focal spots have improved instantaneous power and are less expensive but have diminished spatial resolution. There is currently a motivation to use a larger focal spot in Statscan in order to reduce cost and increase duty cycle. The purpose of this section is to analyse the effect of focal spot size and shape on spatial resolution and to give an approximate recommendation for what shape and size focal spot can be used to improve heat loading and cost for a minimum loss in resolution.

For the current focal spot dimensions and machine settings - collimator width C_w = 0.4 mm, source to collimator SC = 400 mm, Object to detector OD = 200 mm, SD = 1300 mm and focal spot width F_w = 0.6 mm - the component MTF's due to geometric blur and other effects are shown in Figure 5-14. Also shown is the detector MTF and System MTF (measured and theory – the system MTF was measured by raising the tungsten plate above the detector). It is clear that the geometric MTF in the slit direction is superior to the geometric MTF in the scan direction. The

result is that system resolution is inferior in the scan direction. This suggests that an asymmetrical focal spot with increased length in the slit direction may be optimal in terms of the trade off between geometric resolution and instantaneous power/ tube heat loading.

Figure 5-15 shows the component MTF's for a focal spot having dimension 1.2 mm in the slit direction and 0.6 mm in the scan direction. Even a doubling of the focal spot dimension in the slit direction does not degrade the slit direction geometrical resolution to the level seen in the scan direction.

Although it is difficult to predict the visual effect of a slight reduction of resolution in one direction, it can be said that a doubling in focal spot area can be achieved for what appears to be a comparatively small loss in resolution.

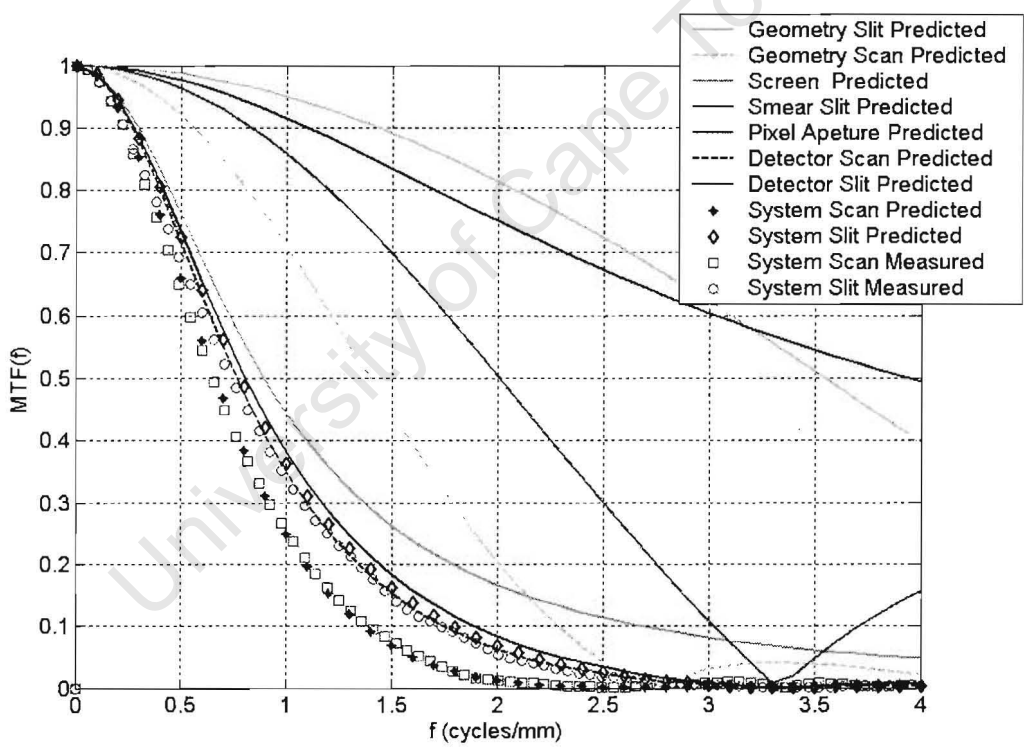

Figure 5-14 Component MTF's, System MTF and Detector MTF measured and predicted for the case of a symmetrical focal spot 0.6 x 0.6 mm. Note that the geometrical MTF in the slit direction is far superior to the geometrical MTF in the scan direction

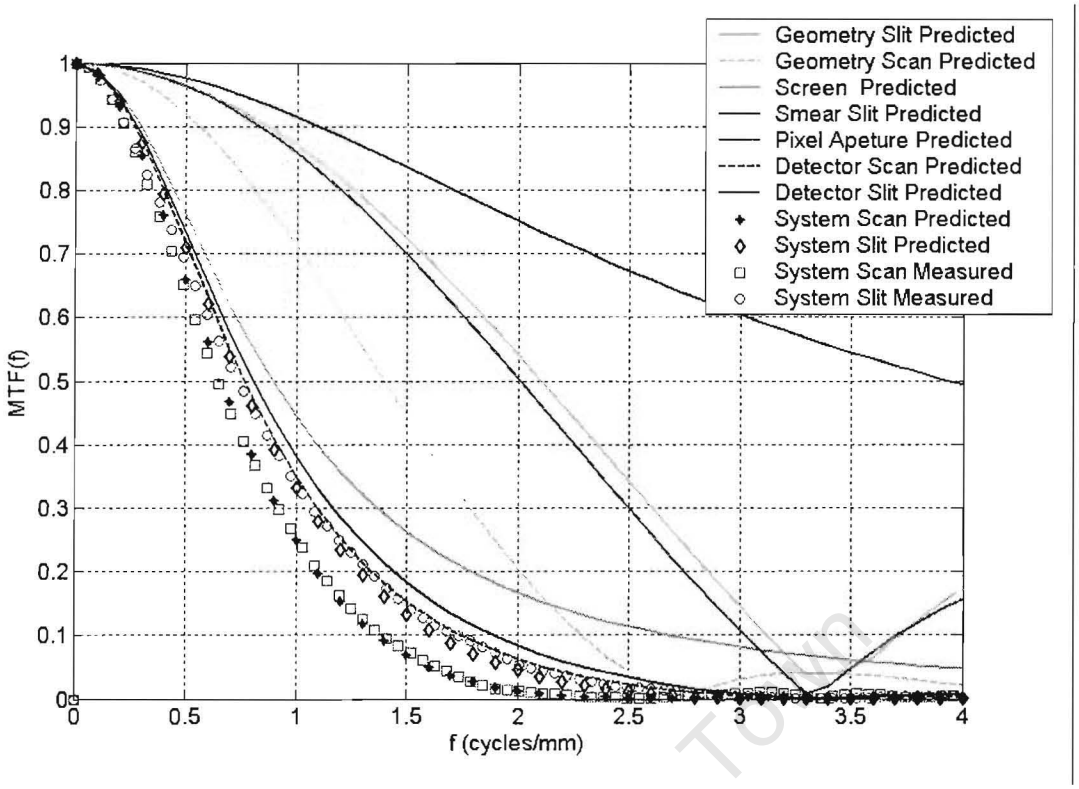

Figure 5-15 Component, System and Detector MTF's measured and predicted for the case of an asymmetrical focal spot with dimension 1.2 x 0.6 mm. This corresponds to a doubling in the focal spot length in the slit direction. Note that the geometrical MTF in the slit direction is still superior to the geometrical MTF in the scan direction (but to a lesser extent).

6 Conclusions and Recommendations

This study has concentrated mainly on developing a multiparameter model of the imaging efficiency of Statscan system using the MTF, Detector DQE and the System DQE (SDQE) as figures of merit. Attempts were made to find generalized expressions for physical parameters used in the model, and where this was not possible, measurements were made for specific cases or estimates were made based on previous studies in the literature. As far as possible the parameter model was validated by taking DQE measurements and comparing against theoretical results. In the case of the SDQE figure of merit – where no method exists for direct measurement - the accuracy of the extra parameters needed to define the SDQE (SPR, grid attenuation and geometric blur) were verified as far as possible.

The Scatter to Primary values for the Statscan system were obtained by Monte Carlo simulation which provides accurate data and which allows one to rapidly prototype new geometry configurations for the machine since changes need only be made in software. However since idealised patient models are used (in this study blocks of water were used to represent the patient), the Monte Carlo results can only be an approximation with unknown systemic error to what the SPR is in reality. Therefore, it is suggested that Monte Carlo simulation is used to investigate new possibilities for the geometry configuration (e.g. slit width and depth) and that the beam stop method [63] is subsequently used to measure results for more realistic patient models (e.g. real patients or anthropomorphic phantoms).

The Cascaded Linear-Systems model can be used to predict system image quality metrics to a reasonable degree of accuracy (within about 15 % of the measured quantity for the DQE and within 10 % for the MTF up to the Nyquist frequency). The model also gives robust results (to a similar degree of accuracy) over a range of detector entrance doses (2.3 to 8.5 uGy) and screen types (50 to 200 mg/cm^2 Gadox). This is encouraging in that it suggests that the model can be used to provide system insight and that system design can be improved by the optimisation of model parameters. However the model does have limitations in that it is based on the assumption of linearity, stationarity and noise with wide sense cyclo-stationary properties. In a sense this can be interpreted as "The Cascaded Linear-systems model only applies to the gross imaging capabilities of the system". This means that spatially variant artefacts such as those at the seams between cameras, spatial distortion due to spatially variant de-magnification in the FOT (see

Appendix B) and failure of the gain correction algorithm due to non-linearity at low exposures are not covered by the model in its present form.

It was shown in Section 5.2.2 that a significantly higher SDQE can be attained by a slit scanning system than by a conventional geometry systems suggesting that slit scanning is the more dose efficient paradigm for x-ray imaging. This is well known in the medical imaging literature and has been shown by measurement on existing systems [14, 22, 43, 49]. Although the low dose has been explained in the literature as being a result of slit scanning systems having no grid and a lower SPR, it is believed by the author that no analytical method has been applied to the different geometry types to quantify the "dose efficiency" of slit scanning systems. This study examines such a method in the form of the SDQE and looks analytically at the relationship between SPR, grid characteristics, geometry and imaging efficiency. At the present time the status and merit of the SDQE parameter is not established in the literature although it has a direct relationship to detectability by an ideal observer [27]. This suggests that it may be useful for x-ray imaging machine manufactures to quote the SDQE as well as the Detector DQE when giving an evaluation of their system in order to give an overall idea of the imaging efficiency of the system.

Although slit scanning systems allow low dose imaging, in practice tube heat loading considerations still place a practical limit on the thickness of patient from which a satisfactory image can be obtained. Further work using the model and tube heat loading characteristics is recommended in order to find possible optimisations in this area (e.g. by varying the scan speed and collimator slit width dynamically).

A useful application of the model developed in this thesis would be the optimisation of the machine physical parameters using a figure of merit that describes absolute image quality in terms of the SNR and resolution properties [27]. An example of a physical parameter for which an optimum could be found for specific imaging tasks is the collimator slit width. It was explained in Section 4.1.2.2 and 4.1.4 that the collimator slit width affects spatial resolution, the SPR and the total primary flux $\bar{q}_0$ incident on the detector. For a specific imaging task it is possible to calculate the geometric blur, SPR and primary flux incident over a continuous range of collimator slit widths. These values could in turn be used as input to calculate the Detectability Index described in Section 2.2 to find the optimum slit width for a specific imaging task. Results obtained from such a study would only be useful in a situation where constraints due to x-ray tube loading are not an issue (e.g. in a thin patient or a short scan) and where the slit width can be varied

dynamically (and does need to be set one time by the manufacturer to accommodate large patients and long scans).

Furthermore, the study could be validated by checking whether the optima found apply to lesion detection in a clinical setting with real patients or anthropomorphic phantoms. This validation is necessary since in a clinical setting there are complicating factors such as anatomic noise, the display conditions and the characteristic of the human visual system to take into account.

The main idea the author is trying to communicate is that the format of the Cascaded Linear Systems allows the investigator to break down the image formation process, to compare different image modalities and to gain insight into the principles that allow slit scanning systems to take lower dose images. The Cascaded Linear Model has been written up in MATLAB, with the intention of it being used as an investigative tool and it is simple to re-run the model for any chosen model parameter values.

References

[1] S. Surujdhal, "An x-ray model to predict system performance in terms of dose and image quality." De Beers Technology Documentation 1998.

[2] M. C. Steyn, "SCANNEX Detector theoretical evaluation." De Beers Technology Documentation 1997.

[3] A. Booysen, D. Biago, "LODOX Image Quality Review and Specification." De Beers Technology Documentation 1998.

[4] GW. Over, "Preliminary design evaluation for the optical detector unit for the proposed LODOX x-ray machine." De Beers Technology Documentation 1997.

[5] G. T. Barnes, X. Wu, P. C. Sanders, "Scanning Slit Chest Radiography: A Practical and Efficient Scatter Control Design." Radiology 190:525-528, 1994.

[6] L. J. M. Kroft, J. Geleijns, B. J. A. Mertens, "Digital Slit-Scan Charge-Coupled Device Radiography versus AMBER and Bucky Screen-Film Radiography for Detection of Simulated Nodules and Interstitial Disease in a Chest Phantom." Radiology 231:156-163, 2004.

[7] E. Samei, R. S. Saunders, J. Y. Lo, J. T. Dobbins, J. L. Jesneck, C. E. Floyd, C. E. Ravin, "Fundamental imaging characteristics of a slit-scan digital chest radiographic system." Medical Physics 31:2687-2698, 2004.

[8] S. Beningfield, H. Potgieter, A. Nicol, S. van As, G. Bowie, E. Hering, E. Latti, "Report on a new type of trauma full-body digital X-ray machine." Emergency Radiology, 10: 23-29, 2003.

[9] M. de Villiers and G. de Jager, "Detective Quantum Efficiency of the LODOX System." Proc. of SPIE Vol 5030, 955-960, Medical Imaging, 2003.

[10] M. Rabbani, R. Van Metter, "Analysis of signal and noise propogation for several imaging mechanisms." Journal of the Optical Society of America A/Vol. 6, No 8: 1156-1164, August 1989.

[11] "Medical electrical equipment – Characteristics of digital X-ray imaging devices – Part 1: Determination of the detective quantum efficiency." IEC 62220-1, International Electrotechnical Commission, 2003.

[12] S. Thunberg, T. Francke, J. Egerstroem, M. Eklund, L. Ericsson, T. Kristoffersson, V. Peskov, J. Rantanen, S. Sokolov, P. Svedenhag, C. Ullberg, N. Weber, "Evaluation of a Photon Counting Mammography System." Proc. of SPIE Vol. 4682, Medical Imaging 2002.

[13] I. S. Kyprianou, S. Rudin, D. R. Bednarek, K. R. Hoffman, "Study of the Generalized MTF and DQE for a New Microangiographic System." Proc. of SPIE Vol. 5368, 349-360, Physics of Medical Imaging 2004.

[14] D. W. Holdsworth, R. K. Gerson, A. Fenster, "A time-delay integration charge-coupled device camera for slit-scanned digital radiography." Medical Physics 17, 876-886, 1990.

[15] E. Samei, "Image quality in two phosphor-based flat panel digital radiographic detectors." Medical Physics 30 (7), 1747-1757, 2003.

[16] J. T. Dobbins III, "Effects of undersampling on the proper interpretation of modulation transfer function, noise power spectra, and the noise equivalent quanta of digital imaging systems." Medical Physics 22 (2), 171-180, 1995.

[17] M. L. Giger, K. Doi, "Investigation of basic imaging properties in digital radiography. I Modulation transfer function." Medical Physics 11 (3), 287-295, May/Jun 1984.

[18] P. R. Granfors, R. Aufrichtig, "Performance of a 41x41-cm^2 amorphous silicon flat panel x-ray detector for radiographic imaging applications." Medical Physics 27 (6), 1324-1331, 2000.

[19] I. A. Cunningham, J. Yao, V. Subotic, "Cascaded Linear-Systems Models and the DQE of Flat-Panels Imagers: Noise Aliasing, Secondary Quantum Noise and Reabsorbtion." Proc. of SPIE Vol. 4682, 61-72 (2002).

[20] E. Samei, M. J. Flynn, D. A. Reimann, "A method for measuring the presampled MTF of digital radiographic systems using an edge test device." Medical Physics 25 (1), 102-113, 1998.

[21] K. Stierstorfer, M. Spahn, "Self-normalising method to measure the detective quantum efficiency of a wide range of x-ray detectors." Medical Physics 26 (7), 1312-1319, 1999.

[22] P. Despres, G. Beaudoin, P. Gravel, J. A. de Guise, "Physical characteristics of a low-dose gas microstrip detector for orthopedic x-ray imaging.", Medical Physics, 32 (4), 1193-1204, 2005.

[23] U. Neitzel, S Gunther-Kohfahl, G. Borasi, E. Samei, "Determination of the detective quantum efficiency of a digital x-ray detector: Comaprison of three evaluations using a common image data set." Medical Physics 31 (8), 2205-2211, 2004.

[24] P. Monnin, D. Gutierrez, S. Bulling, "Performance comparison of an active matrix flat panel imager, computer radiography system, and a screen-film system at four standard radiation qualities." Medical Physics, 32 (2), 343-350, 2004.

[25] J. H. Siewerdsen, L.E. Antonuk, "DQE and System Optimisation for Indirect-Detection Flat-Panel Imagers in Diagnostic radiology." Proc. Of SPIE Vol. 3336, 484 – 493, Physics of Medical Imaging, 1998.

[26] I. S. Kyprianou, S. Rudin, D. R. Bednarek, K. R. Hoffman, "Generalizing the MTF and DQE to include x-ray scatter and focal spot unsharpness: Application to a new microangiographic system." Medical Physics 32 (2), 613-626, 2005.

[27] J. H. Siewerdsen, D. A. Jaffray, "Optimisation of x-ray imaging geometry (with specific application to flat-panel cone-beam computed tomography." Medical Physics 27: 1903-1914, 2000.

[28] W. A. Kalender, "Calculation of x-ray grid characteristics by Monte Carlo methods." Physics in Medicine and Biology, Vol. 27, No. 3, 353-361, 1982.

[29] H-P Chan, K. Doi, "Investigation of the performance of antiscatter grids: Monte Carlo simulation studies." Physics in Medicine and Biology, Vol. 27, No. 6, 785-803, 1982.

[30] H-P Chan, K. Doi, "Studies of performance of antiscatter grids in digital radiography: Effect on signal-to-noise ratio." Medical Physics 17 (4), 655-664, 1990.

[31] C. E. Metz, R. F. Wagner, D. G. Brown, R. M. Nishikawa, K. L. Myers, "Toward consensus on quantitative assessment of medical imaging systems.", Medical Physics 22(7):1057-1061, 1995.

[32] I. A. Cunningham, "Chapter 2: Applied Linear-Systems Theory." from The Handbook of Medical Imaging, Volume 1. Physics and Psychophysics, Editors J Beutel, H. L. Kundel, R. L. Van Metter, SPIE Press, 2000.

[33] A. Ganguly, S. Rudin, D. R. Bednarek, K. R. Hoffman, "Micro-angiography for neuro-vascular imaging. II. Cascade model analysis." Medical Physics 30 (11), 3029-3039, 2003.

[34] A. Ganguly, S. Rudin, D. R. Bednarek, K. R. Hoffman, "Micro-angiography for neuro-vascular imaging. I. Experimental evaluation and feasability." Medical Physics 30 (11), 3029-3039, 2003.

[35] S. Richard, J. H. Siewerdsen, D. A. Jaffray, D. J. Modely, B. Bakhtiar, "Generalized DQE Analysis of Dual-Energy Imaging using Flat-Panel Detectors.", Proc. Of SPIE Vol, 519 – 528, 2005.

[36] R. F. Wagner, G. T. Barnes, B. S. Askins, "Effect of reduced scatter on radiographic information content and patient exposure: a quantitative demonstration." Medical Physics Vol. 7, 13-18, 1980.

[37] M.S. Westmore, I.A. Cunningham. "Analysis of the DQE of coupling a CCD to a scintillating phosphor for x-ray microtomographic imaging." Proc. of SPIE Vol. 1896, 82-92, 1993.

[38] M. B. Williams, P. U. Simoni, L. Smilowitz, M. Stanton, W. Philips, A. Stewart, "Analysis of the detective quantum efficiency of a developmental detector for digital mammography." Medical Physics 26 (11), 2273-2285, 1999.

[39] W. Zhao, J. A. Rowlands, "Digital radiology using active matrix readout of amorphous selenium: Theoretical analysis of detective quantum efficiency." Medical Physics 24 (12), 1819-1833, 1997.

[40] J. H. Siewerdsen, L. E. Antonuk, Y. El-Mohri, J. Yorkston, W. Huang, I. A. Cunningham. "Signal, noise power spectrum, and detective quantum efficiency of indirect-detection flat-panel imagers for diagnostic radiology." Medical Physics 25:614-628, 1998.

[41] J. H. Siewerdsen, L. E. Antonuk, Y. El-Mohri, J. Yorkston, W. Huang, I. A. Cunningham. "Empirical and theoretical investigation of the noise performance of indirect detection, active matrix flat-panel imagers (AMFPIs) for diagnostic radiology." Medical Physics 24:71-89, 1996.

[42] Hetal Ved, "A Cascaded Linear-Systems Modeling and experimental approach to the physical characterization of a mammography machine." Thesis, Worcester polytechnic, Worcester, England, 2002.

[43] J. G. Mainprize, N. L. Ford, S. Yin, T. Tumer, M. J. Yaffe, "A slit-scanned photodiode-array/CCD hybrid detector for digital mammography." Medical Physics 29:214-225, 2002.

[44] I. A. Cunningham, M. S. Westmore, A. Fenster, "A spatial-frequency dependent quantum accounting diagram and detective quantum efficiency model of signal and noise propogation in cascaded imaging systems." Medical Physics 21(3), 417 – 427, March 1994.

[45] M. Rabbani, R. Shaw, R. Van Metter, "Detective quantum efficiency of imaging systems with amplifying and scattering mechanisms." Journal of the Optical Society of America A, Vol. 4, No. 5, 895 – 901, May 1987.

[46] L. T. Niklason, J. A. Sorenson, J. A. Nelson, "Scattered radiation in chest radiography." Medical Physics 8 (5), 677-681, 1981.

[47] M. M. Levine, J. Hale, "Variation of the scatter to primary ratio in diagnostic radiology." Physics in Medicine and Biology, Vol. 25, No. 3, 545-548, 1980.

[48] D. C. Kushner, R. H. Cleveland, T. E. Herman, T. C. McLoud, A. C. Waltman, J. O. Shepard, C. G. Dedrick, D. B. Kopans, R. E. Greene, "Low-Dose Flying Spot Digital Radiography of the Chest: Sensitivity Studies." Radiology 163:685-688, 1987.

[49] M. M. Tesic, R. A. Sones, D. R. Morgan, "Single-Slit Digital Radiography: Some Practical Considerations." Amateur Journal of Ronetgenol, 142:697-702 , 1984.

[50] D. Plenkovich, J. A. Sorenson, R. A. Kruger, "Scatter rejection by electronic collimation." Medical Physics, 13 (2), 158-163, 1986.

[51] P. Despres, G. Beaudoin, P. Gravel, J. A. de Guise, "Evaluation of a full-scale gas microstrip detector for low-dose X-ray imaging.", Nuclear Instruments and Methods in Physics Research A 536:52-60, 2005.

[52] G. Charpak, R. Bouclier, T. Rressani, J. Favier, C. Zupancic, "The use of multiwire proportional chambers to select and localize charged particles." Nuclear Instruments and Methods in Physics Research A, 263, 351-359, 1988.

[53] G. T. Barnes, H. M. Cleare, I. A. Brezovich, "Reduction of Scatter in Diagnostic Radiology by Means of a Scanning Multiple Slit Assembly." Radiology 120:691-694, 1976.

[54] G. T. Barnes, I. A. Brezovich, "The design and performance of a scanning multiple slit assembly." Medical Physics, 6(3), 197-204, 1979.

[55] B. S. Slasky, "Digital radiography of the chest by self-scanning linear diode arrays." Acta Radiology 28:461-466, 1987.

[56] D. C. Kushner, R. H. Cleveland, T. E. Herman, D. J. Zaleske, M. G. Ehrlich, J. A. Correia, "Radiation Dose Reduction in the Evaluation of Scoliosis: An Application of Digital Radiography." Radiology 161:175-181, 1986.

[57] R. A. Sones, K. L. Lauro, C. L. Cattell, "A detector for scanned projection radiography." Radiology 175:553-559, 1990.

[58] H. Vlasbloem, L. J. Schultze Kool, "AMBER: A scanning Multiple-Beam Equalization System for Chest Radiogaphy." Radiology 169:29-34, 1988.

[59] J. D. Armstrong II, J. A. Sorenson, J. A. Nelson, I. Tocino, P. D. Lester, J. O. Janes, L. T. Niklason, W. Stanish, "Clinical Evaluation of Unsharp Masking and Slit Scanning Techniques in Chest Radiography." Radiology 147:351-356, 1983.

[60] A. D. A Maidment. M. Y. Yaffe, D. B. Plewes, G. E. Mawdsley, I. C. Soutar, B. G. Starkoski, "Imaging performance of a prototype scanned-slit digital mammography system." Proc. of SPIE Vol. 1896, 93-103, Medical Imaging, 1993.

[61] G. M. Besson, A. Koch, M. Tesic, R. Sottoriva, P. Prieur-Drevron, B. Munier, E. Calais, P. DeGroot, "Design and Evaluation of a Slot-Scanning Full-Field Digital Mammography System", Proc. Of SPIE Vol. 4682, 457-468, Medical Imaging, 2002.

[62] D. J. Curtis, R. J. Ayella, J. Whitley, R. P. Moser, K. S. Rugh, "Digital Radiology in Trauma Using Small-Dose Exposure." Radiology 132:587-591, 1979.

[63] E. Samei, J. Y. Lo, T. T. Yoshizumi, J. L. Jesneck, J. T. Dobbins III, C. E. Floyd, H. P. McAdams, C. E. Ravin, "Comparitive Scatter and Dose Performance of Slot-Scan and Full-Field Digital Chest Radiography systems." Radiology to be published 2005.

[64] W. J. H. Veldkamp, L. J. M. Kroft, B. J. A. Mertens, J. Geleijns, "Digital Slot-Scan Charge-coupled Device Radiography versus AMBER and Bucky Screen-Film Radiography: Comparison of Image Quality in a Phantom Study." Radiology to be published 2005.

[65] J. M. Boone, J. A. Seibert, C-M. Tang, S. M. Lane, "Grid and Slit Scan Scatter Reduction in Mammography: Comparison by using Monte Carlo Techniques." Radiology 222:519-527, 2002.

[66] J. H. Potgieter, M. de Villiers , M. Scheelke, G. de Jager, "An explanation for the extremely low, but variable radiation dosages measured in a linear slit scanning radiography system." Proc. of SPIE, Medical Imaging, 1138-1145, 2005.

[67] J. M. Boone, J. Anthony Seibert, "An accurate method for computer-generating tungsten anode x-ray spectra from 30 to 140 kV." Medical Physics 24 (11), 1661-1670, Novemeber 1997.

[68] J. M. Boone, "Chapter1: "X-ray Production, Interaction and Detection in Diagnostic Imaging." from The Handbook of Medical Imaging, Volume 1. Physics and Psychophysics, Editors J Beutel, H. L. Kundel, R. L. Van Metter, SPIE Press, 2000.

[69] M.J. Berger, J.H. Hubbell, S.M. Seltzer, J. S. Coursey, and D. S. Zucker, "XCOM: Photon Cross Sections Database." Institute of Standards and Technology, Physics Laboratory, Ionizing Radiation Division, http://physics.nist.gov/PhysRefData/Xcom/Text/XCOM.html.

[70] E. Pearce, "Focal spot intensity distribution for the Lodox GS-20711 tube unit." Varian systems Engineering documentation, 2004.

[71] M . Sandborg, D. R. Dance, J. Persliden, G. A. Carlsson "A Monte Carlo program for the calculation of contrast, noise and absorbed dose in diagnostic radiology." Computer Methods and Programs in Biomedicine Vol. 42, 167-180, 1994.

[72] J. F. Carrier, L. Atchambault, L. Beaulieu, R. Roy, "Validation of GEANT4, an object-oriented Monte Carlo toolkit, for simulations in medical physics." Medical Physics 31 (3), 484-492, 2004.

[73] S. Agostinelli et al. "Geant4 – a simulation toolkit." Nuclear Instruments and Methods in Physics Research A 506:250-303, 2003.

[74] J. M. Boone, J. A. Seibert, "Monte Carlo simulation of the scattered radiation distribution in diagnostic radiology." Medical Physics 15 (5), 713-720, 1998.

[75] H-P. Chan, K. Doi, "Physical characteristics of scattered radiation in diagnostic radiology: Monte Carlo simulation studies." Medical Physics 12 (2), 152-165, 1985.

[76] G. Barnea, C. E. Dick, "Monte Carlo studies of x-ray scattering in transmission diagnostic radiology." Medical Physics 13 (4), 490-495, 1986.

[77] R. K. Swank, "Absorption and noise in x-ray phosphors." Journal of Applied Physics, Vol. 44, No. 9, 4199-4203, September 1973.

[78] M . Sandborg, G. A. Carlsson, "Influence of x-ray energy spectrum, contrasting detail and detector on the signal-to-noise ratio (SNR) and detective quantum efficiency (DQE) in projetion radiography." Physics in Medicine and Biology, Vol. 37, No.6, 1245-1263, 1992.

[79] A. Ginzburg, C. E. Dick, "Image Information transfer properties of x-ray intensifying screens in the energy range from 17 to 320 keV." Medical Physics. 20:1013-1021, 1993.

[80] J. A. Rowlands, "Chapter 4: Flat Panel detectors for Digital Radiography" from The Handbook of Medical Imaging, Volume 1. Physics and Psychophysics, Editors J Beutel, H. L. Kundel, R. L. Van Metter, SPIE Press, 2000.

[81] R. K. Swank, "Calculation of Modulation Transfer Functions of X-Ray Flourescent Screens." Applied Optics Vol. 12, N0 8, 1865-1870, August 1973.

[82] Kasei Optonix supplied data, "http://www.kasei-optonix.co.jp/english/f-pro.htm".

[83] J. G. MainPrize, M. J. Yaffe, "The Effect of Phosphor Persistence on Image Quality in Digital X-Ray Scanning Systems." Proc. of SPIE Vol. 2708, Medical Imaging,85-93, 1996.

[84] D. Okkalides, "Evaluation of afterglow response in irradiated intensifying screens." Physics in Medicine and Biology (41), 2173-2178, 1986.

[85] D. J. Krus, W. P. Novak, L. Perna, "Precision linear and two-dimensional scintillation crystal arrays for x-ray and gamma ray imaging applications." Proc. of SPIE Vol. 3768, Hard X-ray, Gamma-Ray and Neutron Detector Physics, 1999.

[86] S. Hejazi, D. P. Trauernicht, "System considerations in CCD-based x-ray imaging for digital chest radiography and digital mammography." Medical Physics 24:287-297, 1996.

[87] W. Zhao, G. Ristic, J. A. Rowlands, "X-ray imaging performance of structured cesium iodide screens." Medical Physics 31 (9), 2594-2605, 2004.

Appendix A – Focal spot intensity distribution

FOCAL SPOT INTENSITY DISTRIBUTION
for the
LODOX GS-20711 & GS-30711
TUBE UNITS

May 21, 2004
by
Eric Pearce
Mid-Tier Engineer
In response to CR 1912

PURPOSE

This report presents the data concerning the normalized intensity of the Lodox GS-20711 and the GS-30711 focal spots. The primary assumption this report makes is that both the GS-20711 and the GS-30711 have the same basic intensity and therefore only the data from GS-30711 will be presented. This information has been requested from Lodox.

PROCEDURE

Data has been gathered according to the following procedure. Focal spots from standard pinhole were aquired for the GS-30711 tube unit with a serial number of 97698-4P. This tube unit was supplied to Lodox in the March/April 2004 timeframe.

The focal spots were scanned into digital format and ran through algorithms that analyzed the spot data. The analysis consisted of a filtering algorithm that removed some of the image noise, then generated plots to illustrate the intensity distributions of the spot.

RESULTS

The attached data represents the following.

Figure 1 & **Figure 5** - Images of GS-30711 Large & Small Focal Spots, respectively, that were analyzed.

Figure 2 & **Figure 6** - Contour maps of the intensity for the GS-30711 Large & Small Focal Spots. The in both figures, width is seen along the x-axis and the length is seen along the y-axis.

Figure 3 & **Figure 7** - Plots of the Line Spread Functions for the GS-30711 Large & Small, respectively, Focal Spots. In both graphs, the width and the length are represented, as indicated.

Figure 4 & **Figure 8** - Plots of the Relative Intensity for the GS-30711 Large & Small Focal Spots, respectively. Also, the Fourier Transform of the Relative Intensity curves is displayed in each graph.

CONCLUSIONS

The data presented here are representative of both the GS-20711 and the GS-30711 focal spot intensities. Additional information, should it be needed, will be made available upon request.

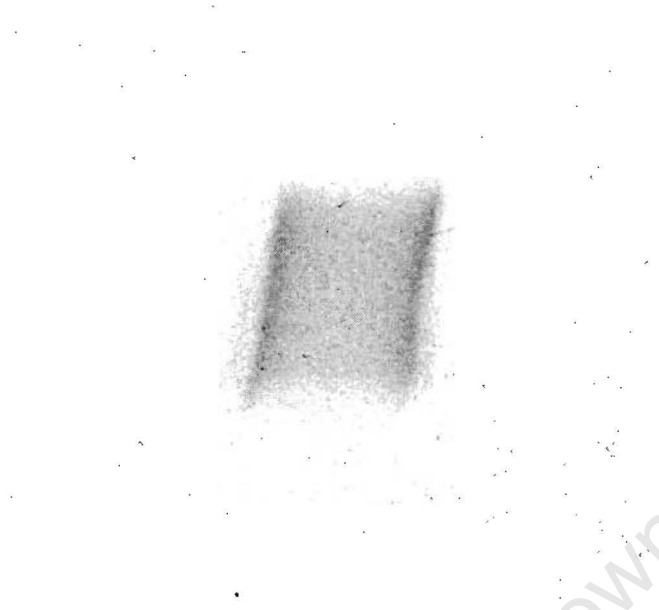

Figure 1- Image of GS-30711 Large Focal Spot that was analyzed.

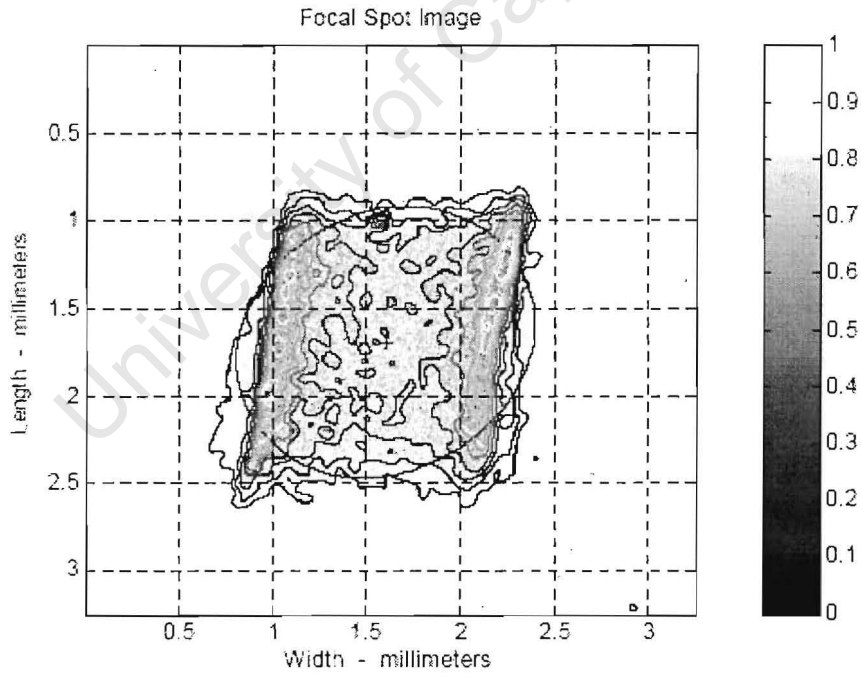

Figure 2- Contour map of the intensity for the GS-30711 Large Focal Spot. The width is seen along the x-axis. The length is seen along the y-axis.

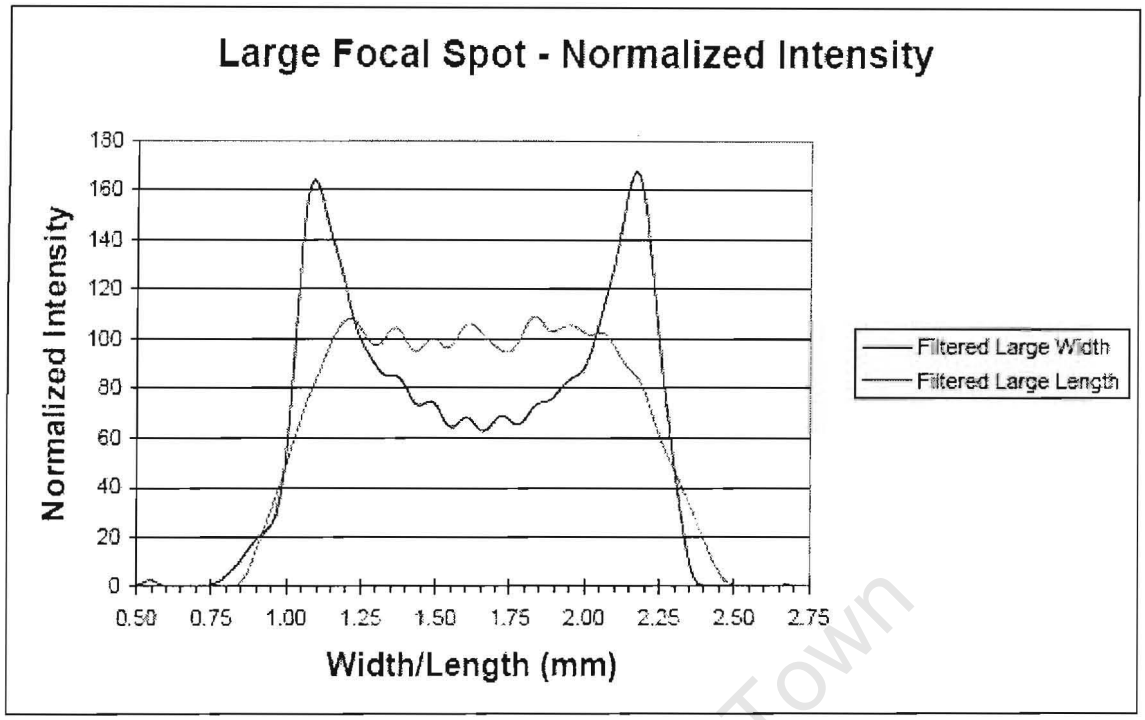

Figure 3- Plot of the Line Spread Functions for the GS-30711 Large Focal Spot. Both the width and the length are represented.

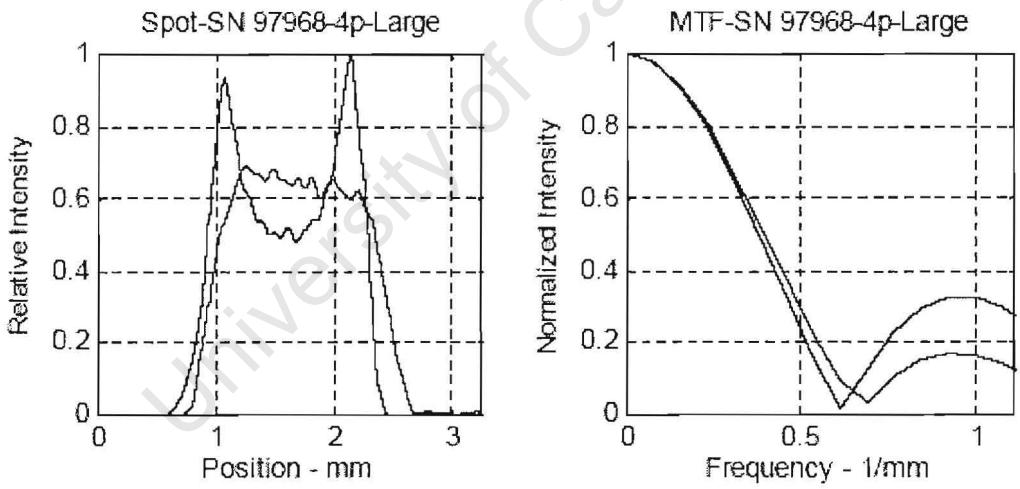

Figure 4- Plot of the Relative Intensity for the GS-30711 Large Focal Spot. Also, the Fourier Transform of the Relative Intensity curves is displayed.

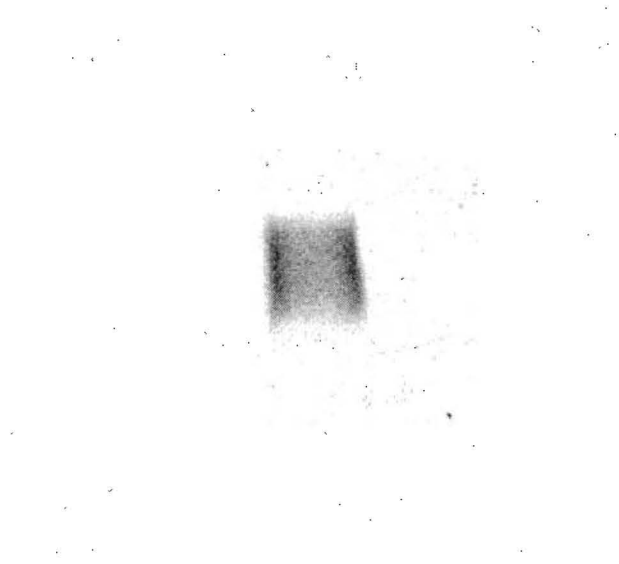

Figure 5- Image of GS-30711 Small Focal Spot that was analyzed.

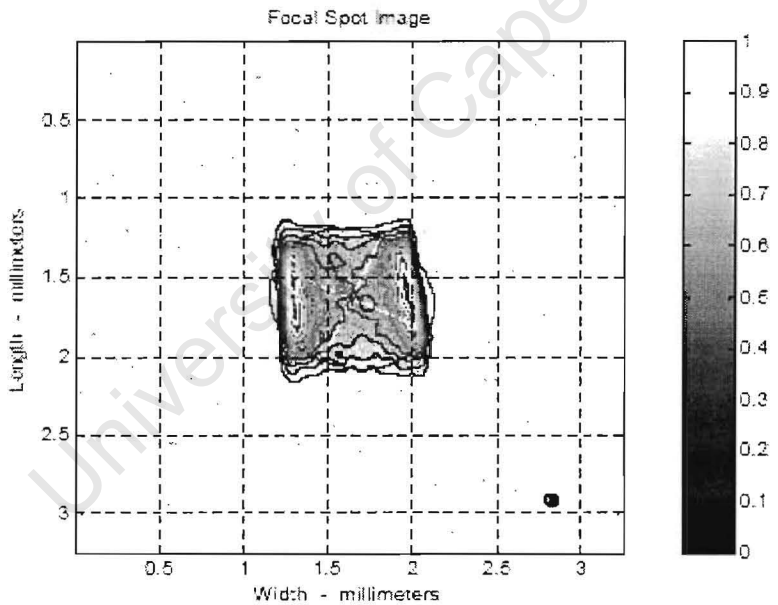

Figure 6- Contour map of the intensity for the GS-30711 Small Focal Spot. The width is seen along the x-axis. The length is seen along the y-axis.

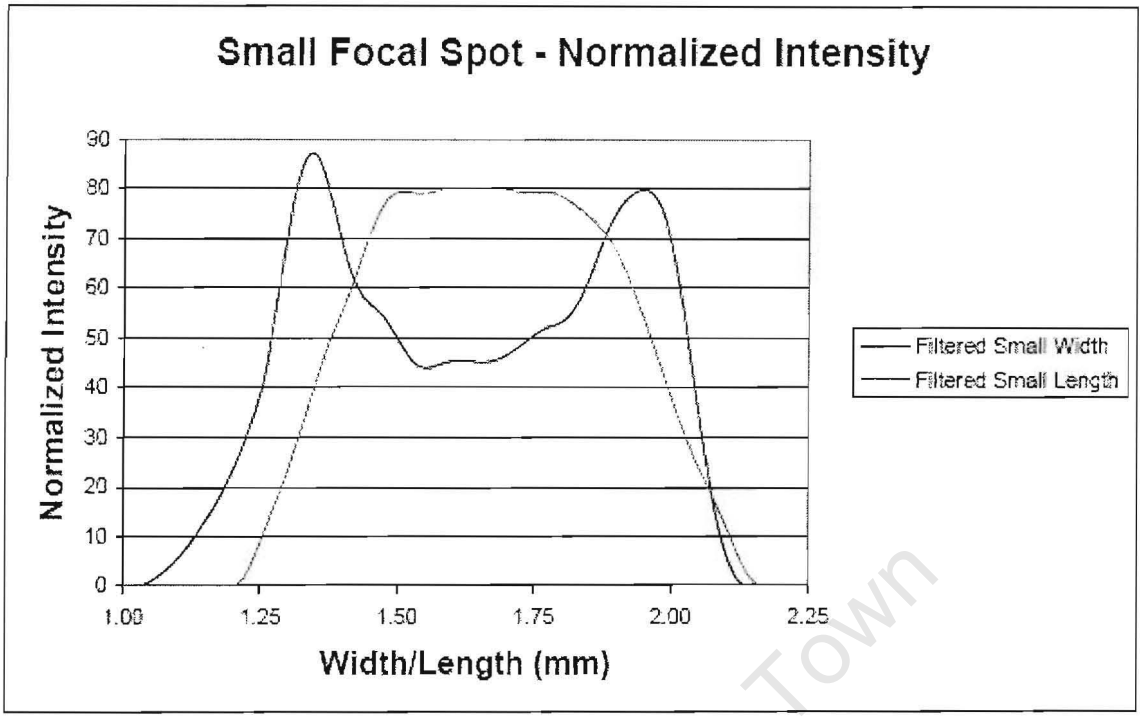

Figure 7- Plot of the Line Spread Functions for the GS-30711 Small Focal Spot. Both the width and the length are represented.

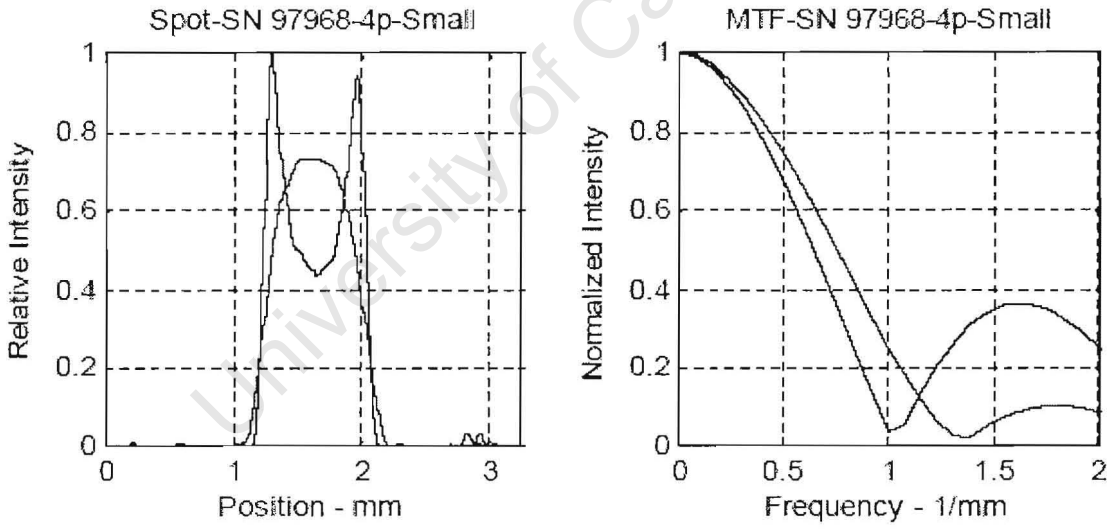

Figure 8- Plot of the Relative Intensity for the GS-30711 Small Focal Spot. Also, the Fourier Transform of the Relative Intensity curves is displayed.

Appendix B – FOT demagnification spatial distribution

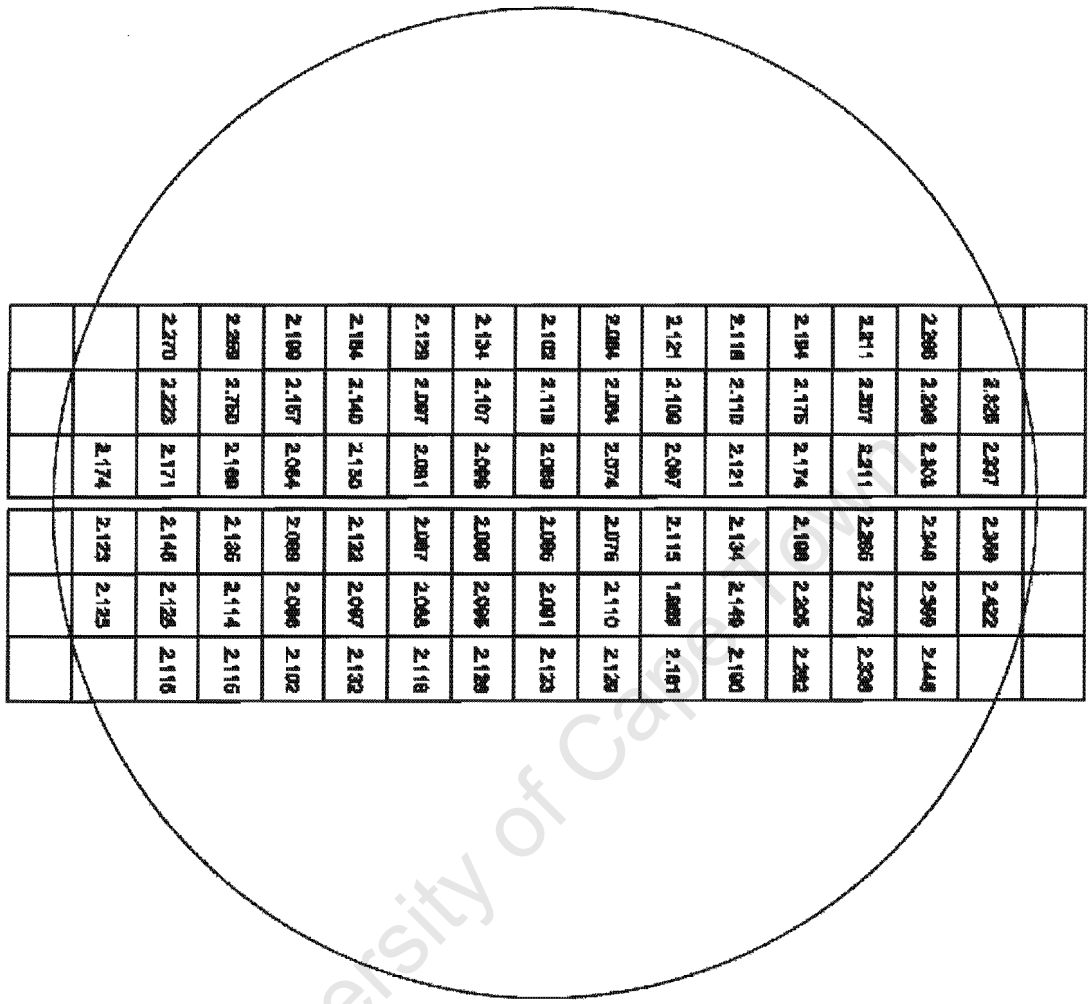

Figure B-1 Spatial distribution of demagnification in a FOT used in the Statscan detector - from measurements taken by Incom Engineers

Appendix C – GEANT4 Monte Carlo simulation

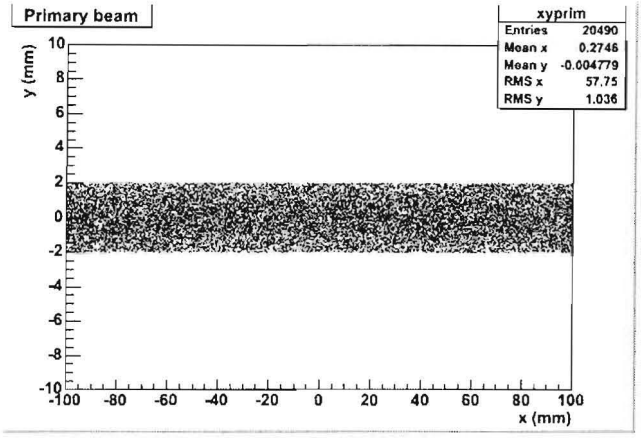

Figure B-1 Spatial distribution of primary photons incident on detector. Simulation with small focal spot (uniform distribution), 0.5 mm collimator width and 20 cm deep water phantom. Peak voltage of TASMIP generated spectrum set to 140 kV.

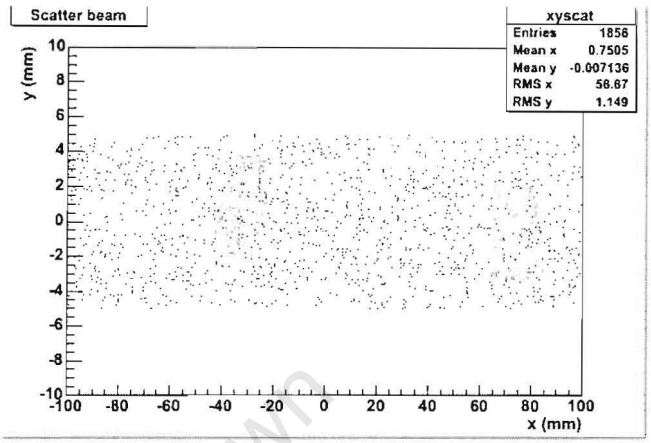

Figure B-2 Spatial distribution of scattered photons incident on detector (data only displayed for a 8 mm wide strip). Simulation with small focal spot (uniform distribution), 0.5 mm collimator width and 20 cm deep water phantom. Peak voltage of TASMIP generated spectrum set to 140 kV.

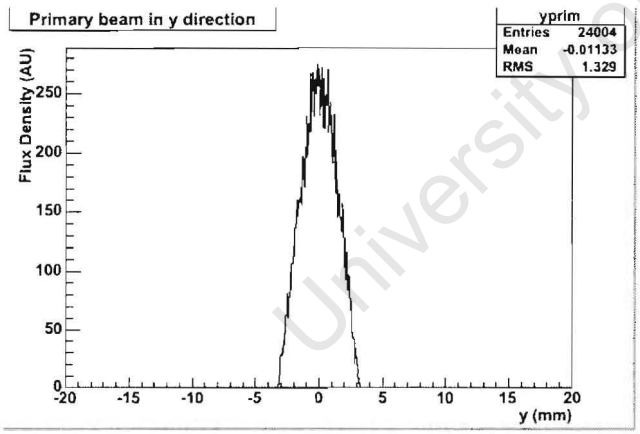

Figure B-3 Scan direction cross section of spatial distribution of primary photons incident on detector. Simulation with small focal spot (uniform distribution), 0.5 mm collimator width and 20 cm deep water phantom. Peak voltage of TASMIP generated spectrum set to 140 kV.

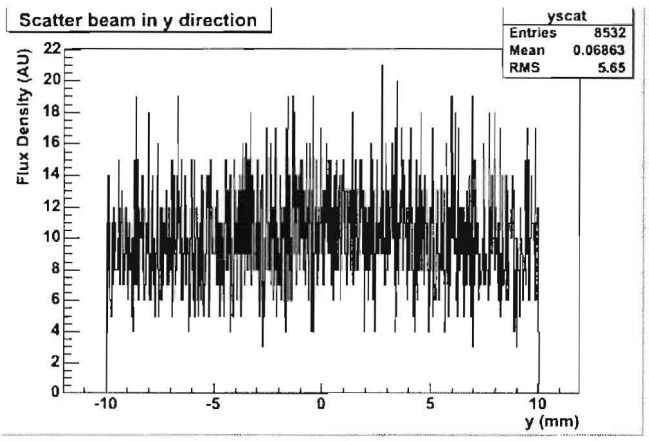

Figure B-4 Cross section of spatial distribution of scattered photons incident on detector. Simulation with small focal spot (uniform distribution), 0.5 mm collimator width and 20 cm deep water phantom. Peak voltage of TASMIP generated spectrum set to 140 kV.

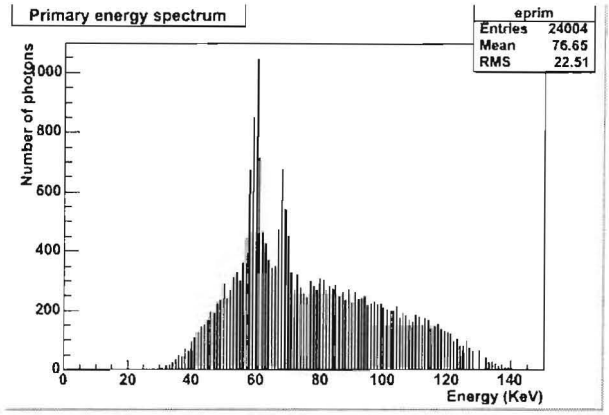

Figure B-5 Energy distribution of primary photons incident on detector. Simulation with small focal spot, 0.5 mm collimator width and 20 cm deep water phantom. Peak voltage of TASMIP generated spectrum set to 140 kV.

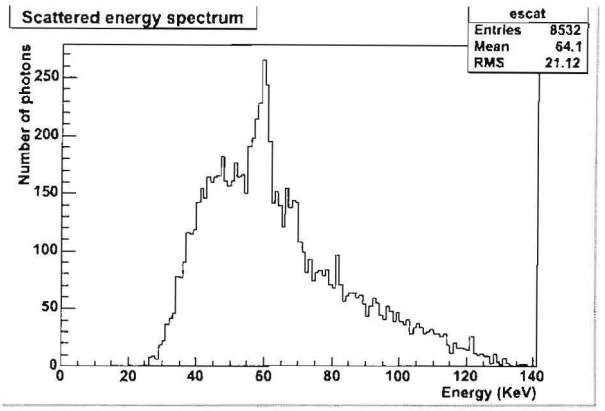

Figure B-6 Energy distribution of scattered photons incident on detector. Simulation with small focal spot, 0.5 mm collimator width and 20 cm deep water phantom. Peak voltage of TASMIP generated spectrum set to 140 kV.

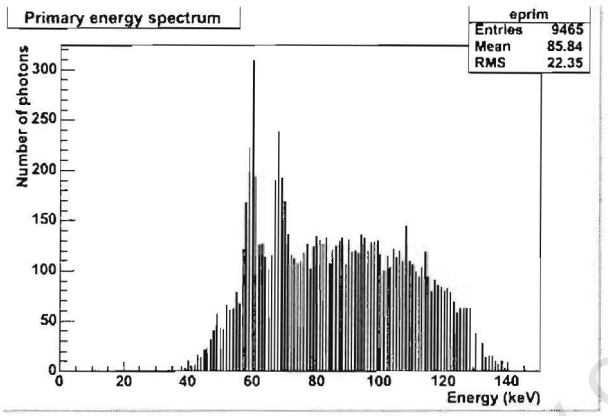

Figure B-7 Energy distribution of primary photons incident on detector. Simulation with small focal spot, 0.5 mm collimator width and 40 cm deep water phantom. Peak voltage of TASMIP generated spectrum set to 140 kV.

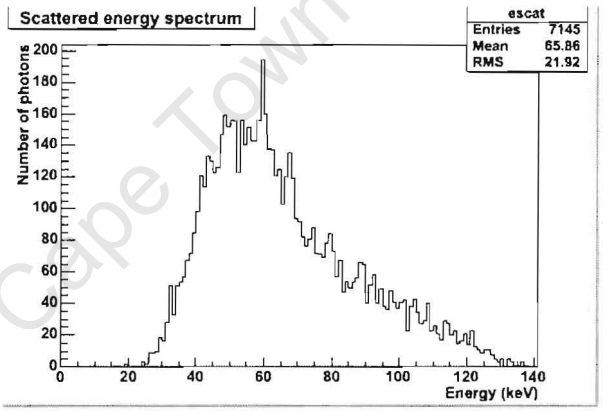

Figure B-8 Energy distribution of scattered photons incident on detector. Simulation with small focal spot, 0.5 mm collimator width and 40 cm deep water phantom. Peak voltage of TASMIP generated spectrum set to 140 kV.

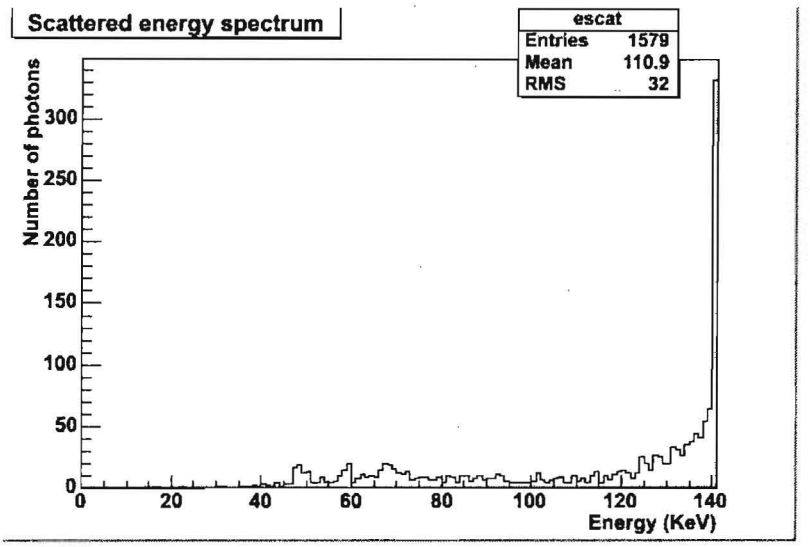

Figure B-9 Energy distribution of scattered photons incident on detector for a monoergetic 140 kV generated beam. Peak at 140 keV is as a result of singly Rayleigh (Coherent) scattered photons.

Appendix D – Paper published in the Proceedings of SPIE

Proceedings of SPIE, Medical Imaging 2005, Vol. 5745 (Edited by M.J. Flynn), 1179-1190.

System characterization of the STATSCAN full body slit scanning radiography machine: Theory and experiment.

Martin Scheelke*[a], J. Herman Potgieter[b], Mattieu de Villiers[b]
[a]MRC/UCT Medical Imaging Unit, Cape Town, South Africa
[b]Lodox Systems (Pty) Ltd, Box 651807, Benmore, 2010. South Africa.

ABSTRACT

This report presents a system model of the STATSCAN slit scanning full body radiography machine. A Cascaded Linear Systems model of the detector was developed and the theoretical DQE, MTF and NPS were compared to measured values for the RQA9 beam quality described in IEC 62220-1. The effect on detector DQE of various system parameters such as coupling efficiency, CCD noise and pixel binning was quantified. System performance for various thicknesses of Gd_2O_2S:Tb was analyzed. The notion of a "System DQE" has been suggested by several authors to facilitate the comparison of overall systems. An expression for the overall "System DQE" was developed by including the effects of scattered radiation, grid attenuation and focal spot unsharpness in the cascaded model. Scattered radiation was quantified as a function of system geometry parameters and was treated as an "additive noise stage". A realistic model of the focal spot was used to calculate the MTF due to beam divergence in the scan direction and focal spot unsharpness in the slit direction. It was found that the "System DQE" is a valuable parameter for the purpose of comparing gridless slit scanning system performance to conventional geometry system performance.

Keywords: DQE, MTF, NPS, System DQE, SDQE, image quality, slit scanning, full body, system optimization.

1. INTRODUCTION

The **Statscan**™ full body x-ray machine is a commercially available digital radiography system that has recently been approved by the Food and Drug Administration and CE marked. The system utilizes a gridless linear slit scanning geometry in which a narrow fan beam is scanned linearly over the object in synchronism with a linear detector array. The slit scanning principle is a well known method[1, 2, 3] to drastically reduce the scatter to primary ratio (SPR) without using a grid. The result is an increased signal to noise ratio (SNR) for a given dose. Entrance doses measured during typical imaging procedures (Skull, Spine, Abdomen, Full Body) for the STATSCAN system are approximately 10 percent of corresponding entrance doses for a conventional geometry (wide beam) system[4, 5] for equivalent image quality. However for lung imaging the slit scanning dose reduction is less marked (at 70 percent) since the low lung density results in a conventional geometry system having a proportionally lower SPR. A further advantage of the linear slit scanning technique is a larger image area (selectable up to 1.8 m x 0.68 m in the case of STATSCAN) for a given detector size and cost. Figure 1 shows an example of a full body image of an obese poly-trauma patient taken with the STATSCAN imaging system.

A commonly reported concern[1] with slit scanning is that the low flux usage efficiency results in tube heat loading placing a practical upper limit on image size, quality and duty cycle. This problem has been overcome due to the availability of tubes with greater heat loading capacity, increases in detector sensitivity and optimization of the slit width for a given imaging task.

The detector DQE has been measured for an earlier version of the STATSCAN system[6]. Since that study, detector noise and coupling efficiency have been improved and this report presents new NNPS, MTF and DQE measurements for various screens and detector configurations. Furthermore, an expression was developed for these image quality metrics using cascaded linear systems analysis[7]. The first purpose of this study is to give a comparison and analysis of the

* Corresponding author: scheelkm@cormack.uct.ac.za; phone +27 72 081 1179; fax +27 11 262 0085.

Figure 1. STATSCAN image of obese poly-trauma patient with tension pneumothorax and fracture of the ribs and pelvis. Vertical stripes due to stretcher.

predicted and measured detector MTF and DQE.

Although the detector DQE is a commonly used metric[8] for the rating of x-ray detectors, it does not include system level effects such as scatter, grid attenuation and focal spot geometric blurring. At the present time no standard method is available for comparing the imaging efficiency of entire x-ray systems. A metric for imaging system evaluation that includes system level effects has been suggested and variably named the "System DQE"[9], "Generalized DQE"[10] or "Effective DQE"[3] – in this study the metric is referred to as "System DQE" or SDQE. The second purpose of this study is to present an extended cascaded linear systems model that includes system level effects and to analyze the effect of various system parameter values on the SDQE. Of specific interest is to use the SDQE concept to compare two systems with identical detectors but different geometries: slit scanning geometry or conventional geometry.

1.1. Principle of operation

A narrow and vertical fan beam 3-6 mm in width and 700 mm long (at detector) is scanned linearly over the patient and detected by a radiographic screen of similar shape as the fan beam. The beam shape is set by two slits or "collimators" as shown in Figure 2. A post-collimator at the detector removes any scattered radiation outside of the primary main beam area. The entire primary beam is detected – no radiation is "lost" outside the sensitive area of the detector. The source and detector are mounted on a C-arm (see Figure 3) that can rotate up to 90 degrees – allowing lateral scans to be taken without repositioning of the patient. Three scans speeds can be selected: 35, 70 and 140 mm/s.

The detector consists of a screen (Gd_2O_2S:Tb, 130 mg/cm^2) optically coupled by fiber optic taper (FOT) to twelve scientific grade CCD's operated in TDI mode. The CCD pixel pitch is 27 μm and the basic image pixel pitch is 60 μm due to the FOT demagnification of 2.3. For each image acquisition, pixels can be binned at the CCD line register level to allow selection of an image pixel pitch of for example 60, 120 ,240, 360 or 480 μm. The FOT butts are arranged diagonally so that neighbouring CCD's receive overlapping data. This allows an "unbutting" software algorithm to completely remove butting artifacts.

Multiplicative structured noise due to spatial variation of sensitivity in the screen, FOT and CCD are compensated for by a gain and offset correction algorithm similar to that described by Samei[11]. The structured noise is less pronounced in the scan direction due to the TDI integration. In slit scanning systems, tube output fluctuations and scan speed variations introduce banding in the scan direction. These effects are lessened by designing the C-arm to dampen anode vibration and the linear drive induction motor was chosen to allow a high degree of scan speed accuracy. The TDI integration effect serves to further lessen image banding in the scan direction.

The x-ray tube is mounted with the plane of the rotating anode in the slit direction. As a result, the Heel effect occurs in the scan direction and is of no consequence as the slit is open only to a very narrow portion of the beam.

Image post-processing includes log compensation, dynamic range compression, geometric distortion correction, camera overlap unbutting and various noise reduction and filtering algorithms.

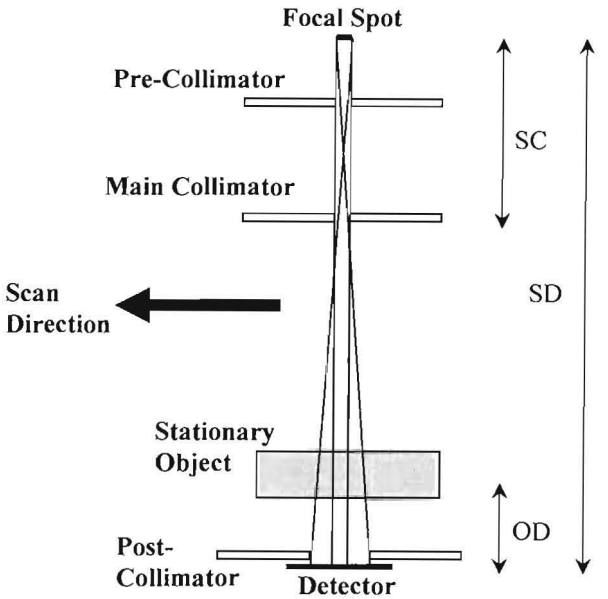

Figure 2. Illustration of linear slit scanning principle. The source, detector and collimator seen from the side here are scanned across the object. The narrow fan beam is detected by a screen and projected by fiber optic taper onto a linear array of CCD sensors operating in TDI mode.

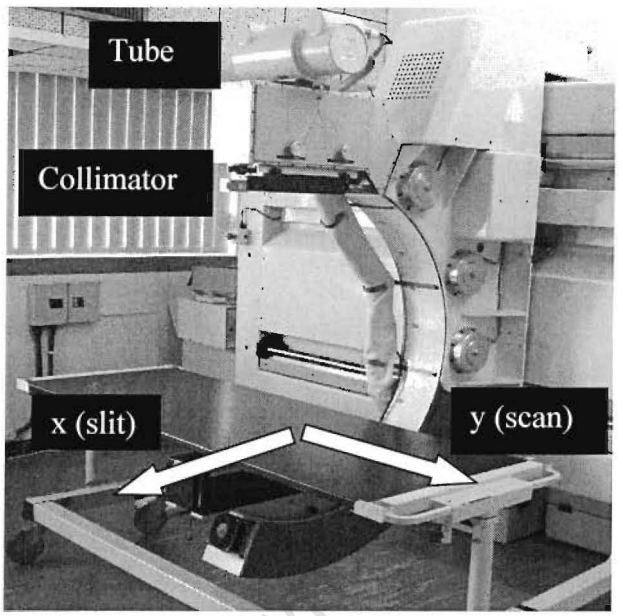

Figure 3. Experimental version of the STATSCAN full body x-ray machine showing the reference axes used in this study.

2. THEORY

2.1. Theoretical DQE, NNPS, MTF and "System DQE"

Cascaded linear systems modeling[7] of detectors in radiography is a well established method for analyzing detector performance in terms of physical parameters. Investigators[12, 13] have used the method to predict detector DQE, and MTF to a high degree of accuracy. Cascaded linear systems analysis relies heavily on frequency domain analysis and requires that the system be linear, shift invariant, ergodic, and should have wide sense cyclo- stationary noise properties. The system is assumed to approximately meet the last two requirements and has been shown to be approximately linear and shift invariant[6].

A cascaded model of the system was developed that includes stages identified in the detector as well as system level effects[10, 13] such as focal spot blurring, grid attenuation and scattered radiation incident. Table 1. shows the stages and parameters used in the cascaded linear model. The inclusion of stages before absorption in the screen is something of a departure from traditional cascaded linear models. An attempt was made to select stages that have the largest effect on system image quality metrics. Error introduced due to omission of certain minor stages is discussed in section 4.

Table 1. System atages of the linear cascaded model. System level effects are included.

Parameter	Description	Stage type
T_1	Geometric blurring	Quantum scatter
$\bar{g}_2$	Grid Attenuation	Binary selection
$\bar{s}_3$	Scattered fluence	Additive noise
$\bar{g}_4$	Screen absorption efficiency	Binary selection
$\bar{g}_5, \varepsilon_5$	Screen conversion gain	Quantum gain
T_6	Screen MTF	Quantum scatter
T_7	Scan direction smear due to phosphor persistence	Quantum scatter
$\bar{g}_8$	Coupling efficiency	Binary selection
T_9	Pixel aperture blur	Deterministic blur
S_{10}	CCD and electronic	Additive noise

The component MTF's can be combined multiplicatively so the System MTF (SMTF) in the slit direction can be written as

$$SMTF(f_x) = T_1(f_x)T_6(f_x)T_9(f_x) \tag{1}$$

and as

$$SMTF(f_y) = T_1(f_y)T_6(f_y)T_7(f_y)T_9(f_y) \tag{2}$$

in the scan direction.
f_y and f_x are the one dimensional spatial frequency variables in the scan and slit direction respectively. The detector MTF is found by setting the geometric blur term T_1 to unity in equations 1. and 2.

In a similar fashion to the analysis of Siewerdsen et al.[13], it is assumed that the difference in spectral distribution between the primary and scattered radiation fields is small. As a consequence both the scatter and primary fluence distributions are transferred identically through the system from absorption in the screen onwards. Based on that and on cascaded systems transfer theory, an expression for System DQE in the scan direction was derived as

$$SDQE(f_y) = \frac{\bar{g}_2\bar{g}_4\bar{g}_5\bar{g}_8 T_1(f_y)^2 T_6(f_y)^2 T_7(f_y)^2 T_9(f_y)^2}{(1+\frac{\bar{s}_3}{q_o\bar{g}_2})\left[1+\bar{g}_8(\varepsilon_5+\bar{g}_5)T_6(f_y)^2\right]\times T_9(f_y)^2 + \frac{S_{10}}{a^4 q_o \bar{g}_4\bar{g}_5\bar{g}_2\bar{g}_8}}, \tag{3}$$

where a is the binned pixel aperture width.

The System DQE in the slit direction $SDQE(f_x)$ has the same form as $SDQE(f_y)$ except that the image smear term $T_7(f_y)$ is omitted.
The geometric blur term T_1 is radialy asymmetric and is a second cause of differences between the scan and slit direction SDQE. In the slit direction $T_1(f_x)$ is similar to focal spot blur and in the scan direction $T_1(f_y)$ is related to beam divergence. A detailed geometry dependent expression for T_1 in the scan and slit direction has been developed, but is beyond the scope of this study.
The detector DQE is found by setting T_1 and g_2 to unity and S_3 to zero in equation 3. This is equivalent to the case with ideal scatter suppression, no grid and no focal spot blurring effects. Hence, one can by inspection of equation 3. see that for the quantum limited case ($S_{10} = 0$), the following relationship between the system DQE and detector DQE holds:

$$SDQE(f) = \frac{\bar{g}_2 T_1(f)^2\, DQE(f)}{(1+SPR)} \tag{4}$$

where $SPR = \bar{s}_3 / q_o\bar{g}_2$ is the scatter to primary ratio of the radiation incident on the detector. This result is consistent with the findings of other investigators[3, 10, 13].
Magnification effects were ignored (the SDQE is referred to the detector plane) in this study since the magnification in the scan direction is unity for linear slit scanning and the magnification in the slot direction is small in this case. Also, effects of signal and noise aliasing were ignored[17].

3. METHOD

The detector MTF, NPS and DQE were measured for five different screen types (Rarex Fast Back 130 mg/cm^2 and Medium 50 mg/cm^2 from MCIO; DRZ-Plus 100 mg/cm^2, DRZ-High 145 mg/cm^2 and PI-200 mg/cm^2 from Kasei-Optonix) at RQA9 with various detector configurations, and exposure levels. Corresponding theoretical values were calculated. The measurement method used is outlined in the IEC 62220-1 standard[8], is described in detail in the literature[14, 15, 16] and has been used in practice by other investigators[11, 14].

The method outlined in IEC 62220-1 does not apply directly to linear slit scanning systems, but a simple modification to the dose calculation method makes it applicable to this purpose[6]. In linear slit scanning, the exposure area increases proportional to the distance from the source rather than with the square of the distance as with conventional geometry systems[5]. Therefore, the dose correction for ionization chamber to detector distance follows a 1/r law rather than a $1/r^2$ law. This fact is unique to *linear* slit scanning systems (the exposure area of radial slit scanning systems with a stationary tube increases by the square of the distance from the source).

3.1. Acquisition conditions

Flat field images for the analysis of NPS and MTF were acquired at four exposure levels for screen type and detector configuration. The additional thickness of aluminium required for each beam quality defined in IEC 62220-1 was placed behind the collimator to minimize scatter. For the MTF measurement, a tungsten plate was placed in the beam. Log compensation was turned off so that pixel values were proportional to the charge accumulated in the CCD line register during scans. Camera unbutting, flat-field gain correction and offset correction were turned on. The beam was collimated to expose only the four central cameras of the detector and the resulting images were about 2000 x 2000 pixels in size (for 2x2 binning). Figure 4 illustrates the setup.

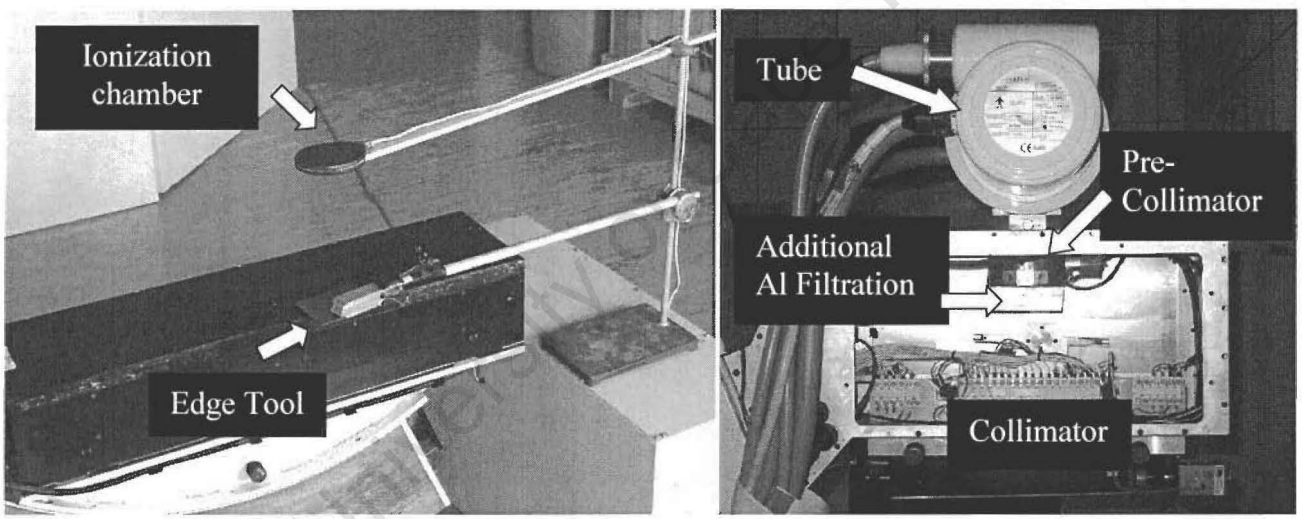

Figure 4. Acquisition conditions for dose, NNPS and MTF measurement. The IEC 62220-1 defined patient equivalent thickness of Aluminium was placed behind the main collimator in order to minimize detected scatter.

3.2. Dose measurement

A relatively large (60 cm^3) dosimeter chamber (Radcal 10X5-60E with Radcal 9010 dosimeter) was used to retain sensitivity at the low dose levels typical of the machine under study. The ionization chamber was placed about 300 mm from the detector to minimize backscatter effects. For each scan, the flux density q_o was calculated at the detector plane using the method described in IEC 62220-01 and at the beginning of Section 3.

3.3. Detector MTF

The MTF was measured using the angled edge method as described in Samei et al.[16] and de Villiers et al.[6]. Images of a milled rectangular tungsten plate which had edges angled at approximately 2 degrees from the scan and slit direction

were obtained. The edge position and angle was identified using a Nelder-Mead optimization algorithm[6] which maximizes the mean signal level difference on either side of the edge. An over-sampled edge spread function (ESF) was then obtained by binning pixel values projected parallel to the edge onto an orthogonal line. The line spread function (LSF) was found by differentiating the ESF using a numerical difference method and the pre-sampled MTF (MTF_{pre}) was obtained as the Fourier transform of the LSF.
The tungsten plate was placed as close as possible to the detector – about 7 mm from the screen due to limitations imposed by the detector housing. The effect of the distance between plate and screen on the measured MTF is discussed in the results and discussions section. Care was taken to make sure the plate was as level as possible.

3.4. NNPS

Several partially overlapped 128x128 regions of interest (ROI's) from the central 1000x1000 area of each flat image were used for the calculation of the Noise Power Spectrum. The two dimensional NPS was calculated as the mean of the squared Fast Fourier Transform of each ROI's. The result was then normalized by the overall mean value of the ROI's to yield the two dimensional Normalised Noise Power Spectrum (NNPS). One dimensional cuts in each orthogonal axis direction were obtained by averaging the central 7 lines (excluding the axis). The frequency values were transformed to the central axis scale by applying $f_x = \sqrt{f_x^2 + f_y^2}$ in the scan direction and $f_y = \sqrt{f_y^2 + f_x^2}$ in the slit direction.
No flat field or offset correction was applied as these corrections are built into the system software and were not turned off under image acquisition.
A point of interest is that in initial experiments, an offset added in software went unnoticed and had the effect of reducing the NNPS. This in turn caused overestimation of the DQE especially at low exposures. This offset error was subsequently corrected.

3.5. Detector DQE

The detector Detective Quantum Efficiency was calculated from the above results as

$$DQE(f) = \frac{MTF_{pre}^{\ 2}(f)}{NNPS(f)\bar{q}_o}. \qquad (5)$$

3.6. Calculation of system parameters

The SPR for the STATSCAN system at the detector and hence s_3 was calculated by a simple GEANT4[18, 19] Monte Carlo simulation for various slit widths and water phantoms of two different thickness (20cm and 40cm). A realistic system geometry and source energy spectrum[20] was used in the simulation with the following parameters: SD = 1300 mm, SC = 400 mm, focal spot width = 0.6 mm, kVp = 90 kV and air gap = 130 mm. Screen parameters were calculated as follows: The quantum absorption efficiency g_4 was calculated as the incident energy spectrum[20] weighted integral over the absorption coefficients[21] for Gd_2O_2S:Tb and CSI:Tl. The conversion gain and noise g_5 and e_5 were calculated from published values[22]. The screen MTF T_6 was modeled by a Lorenztian fit[12] (with fitting parameter H) to manufacturer (Kasei Optonix and MCIO) supplied data and data in the literature[23]. Image smear in the scan direction T_7 was modeled as a decaying exponential[24] with time constant τ = 850 ms. The coupling efficiency g_8 was calculated from the transmission efficiency[25] of the FOP and FOT and the matching of the screen output spectrum to the CCD quantum effieicncy[25]. The pixel apeture MTF T_9 was modeled as $T_9(f) = sinc(bmaf)$ for bxb binning (a is the pixel width on the CCD and m is taper demagnification). The additive noise S_{10} was calculated from the measured noise power spectrum of dark field images. S_{10} was referred to units of electrons at the CCD pixel by dividing by the square of the A/D converter gain and the CCD output gain.

4. RESULTS AND DISCUSSION

4.1. Detector results

Figure 5, 6 and 7 show the measured and predicted MTF, DQE and NNPS for Rarex 130 mg/cm^2 and 50 mg/cm^2. Detector parameter values for the two screens were calculated as $g_4 = 0.6$; $g_5 = 1390$; $e_5 = 510$; $H = 1.25$; $\tau = 850$ ms; $g8 = 0.015$; $a = 0.06$ mm; $b = 2$ for the former and $g_4 = 0.31$; $g_5 = 1200$; $e_5 = 420$; $H = 0.5$; $\tau = 850$ ms; $g_8 = 0.015$; $a = 0.06$ mm; $b = 2$ for the latter.

4.1.1. MTF discussion

Figure 5 shows that there is good agreement at lower spatial frequencies between theory and experiment, however the agreement is not as good at higher spatial frequencies. The predicted MTF is consistently higher than the measured quantity. The measured and predicted MTF in the scan direction is slightly inferior to the slit direction MTF – an expected effect of image smear. Image smear has a more pronounced effect in the case of the Rarex 50 mg/mm2 screen since τ remains constant but the remaining MTF components are better. Reasons for the differences between measured and predicted MTF values could be (1) The gap between the tungsten plate and detector (7 mm) introduces an error which reduces the measured MTF. (2) A possible misalignment between scan direction and TDI columns would reduce the measured MTF.[26] (3). The effect of charge transfer inefficiency reduces the measured MTF.[28] (4) A possible scan speed-charge transfer mismatch would also reduce the measured MTF.[27] (5) Backscatter from the tapers may cause a small degradation of the measured MTF.

4.1.2. NNPS discussion

Figure 6 shows good agreement at low spatial frequencies but less agreement is shown at higher spatial frequencies. This can be explained by the squared dependence of the predicted NNPS on the predicted MTF which is overestimated (see Section 4.1.1).

4.1.3. DQE discussion

In Figure 7 reasonable agreement is shown between the predicted and measured results, particularly in the case of the Rarex 50 mg/cm^2 screen. For both screens, greater exposure dependence is seen in the predicted results than in the measured results. This could be due to two possibilities (1) The gain correction algorithm does not completely remove

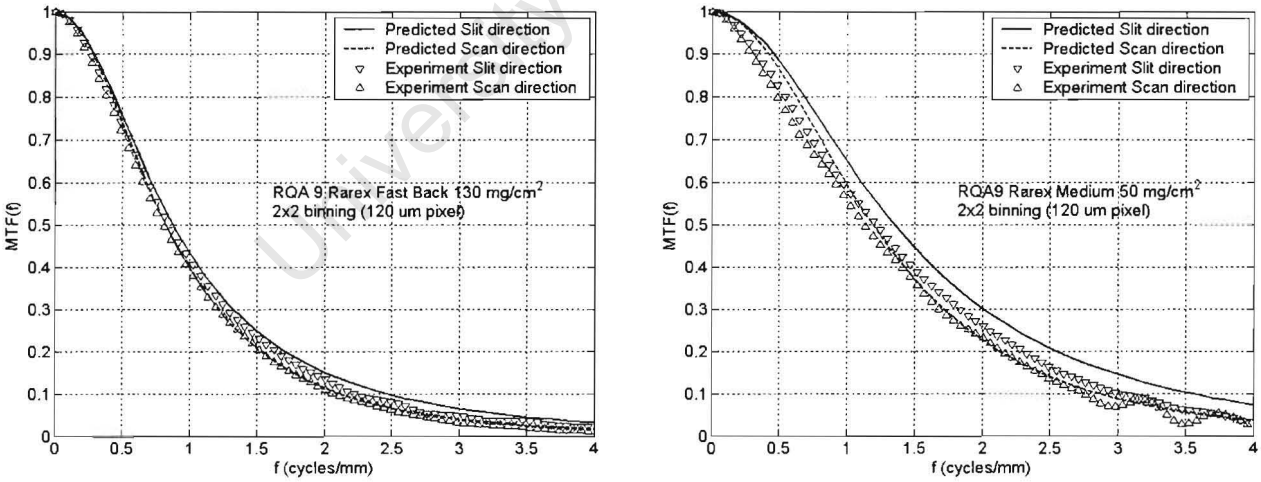

Figure 5. MTF for Rarex 130 mg/cm^2 and Rarex 50 mg/cm^2 at RQA9 – comparison of measured data and theoretical prediction. All measurements taken at half scan speed (70 mm/s). For clarity, the MTF is shown in the slit direction only.

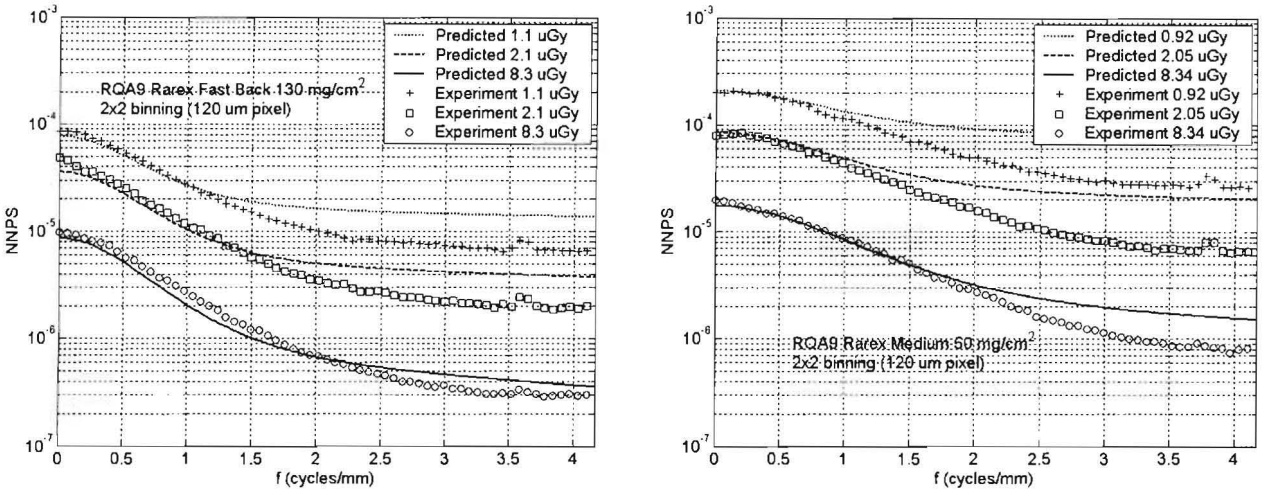

Figure 6. NNPS for Rarex 130 mg/cm^2 and Rarex 50 mg/cm^2 at RQA9 – comparison of measured data and theoretical prediction. All measurements taken at half scan speed (70 mm/s). For clarity, the NNPS is shown in the slit direction only.

multiplicative noise causing increased structured noise at higher exposures and hence a decrease in measured exposure dependence of the DQE. (2) The CCD and A/D converter gains were underestimated causing an overestimation of the additive noise S_{10}. Systemic differences between predicted and measured values at low frequency could be due to deviation of the screen mass thickness from the quoted value. Figure 8 shows a predicted and measured value comparison of the slit and scan direction DQE for the Rarex 130 mg/cm^2 screen. As predicted by theory the scan direction DQE is slightly inferior due to finite phosphor persistence image smear.

For the three remaining screens (PI-200, DRZ-High, DRZ-Plus), results showed similar exposure dependence and agreement between experiment and theory (results omitted for brevity). Similar differences in the slit and scan direction quantities were also found. A comparison of the slit direction MTF and DQE for the five screens used in this study is shown in Figure 9. The DQE results follow the expected trend of thicker screens having higher low frequecy DQE and lower high frequency DQE. The DRZ-100 mg/cm^2 screen seems to be an exception with a high frequency DQE higher

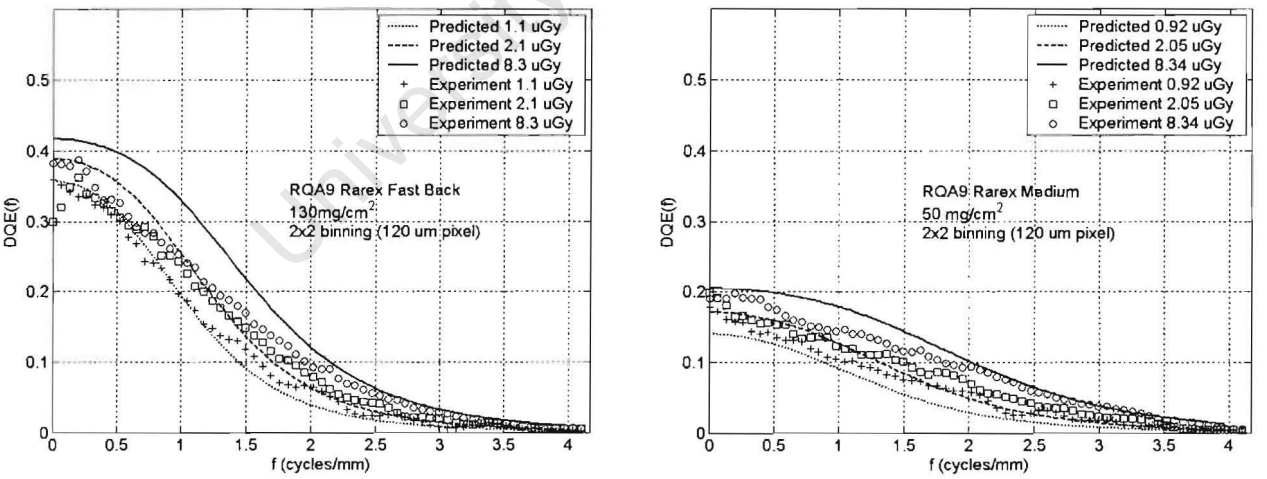

Figure 7. DQE for Rarex 130 mg/cm^2 and Rarex 50 mg/cm^2 at RQA9 – comparison of measured data and theoretical prediction. All measurements taken at half scan speed (70 mm/s). For clarity, the DQE is shown in the slit direction only.

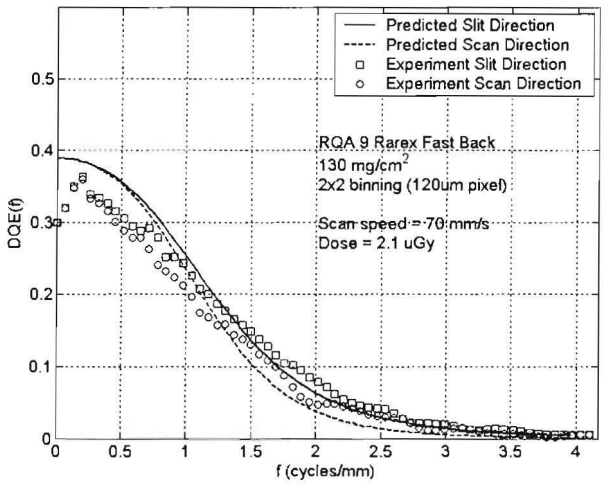

Figure 8. Measured and predicted DQE in the scan and slit direction for the Rarex Fast Back screen. The slightly inferior DQE in the scan direction at higher spatial frequencies was seen for all the five screens for which measurements were taken.

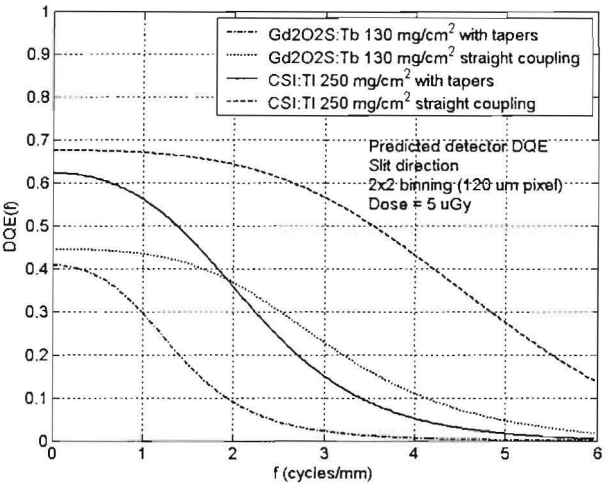

Figure 9. Predicted detector DQE at RQA9 for various detector configurations. Large gains in the detector DQE can be made by removing the coupling tapers and by replacing the unstructured screen with a structured CSI:Tl scintillator.

than that of the next thinner screen. This can be explained by examining the MTF curves in Figure 10 which suggest that the DRZ-100 mg/cm^2 has a particularly good MTF for its mass thickness.

4.2. Possible detector upgrades: Predicted DQE

The FOT coupling introduces an undesirable high frequency drop[7] in the detector DQE (see Figure 7). An improvement in the detector DQE could be made by removing the FOT coupling and replacing it with a non-demagnifying fiber optic plate (FOP) that projects the screen output onto a butted linear array of CCD's. The DQE could be further improved by replacing the screen with a structured CSI:Tl scintillator: allowing greater quantum absorption efficiency for similar or superior resolution[23]. Figure 9 shows the detector DQE calculated for various combinations of screen and coupling type. For the CSI:Tl scintillator, the following parameters values were calculated[13, 23]: $g_4 = 0.8$; $g_5 = 1550$; $e_5 = 273$; $H = 0.49$; $g_8 = 0.014$ (FOT coupling), $g_8 = 0.1$ (FOP coupling) ; $a = 0.06$ mm; $b = 2$. These results suggest that a significant increase in the detector DQE is possible, but this matter should be investigated further.

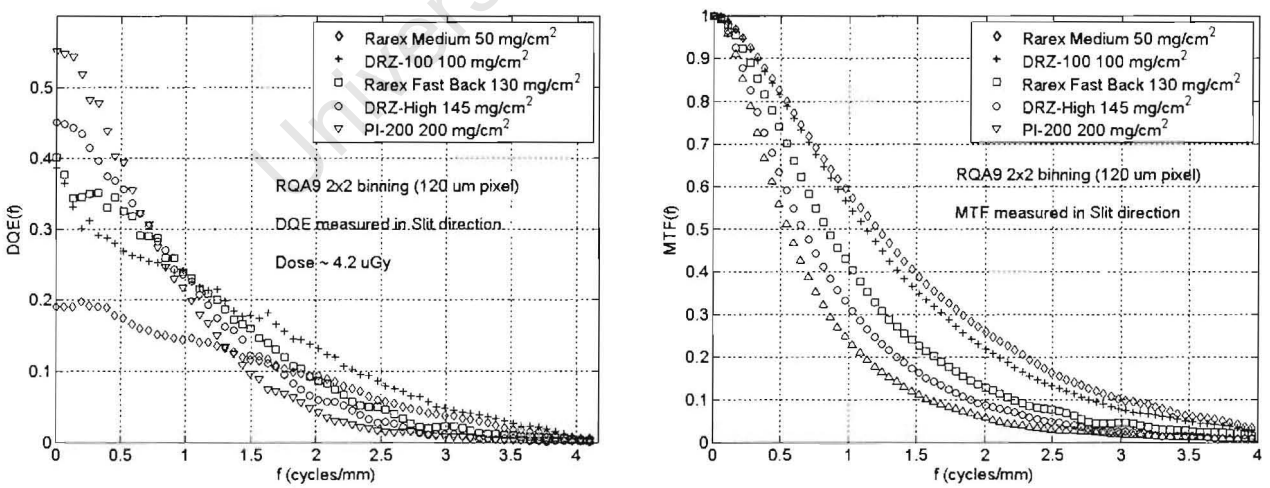

Figure 10. Measured detector DQE and MTF the five screen types used in this study. Results presented in the slit direction only.

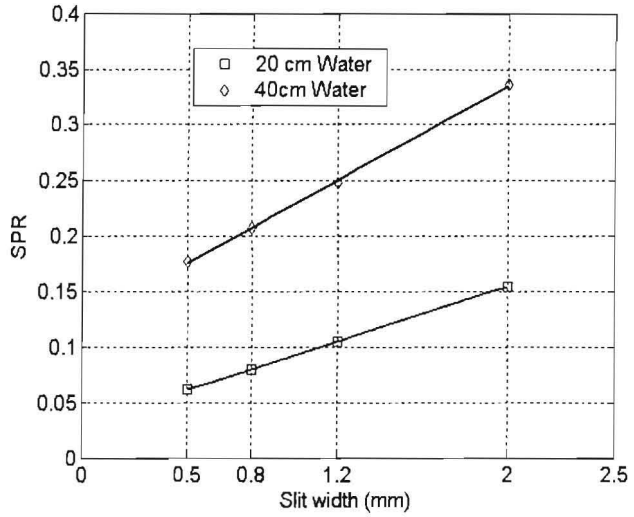

Figure 11. Monte Carlo simulated scatter to primary ratios for various slit widths and a straight line fit. The collimator slit widths of 0.5, 0.8, 1.2 and 2 mm correspond to beam widths at the detector of 3, 4, 4.9 and 7.85 mm respectively.

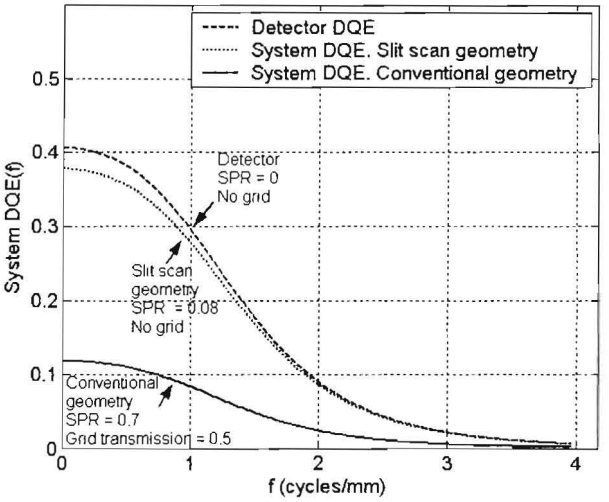

Figure 12. System and detector DQE calculated for RQA9, Rarex 130 mg/cm^2, 120um pixel detector and two different grid and scatter combinations. The Slit scan geometry performs significantly better than a conventional geometry system with an identical detector.

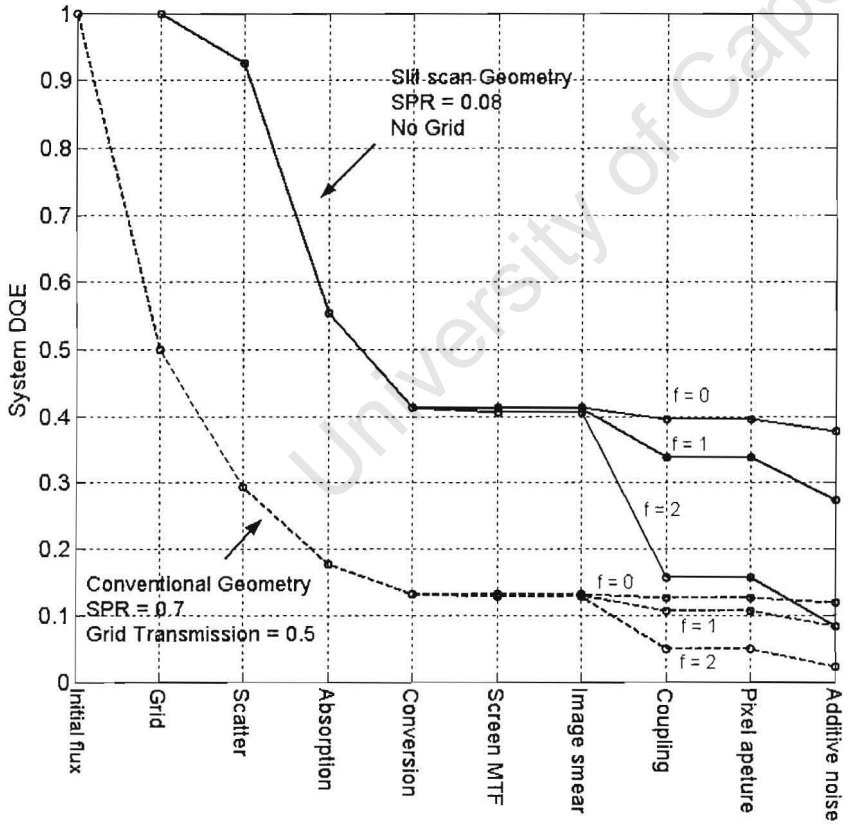

Figure 13. Stage dependent SDQE (f) calculated for two systems with different geometry but identical detectors (RQA9, Rarex 130 mg/cm^2, 120 um pixel and Dose = 5uGy). In this example the slit scanning geometry has no grid and a scatter to primary ratio (SPR) of 0.08 whereas the conventional geometry system has a grid with a 50 % transmission efficiency and a scatter to primary ratio of 0.7. The first two stages – grid attenuation and scatter - degrade the SDQE to such an extent in the conventional geometry system that even an ideal detector with a DQE of unity would still result in a "System DQE" lower than the slit scanning system. Clearly the slit scanning system has a higher "system DQE".

4.3. System DQE: Comparison of slit scan geometry with conventional geometry.

Calculation of the System DQE requires knowledge of the SPR and grid attenuation for the particular system under study. Figure 11 shows SPR results for STATSCAN as calculated by Monte Carlo simulation. For the phantoms, air gap and beam widths used in this study the SPR has an almost linear relationship to beam width. The values are in good agreement with the results of comparable simulations in the literature[1, 19, 29]. A typical value for the SPR was taken as 0.08 for the slit scanning system and was taken as 0.7 for a conventional geometry system with a grid[1, 29] (in practice this value is highly variable and dependant on the imaging task). A typical primary beam attenuation value for a grid[30] in a conventional geometry system was taken as 0.5.

Figure 12 shows the system DQE calculated for the slit scanning system and a conventional geometry system with identical detector (the detector DQE is shown on the same curve). Figure 13 shows the System DQE for the same two system plotted at each stage in the system. The results show that the efficiency of the conventional geometry system is significantly degraded by the system level effects of scatter and grid attenuation.

5. CONCLUSIONS

The cascaded linear systems model predicts system image quality metrics to a high degree of accuracy. This is encouraging in that it suggests that the model can be used to provide system insight and that system design can be improved by the optimization of model parameters.

A significantly higher SDQE can be attained by a slit scanning system than by a conventional geometry systems suggesting that slit scanning is the more efficient paradigm for x-ray imaging. At the present time the System DQE is sometimes seen as an "intuitive system parameter"[10] although it has a direct relationship to detectability by an ideal observer[10, 13]. This suggests that x-ray imaging machine manufactures should quote SDQE as well as the detector DQE when giving an evaluation of their system. Or as a minimum, the expected range of the SPR and grid attenuation as well as the detector DQE should be quoted.

ACKNOWLEDGMENTS

This work was partially funded by the MRC/UCT Medical Imaging Research Unit at the University of Cape Town and Lodox Systems (Pty) Ltd. The author would like to thank Dr. Ulrich Neitzel for assistance with the DQE measurements and concepts.

REFERENCES

1. G. T. Barnes, X. Wu, P. C. Sanders, "Scanning Slit Chest Radiography: A Practical and Efficient Scatter Control Design", *Radiology* **190,** 525-528, 1994.
2. L. J. M. Kroft, J. Geleijns, B. J. A. Mertens, "Digital Slit-Scan Charge-coupled Device Radiography versus AMBER and Bucky Screen-Film Radiography for Detection of Simulated Nodules and Interstitial Disease in a Chest Phantom", *Radiology* **231,** 156-163, 2004.
3. E. Samei, R. S. Saunders, J. Y. Lo, J. T. Dobbins, J. L. Jesneck, C. E. Floyd, C. E. Ravin, "Fundamental imaging characteristics of a slit-scan digital chest radiographic system", *Medical Physics* **31**:2687-2698, 2004.
4. S. Beningfield, H. Potgieter, A. Nicol, S. van As, G. Bowie, E. Hering, E. Latti, "Report on a new type of trauma full-body digital X-ray machine", *Emergency Radiology* **10**, 23-29, 2003.
5. H. Potgieter, M. de Villiers, M. Scheelke, "An explanation for the extremely low, but variable, radiation dosages measured in a linear slit scanning radiography system", *Proc. of SPIE,* Medical Imaging 2005.
6. M. de Villiers and G. de Jager, "Detective Quantum Efficiency of the LODOX System", *Proc. of SPIE,* Vol. 5030, Medical Imaging, 2003.
7. A. Cunningham, M. S. Westmore, A. Fenster, "A spatial-frequency dependent quantum accounting diagram and detective quantum efficiency model of signal and noise propogation in cascaded imaging systems", *Medical Physics* **21:** 1994.
8. "Medical electrical equipment – Characteristics of digital X-ray imaging devices – Part 1: Determination of the detective quantum efficiency", IEC 62220-1, International Electrotechnical Commission.
9. S. Thunberg et al., "Evaluation of a Photon Counting Mammography System." *Proc. of SPIE* Vol. 4682, Medical Imaging 2002.

10. I. S. Kyprianou, S. Rudin, D. R. Bednarek, K. R. Hoffman, "Study of the Generalized MTF and DQE for a New Microangiographic System", *Proc. of SPIE* Vol. 5368, Medical Imaging 2004.
11. E. Samei, "Image quality in two phosphor-based flat panel digital radiographic detectors." *Medical Physics* **30**: 1747-1757, 2003.
12. J. H. Siewerdsen, L. E. Antonuk, Y. El-Mohri, J. Yorkston, W. Huang, I. A. Cunningham. "Signal, noise power spectrum, and detective quantum efficiency of indirect-detection flat-panel imagers for diagnostic radiology", *Medical Physics* **25**:614-628, 1998.
13. J. H. Siewerdsen, D. A. Jaffray, "Optimization of x-ray imaging geometry (with specific application to flat-panel cone-beam computed tomography", *Medical Physics* **27**: 1903-1914, 2000.
14. U. Neitzel, S Gunther-Kohfahl, G. Borasi, E. Samei, "Determination of the detective quantum efficiency of a digital x-ray detector: Comaprison of three evaluations using a common image data set", *Medical Physics* **31** (8), 2205-2211, 2004.
15. K. Stierstorfer, M. Spahn, "Self-normalising method to measure the detective quantum efficiency of a wide range of x-ray detectors." *Medical Physics* **26**, 1312-1319, 1999.
16. E. Samei, M. J. Flynn, D. A. Reimann, "A method for measuring the presampled MTF of digital radiographic systems using and edge test device." *Medical Physics* **25** (1), 102-113, 1998.
17. J. T. Dobbins III "Effects of undersampling on the proper interpretation of modulation transfer function, noise power spectra, and the noise equivalent quanta of digital imaging systems", *Medical Physics* **22** (2): 171-180, 1995.
18. J. F. Carrier, L. Atchambault, L. Beaulieu, R. Roy, "Validation of GEANT4, an object-oriented Monte Carlo toolkit, for simulations in medical physics." *Medical Physics* **31**: 484-492, 2004.
19. J. M. Boone, J. A. Seibert, "Monte Carlo simulation of the scattered radiation distribution in diagnostic radiology." *Medical Physics* **15** :713-720, 1988.
20. J. M. Boone, J. Anthony Seibert, "An accurate method for computer-generating tungsten anode x-ray spectra from 30 to 140 kV." *Medical Physics* **24,** 1997.
21. M.J. Berger, J.H. Hubbell, S.M. Seltzer, J. S. Coursey, and D. S. Zucker, "XCOM: Photon Cross Sections Database." *Institute of Standards and Technology*, Physics Laboratory, Ionizing Radiation Division, http://physics.nist.gov/PhysRefData/Xcom/Text/XCOM.html.
22. A. Ginzburg, C. E. Dick, "Image Information transfer properties of x-ray intensifying screens in the energy range from 17 to 320 keV", *Medical Physics* **20**:1013-1021, 1993.
23. W. Zhao, G. Ristic, J. A. Rowlands, "X-ray imaging performance of structured cesium iodide scintilators", *Medical Physics* **31** (9), 2594-2605, 2004.
24. J. G. MainPrize, M. J. Yaffe, "The Effect of Phosphor Persistence on Image Quality in Digital X-Ray Scanning Systems", *Proc. of SPIE Vol.* 2708, Medical Imaging, 1996.
25. S. Hejazi, D. P. Trauernicht, "System considerations in CCD-based x-ray imaging for digital chest radiography and digital mammography." *Medical Physics* **24**:287-297, 1996.
26. J. G. Mainprize, N. L. Ford, S Yin, T. Tumer, M. J. Yaffe, "A slit-scanned photodiode-array/CCD hybrid detector for digital mammography." *Medical Physics* **29** (2), 214-224, 2002.
27. A. D. A Maidment. M. Y. Yaffe, D. B. Plewes, G. E. Mawdsley, I. C. Soutar, B. G. Starkoski, "Imaging performance of a prototype scanned-slit digital mammography system." *Proc. of SPIE* Vol. 1896, Medical Imaging 1993.
28. D. W. Holdsworth, R. K. Gerson, A. Fenster, "A time-delay integration charge-coupled device camera for slit-scanned digital radiography." *Medical Physics* **17**:876-886, 1990.
29. H-P. Chan, K. Doi, "Physical characteristics of scattered radiation in diagnostic radiology: Monte Carlo simulation studies." *Medical Physics* **12:**152-165, 1985.
30. M . Sandborg, D. R. Dance, J. Persliden, G. A. Carlsson "A Monte Carlo program for the calculation of contrast, noise and absorbed dose in diagnostic radiology." *Computer Methods and Programs in Biomedicine* Vol. **42**:167-180, 1994.